

DISSERTATION

STUDY OF COLLECTIVE BEAM EFFECTS IN ENERGY RECOVERY LINAC DRIVEN FREE  
ELECTRON LASERS

Submitted by

Christopher C. Hall

Department of Electrical and Computer Engineering

In partial fulfillment of the requirements

For the Degree of Doctor of Philosophy

Colorado State University

Fort Collins, Colorado

Spring 2016

Doctoral Committee:

Advisor: Sandra Biedron  
Co-Advisor: Stephen Milton

Carmen Menoni  
William Fairbank

Copyright by Christopher C. Hall 2016

All Rights Reserved

## ABSTRACT

### STUDY OF COLLECTIVE BEAM EFFECTS IN ENERGY RECOVERY LINAC DRIVEN FREE ELECTRON LASERS

Collective beam effects such as coherent synchrotron radiation (CSR) and longitudinal space charge (LSC) can degrade the quality of high-energy electron beams used for applications such as free-electron lasers (FELs). The advent of energy recovery linac (ERL)-based FELs brings exciting possibilities for very high-average current FELs that can operate with greater efficiency. However, due to the structure of ERLs, they may be even more susceptible to CSR. It is therefore necessary that these collective beam effects be well understood if future ERL-based designs are to be successful.

The Jefferson Laboratory ERL driven IR FEL provides an ideal test-bed for looking at how CSR impacts the electron beam. Due to its novel design we can easily test how CSR's impact on the beam varies as a function of compression within the machine. In this work we will look at measurements of both average energy loss and energy spectrum fragmentation as a function of bunch compression. These results are compared to particle tracking simulations including a 1D CSR model and, in general, good agreement is seen between simulation and measurement. Of particular interest is fragmentation of the energy spectrum that is observed due to CSR and LSC. We will also show how this fragmentation develops and how it can be mitigated through use of the sextupoles in the JLab FEL. Finally, a more complete 2D model is used to simulate CSR-beam interaction. Due to the parameters of the experiment it is expected that a 2D CSR model would yield different results than the 1D CSR model. However, excellent agreement is seen between the two CSR model results.

## ACKNOWLEDGEMENTS

I would like to thank my advisors Sandra Biedron and Stephen Milton. Without their input and guidance this work would certainly not have been possible. I also owe a great deal to a number of people at JLab who worked on the FEL and allowed me to have the opportunity to work on such an interesting problem. In particular David Douglas, Chris Tennant, Rui Li, and Stephen Benson all provided so much help and support for this work. To my parents and grandparents who have cheered me on through all of this, and last but not least, my wife Mandy, for her love and support.

This dissertation is typeset in  $\text{\LaTeX}$  using a document class designed by Leif Anderson.

## TABLE OF CONTENTS

Abstract .....	ii
Acknowledgements .....	iii
List of Tables .....	vi
List of Figures .....	vii
Chapter 1. Introduction .....	1
Chapter 2. Collective Beam Effects .....	5
2.1. Coherent Synchrotron Radiation .....	5
2.2. Transverse Space Charge .....	18
2.3. Longitudinal Space Charge .....	19
Chapter 3. Experimental Setup .....	22
3.1. The Jefferson Laboratory Energy Recovery Linac Driven Free Electron Laser ..	22
3.2. Basic Principle of FEL Operation .....	23
3.3. Accelerator Components .....	26
3.4. Description of the Experiment .....	35
Chapter 4. Analysis with a 1-D CSR Model .....	48
4.1. Modeling Collective Effects .....	48
4.2. Controlling Numerical Noise .....	49
4.3. Measurement Calibration .....	52
4.4. Determining Initial Beam Conditions .....	54
4.5. Simulation Results .....	56

Chapter 5. 2D CSR Simulations .....	90
5.1. The Derbenev Criterion .....	91
5.2. BC1 Chicane Model in CSRtrack .....	95
5.3. Simulation Results and Analysis .....	97
Chapter 6. Conclusion .....	107
References .....	110
Appendix A. Transport Notation .....	116
Appendix B. Accelerator Coordinate Conventions .....	118

## LIST OF TABLES

2.1	Bunch properties and beamline parameters at entrance of the fourth dipole for the JLab bunch compression chicane. Values were obtained from simulations of the beamline. (Note that the geometric emittance is given here.) . . . . .	17
3.1	Nominal beam parameters for the experiment and relevant characteristics of the machine. . . . .	36
4.1	Parameters used to calculate bunch profile and LSC fields for linear compression, nonlinear compression, and compression with $T_{566}$ corrected to linearize the bunch. . . . .	88

## LIST OF FIGURES

2.1	A particle on some arbitrary trajectory with instantaneous velocity $\beta(t')$ at time $t'$ . The fields from the particle are observed at a point $P$ at some later time $t'$ . The unit vector $\mathbf{n}(t')$ points from the particle to $P$ and the vector between the particle and $P$ is $\mathbf{r}(t')$ . . . . .	7
2.2	A qualitative illustration of incoherent and coherent radiation produced from a group of electrons. Above, for short-wavelength radiation, all electrons emit at vastly different, random phases leading to incoherence. Below, for long-wavelength radiation, the relative phase differences are small and the radiation is coherent. . .	8
2.3	The CSR field from Eq. 2.4 for a 135 pC Gaussian bunch with rms length of 167 fs traveling through a uniform magnetic field on a radius of curvature of 1.2 m. This matches the conditions within the dipoles of the BC1 chicane of the JLab FEL. The Gaussian distribution is overlaid. The head of the bunch is located at $s > 0$ .	11
2.4	Within a magnetic field radiation produced by a particle at the tail of the bunch by a particle $s'$ at a position $P'$ within the magnet may catch up to the head of the bunch $s$ at some later time at the position $P$ . This is due to the bunch being constrained traveling on the arc of length $l = R\phi_m$ between $P'$ and $P$ while the radiation travels on the chord $\vec{n}$ between the two points. . . . .	13
2.5	The CSR field from Eq. 2.4 for a 135 pC Gaussian bunch with rms length of 167 fs traveling through a uniform magnetic field on a radius of curvature of 1.2 m. This matches the conditions within the dipoles of the BC1 chicane of the JLab FEL. The CSR wake is shown at various distances into the magnet. As the bunch travels into the maget the transient term of the field slips ahead of the bunch while	

	the steady state term grows stronger. A Gaussian distribution is overlaid. The tail of the bunch is at $s < 0$ and the head is at $s > 0$ . . . . .	14
2.6	Shown in (a) for a particle on a reference dispersive trajectory $x_\eta$ within a dipole at the point of emission $\Delta x_{\beta,emis} = \Delta x_{\eta,emis}$ . The result is a new dispersive trajectory given by $x_{\eta,emis}(s) = x_\eta + \Delta x_{\eta,emis}$ . The resulting effect on the emittance is shown in (b) where different longitudinal slices now have varying betatron functions, increasing the projected emittance. . . . .	15
2.7	Radiation emitted by a particle at $s'$ in the tail of the bunch at a position P' in the dipole will catch up to a particle at $s$ at the head of the bunch at a later point P. The blue line shows the path assumed by the projected model while the red shows the true path that must be followed by the radiation for two particles with large horizontal separation. . . . .	18
2.8	Impedances for LSC (red) and CSR (blue) as a function of $\lambda^{-1}$ with the spectrum of a Gaussian bunch with rms length 150 fs overlaid (green). . . . .	21
3.1	Layout of the FEL at Jefferson Laboratory. The IR FEL system, shown in black, was used for these measurements. The grey is the UV line and was not used in this experiment. . . . .	23
3.2	Electrons follow an oscillatory path (green) through the dipole fields of the undulator. As bunching occurs on the scale of $\lambda_L$ the power in the optical pulse grows exponentially due to the coherent emission of the electrons (shown above in blue). . . . .	25

3.3	A bunch accelerated on the rf-wave at phase $\phi_0 < 0$ , or on the rising-side. The head is at negative $z$ coordinates with respect to the middle of the bunch while the tail is at positive $z$ coordinates with respect to the middle. ....	28
3.4	Schematic of a bunch compression system starting with a bunch passed off-crest through the linac before passing through a four-dipole chicane with legs of length $L$ . ....	29
3.5	Schematic of the Bates bend design used in the recirculation arc. Dipoles are represented as trapezoids and in the case of the 180 degree bend by half a donut shape, quadrupoles as ovals, and sextupoles as diamonds. Trajectories for kicked particles are illustrated by the black and red lines, showing the path dependence through the 180 deg bend. ....	32
3.6	Layout of the first arc (A1) section of the JLab FEL. Dipoles are represented by gray trapezoids, quadrupoles are blue ovals, and sextupoles are shown as green diamonds. Two beam position monitors are represented by vertical red lines. ....	37
3.7	Plots of beam centroid position as function of integrated quadrupole field (in units of Gauss) in A1, where (a) and (b) are the BPM readings in the middle of A1 for falling-rf and rising-rf acceleration respectively and (c) and (d) are the BPM readings in the middle of A2 for falling-rf and rising-rf acceleration respectively. .	39
3.8	Plots of beam centroid position with the baseline reading subtracted from the energy loss data. The data for falling-rf acceleration is shown in (a) and the rising-rf acceleration data is shown in (b). ....	40

3.9	Example plot showing the beamline elements along the bottom in black, with the compression of the bunch (defined as $\text{Compression} = (1 + hR_{56})^{-1}$ ) in red, and the sign of the chirp, $h$ , plotted in blue. ....	41
3.10	For falling rf acceleration the compression ratio (red) and the normalized sign of the chirp (blue) are plotted along the beamline. Shown in (A) - (C) are the undercompressed, fully compressed, and overcompressed cases for BC1 compression. The same are represented in (D) -(F) for compression in the first arc. Parasitic compressions can be observed when the sign of the chirp (blue) changes, then changes back in a single dipole. ....	43
3.11	For rising rf acceleration the compression ratio (red) and the normalized sign of the chirp (blue) are plotted along the beamline. Shown in (A) - (C) are the undercompressed, fully compressed, and overcompressed cases for BC1 compression. Parasitic compressions can be observed when the sign of the chirp (blue) changes, then changes back in a single dipole. ....	45
3.12	Examples of the beam distribution from the synchrotron light monitor operated in A2. Plots to the left and below the center image show the projection of the y and x distributions respectively. The x-distribution corresponds directly to the energy spectrum of the beam. Shown in (A) is an example of the spectrum for an uncompressed bunch. Shown in (B) is the spectrum of a bunch that has compressed at the end of BC1.....	47
4.1	Scan over the number of particles in the simulation. Shown in (A) is $\langle \delta \rangle$ as a function of the number of particles and in (B) $\delta\epsilon_x$ , the fractional deviation of the emittance as a function of the number of particles. ....	50

4.2	Scan over the number of bins used in each dipole to calculate the shape of the CSR wake. Shown in (A) is $\langle\delta\rangle$ as a function of the number of bins and in (B) $\delta\epsilon_x$ , the fractional deviation of the emittance as a function of the number of bins. ....	51
4.3	Scan over the step size interval at which the CSR wake calculation is performed in CSRDrift elements. Shown in (A) is $\langle\delta\rangle$ as a function of the step size and in (B) $\delta\epsilon_x$ , the fractional deviation of the emittance as a function of the step size. ....	52
4.4	Dispersion calculated at the arc BPMs as a function of the MQT2F08 quadrupole strength.....	54
4.5	Comparison of energy loss for acceleration on the falling-rf side for various initial bunch lengths at the linac entrance.....	55
4.6	Fractional energy deviation of the beam as a function of the first arc momentum compaction $R_{56}^{A1}$ for acceleration on the rising side of the rf. The experimental data is shown with the diamond symbols. The simulation is shown with sextupoles off in black and the sextupoles on in red. ....	57
4.7	Fractional energy deviation of the beam as a function of the first arc momentum compaction $R_{56}^{A1}$ for acceleration on the falling side of the rf. The experimental data is shown with the diamond symbols. The simulation is shown with sextupoles off in black and the sextupoles on in red. ....	59
4.8	Fractional energy deviation as a function of position along the beamline. In (A) the result for full compression at the end of the first arc is shown. In (B) full compression is achieved at the end of the first chicane.....	60
4.9	Comparison of a bunch with sextupoles off (black) and on (red). The longitudinal phase space immediately before the BC1 chicane is shown.....	63

4.10	Comparison of a bunch with sextupoles off (black) and on (red). The longitudinal phase space immediately after BC1 is shown in (A), and (B) is the current distribution(histogram of (A)) at the end of BC1.....	64
4.11	Energy loss as a function of position along the beamline at maximum compression after BC1 for sextupoles turned off (black) and on (red).....	65
4.12	The longitudinal phase space at the entrance (black) and exit (red) of the BC2 chicane. Shown in (A) is the phase space with the sextupoles turned off and in (B) with the sextupoles configured to provide linearization.....	66
4.13	Measurements of the energy spectrum collected in the second Bates arc (A2). The vertical axis is the population (arb. units) and the horizontal axis is the energy (arb. units). As the compression is changed a distinct spike and depletion region form and shift along the spectrum, shown from (a) to (f) for the BC1 compression point and from (g) to (l) for the A1 compression point. ....	68
4.14	(A) The longitudinal phase space of a compressed bunch after BC1 is shown overlaid with the density distribution. (B) The density distribution is shown together with the CSR wake at the end of the fourth dipole in BC1. In both plots the head of the bunch occurs at $t < 0$ . ....	69
4.15	Simulation of the energy spectrum as the beam progresses in (a)-(f) from under-compressed to critically compressed to over-compressed. In each plot the energy spectrum is examined at the end of BC1 (black), the entrance to BC2 (red), and the middle of A2 (blue).....	70

4.16	The longitudinal phase space overlayed with the energy spectrum at the beginning of BC2 (a)-(c) and the beginning of BC1 (d)-(f). The horizontal line is the predicted point from Eq. 50. ....	72
4.17	Energy spectrum before BC2 for maximum compression between BC1 and BC2. The spectrum with sextupoles off is shown in black. In red is the spectrum for full compression and sextupoles on. In blue the sextupoles are on but the bunch is slightly over-compressed. The vertical axis has been normalized. ....	74
4.18	(A) Mountain range plot of the energy spectrum difference from the baseline taken when the sextupoles are correctly set. The sextupole strength is scaled from 0 to 300% of the correct setpoint for linearizing the bunch. At the bottom left the sextupoles are completely off while at the top right of the plot the sextupole strength has reach 300% of the correct setpoint. (B) Baseline momentum distribution when sextupoles are set to nominal strength. ....	75
4.19	The standard deviation (A) and the maximum deviation (B) of the energy spectrum minus the baseline as the sextupoles are scaled from 0 to 300% of the correct sextupole setpoint for linearizing a bunch at full compression after BC1. For both calculations the edges of the distribution are excluded. ....	76
4.20	The space charge oscillation period as a function modulation wavelength (shown for typical beam parameters downstream of BC1). ....	78
4.21	The longitudinal density distribution at the end of BC2 for various macroparticle counts in Elegant with LSC enabled. ....	79

4.22	Simulated energy loss as a function of $R_{56}$ setting in A1. The simulation without LSC is shown in black and with LSC is shown in red. In both cases CSR is enabled.....	80
4.23	Energy spectrum at the center of A2 for simulations with LSC turned off (red) and on (black). CSR is enabled in both cases.....	81
4.24	Comparison of total energy loss due CSR (red), LSC (blue), and both LSC and CSR (white) accumulated between BC1 and BC2 at full compression after BC1...	82
4.25	The energy spectrum of the bunch is shown at three positions: the exit to BC1 (black), the entrance to BC2 (red), and the middle of A1 (blue). Compression at the end of BC1 is varied from under-compressed through to over-compressed in (A)-(F).....	84
4.26	The energy spectrum of the bunch is shown at three positions: the exit to A1 (black), the entrance to BC1 (red), and the middle of A1 (blue). Compression at the end of BC1 is varied from under-compressed through to over-compressed in (A)-(F).....	86
4.27	The longitudinal charge distribution at the entrance to A2 for a bunch compressed at the end of A1. ....	87
4.28	(A) Longitudinal density for linear transport (red) and nonlinear transport (blue) and (B) the corresponding LSC fields calculated from Eqs. 55 and 59. ....	88
4.29	(A) Longitudinal density for adjusted setting of $T_{566}$ to linearize transport (B) the corresponding LSC fields calculated from Eqs. 55 and 59. ....	89
5.1	For radiation emitted from the tail of a bunch at some time $t$ .....	92

5.2	The Derbenev parameter, defined in Eq. 64, is plotted as a function of position within the BC1 chicane. Three cases are shown, under-compressed in red, critically-compressed in blue, and over-compressed in green. ....	94
5.3	Comparison between CSRtrack and Elegant in blue and green respectively with CSR calculations turned off in both simulations. Shown from the top left going clockwise are the horizontal phase space (in the bending plane), the vertical phase space, and the longitudinal phase space. For the horizontal and vertical planes the ellipse calculated from the Twiss parameters of each bunch is shown. ....	96
5.4	The energy loss due to CSR in the BC1 chicane is plotted as a function of $R_{56}^{A1}$ , the momentum compaction, in the first arc. The black line shows the result for Elegant, the red and blue symbols show the 1D and 2D results from CSRtrack....	98
5.5	The bunch length at the end of the BC1 chicane is plotted as a function of $R_{56}^{A1}$ , the momentum compaction, in the first arc. The black line shows the result for Elegant, the red and blue symbols show the 1D and 2D results from CSRtrack. Note that red and blue symbols are directly over top of each other. ....	99
5.6	Shown in (a) is the energy loss as a function of position in the BC1 chicane for $R_{56}^{A1} = 0.695$ m with the 1D and 2D CSRtrack results shown in red and blue respectively and the 1D result from Elegant in black. The rate of energy loss $\frac{d\langle p \rangle}{\langle p_i \rangle ds}$ is shown in (b). The vertical black lines represent the boundaries of the four dipoles. ....	100
5.7	Shown in (a) is the energy loss as a function of position in the BC1 chicane for $R_{56}^{A1} = 0.655$ m with the 1D and 2D CSRtrack results shown in red and blue respectively and the 1D result from Elegant in black. The rate of energy loss	

	$\frac{d\langle p \rangle}{\langle p_i \rangle ds}$ is shown in (b). The vertical black lines represent the boundaries of the four dipoles.....	101
5.8	Shown in (a) is the energy loss as a function of position in the BC1 chicane for $R_{56}^{A1} = 0.612$ m with the 1D and 2D CSRtrack results shown in red and blue respectively and the 1D result from Elegant in black. The rate of energy loss $\frac{d\langle p \rangle}{\langle p_i \rangle ds}$ is shown in (b). The vertical black lines represent the boundaries of the four dipoles.....	103
5.9	Plots $x'-t$ for (a)the critically-compressed bunch and (b) the over-compressed bunch. The heat map is based upon energy change between two successive steps in the simulation starting 0.25 m from the entrance to the fourth dipole. (Note that in this plot $t > 0$ is the head of the bunch.) .....	105
5.10	The energy spectrum is plotted for the under-compressed, critically-compressed, and over-compressed cases in (a), (b), and (c). The 1D CSRtrack result is shown in red, the 2D CSRtrack in blue, and 1D Elegant in black. ....	106
B.1	The ideal reference trajectory through the accelerator along a path $s$ with radius of curvature $\rho_0(s)$ is shown. Particles in the bunch can then be defined in terms of their deviation from the reference particle, given as the vector $\delta\boldsymbol{\rho}(s)$ .....	118

## CHAPTER 1

# INTRODUCTION

Particle accelerators have made possible invaluable advances in a wide variety of fields, both in the basic and applied sciences [1]. Electron-based particle accelerator light sources, both synchrotrons and free electron lasers (FELs), are capable of providing high-brightness light, including ultraviolet and x-ray radiation. These light sources are used for research by a broad community of scientists in different fields, [2] and demand is such that there are now dozens of light source facilities around the world. The design of the next generation of free electron lasers looks to focus on increase of bunch repetition rate (higher average power) and providing more undulator lines for users to meet this growing demand [3]. An energy recovery linac (ERL) [4] based FEL can provide for both of these requirements due to its very efficient operation at high average power and a design that can accommodate multiple undulator lines [5]. There are also plans to use ERLs for a proposed electron-ion collider [6] that would require extremely high power electron beams. While demand for the capabilities of ERLs is increasing these proposed accelerators do not come without significant challenges that will need to be addressed.

One of these is the issue of collective beam effects, that may degrade beam quality during transport, and decrease performance of free-electron laser (FEL) sources, in particular. In this work we will primarily examine the impact of coherent synchrotron radiation (CSR) on the properties of the electron bunch. Because CSR strongly effects short bunches, like those used for FELs, and scales quadratically with the number of particles in the bunch,  $P_{CSR} \propto N^2$ , it is vital that CSR is accounted for and properly managed in the design of any FEL. A very high peak beam current is desirable for increasing FEL efficiency, this

translates into producing very short bunches. This is normally done through compression of the bunch in a dipole-based chicane structure. This very short bunch length also can greatly increase coherent emission of the bunch within the dipoles, and this effect, unless understood and controlled, will degrade the energy spread and projected emittance of the bunch. This may be a particular issue for ERLs. This is due to the need for many more dipoles to provide recirculation back to the linac entrance. It is critical, then, that we have a good understanding of how to model CSR effects in simulation and how to mitigate the impact of CSR in the accelerator if we wish to use ERLs as a base for future FELs and light sources in general.

Improvement in simulation of CSR is essential for use these design studies of future machines, to provide understanding of CSR's impact on beam quality. However, beyond this, new simulation tools are also vital to expanding our understanding of the underlying physics. This is well demonstrated in the work of Ryne et al. [7], who have used their massively parallel Lienard-Wiechert solver code to show CSR-induced microbunching is quite sensitive to vertical beam size. This is a surprising result, given the normal assumption that the beam will be more sensitive to size in the horizontal bending plane. Such results show the need for further study of CSR in simulation beyond the typical, 1D projected CSR model.

For the proposed Medium Energy Electron-Ion Collider (MEIC) at Jefferson Laboratory a high-energy (55 MeV) ERL-based electron cooling ring is required to cool the ion beam [8]. Simulation studies [9] have shown that CSR-induced microbunching may cause excessive rise in the electron bunch energy spread if left unchecked. Considerable effort has now been put into the study of how CSR-induced microbunching may be expected to grow in the recirculation structures of ERLs [10]. Such studies face additional challenges, such as that of transient CSR effects, which must be accounted for, as they may remain quite important

in the microbunching growth process [11]. The importance of CSR transient effects will also be seen in the work presented here, where CSR remains significant in the drifts downstream of the bending dipoles. Providing improved measurements of these transient effects will be important to ensuring the success of future ERL projects such as MEIC.

The Jefferson Laboratory (JLab) ERL driven FEL [12] has beamlines that provide very high average power lasing in both the IR and UV. As an operational ERL based FEL the impact of CSR has already played into the design of this accelerator [13] in many aspects, and this makes the accelerator an excellent testbed for studying how CSR will impact future ERLs such as in MEIC. The JLab FEL is ideal for the continued study of CSR due to several novel aspects of its design, and a collaboration has been built up focused on studying the collective effects. This study encompasses all steps of the research process from theory and simulation through to experimental studies.

For this work we used the JLab FEL to perform an experiment focused on the study of how the total CSR emission within the accelerator varies as a function of the compression point and how, in turn, CSR impacts key parameters of the beam. Experimental observations are made and compared to several different models used to simulate the conditions of the experiment. From these results we also draw several important conclusions about how to best manage the impact of collective forces on the beam and improve the ERL and FEL performance.

The general theory of CSR and the 1D model most frequently used to calculate the CSR field are described in Chapter 2, along with the theory of transverse and longitudinal space charge forces. In Chapter 3 the critical components of the JLab FEL are summarized and the key longitudinal dynamics of the machine and the compression system are detailed. We then describe the exact setup of the experiment that was performed on the JLab FEL. The

results of the experiment are shown in Chapter 4. Those results are discussed and compared against theory and simulation, a number of key conclusions are drawn about how to mitigate the negative impacts of CSR and longitudinal space charge. Finally, in Chapter 5 we include the results from 2D CSR simulations. These simulations use a more complete model of CSR and show general agreement, but also several distinct anomalies, not predicted by the more common 1D CSR model. As discussed previously such findings highlight how essential it is to continue to push the bounds of research into CSR in both simulation and experiment.

## CHAPTER 2

# COLLECTIVE BEAM EFFECTS

While space-charge forces on the beam can often be ignored for an ultra-relativistic electron beam (with  $\gamma \gg 1$ ), some collective effects still remain extremely important for electron beams in free-electron lasers, even at very high energies. This should come as no surprise as the FEL itself arises from the collective action of the electrons in a bunch. By creating a bunch that will be suitable for lasing we are necessarily setting it up to be susceptible to collective effects throughout the whole accelerator. Indeed, these problems, such as CSR and microbunching are desirable within the confines of the undulator. In this regard we are somewhat victims of our own success, we have succeeded admirably in creating an electron bunch that will lase within the FEL, but must keep it from manifesting such behavior during the initial transport lest the bunch's desirable properties be corrupted.

In this section we will discuss the physical origin of coherent synchrotron radiation and examine its impact upon the electron beam to show why it can degrade FEL performance. We will then look at space charge forces, in particular longitudinal space charge, which will be seen to be a major driver of energy spectrum fragmentation.

### 2.1. COHERENT SYNCHROTRON RADIATION

The term synchrotron radiation is generally used to refer to radiation emitted by charged particles that have been deflected by a magnetic field. The very first idea of synchrotron radiation arose from the independent work of Alfred Lienard in 1898 [14] and then Emil Wiechert [15] in 1900 from their application of the idea of retarded potentials. The first experimental confirmation of synchrotron radiation came from John Blewett who predicted and measured the orbit reduction due to the energy loss in the G.E. Research Lab 100 MeV

betatron [16]. Actual observation of synchrotron radiation finally came in 1947 from the G.E. 70 MeV synchrotron which had clear vacuum chamber sections allowing for synchrotron radiation in the visible spectrum to be observed. Not long after this Julian Schwinger published his thorough work on the properties of synchrotron radiation and made special note of the possible coherence of lower harmonics [17].

To describe the theory of synchrotron radiation we begin with the Lienard-Wiechert potentials

$$(1) \quad \phi(t) = \frac{e}{4\pi\epsilon_0} \frac{1}{(1 - \hat{\mathbf{n}}(t') \cdot \boldsymbol{\beta}(t')) r(t')}$$

$$(2) \quad \mathbf{A}(t) = \frac{\mu_0 e}{4\pi} \frac{\mathbf{v}(t')}{(1 - \hat{\mathbf{n}}(t') \cdot \boldsymbol{\beta}(t')) r(t')}$$

which describe the scalar and vector potential ( $\phi$  and  $\mathbf{A}$  respectively) experienced by an observer located at a point  $P$  at time  $t$  due to a moving charge with an instantaneous velocity  $\boldsymbol{\beta}(t')$  (illustrated in Fig. 2.1). At time  $t'$  the particle and observer are separated by a distance  $r(t')$  along the unit vector  $\hat{\mathbf{n}}(t')$ . Because of the propagation of the potential at the speed of light  $c$  there is a relationship between the observation time  $t$  and the earlier time  $t'$  at which the potential was emitted from the charge,  $t' = t - r(t')/c$ . Because the signal propagates at  $c$  there is a causal restriction that  $r(t') < c|t - t'|$  for the potential to be observed at  $P$ , else there will not be sufficient time for it to have reached the observation point.

From the retarded potentials (Eqs. 1 and 2) we can calculate the fields from the usual expressions  $\mathbf{E} = -\nabla\phi - \frac{\partial\mathbf{A}}{\partial t}$  and  $\mathbf{B} = \nabla \times \mathbf{A}$ , giving the following result for the electric and magnetic fields  $\mathbf{E}(t)$  and  $\mathbf{B}(t)$

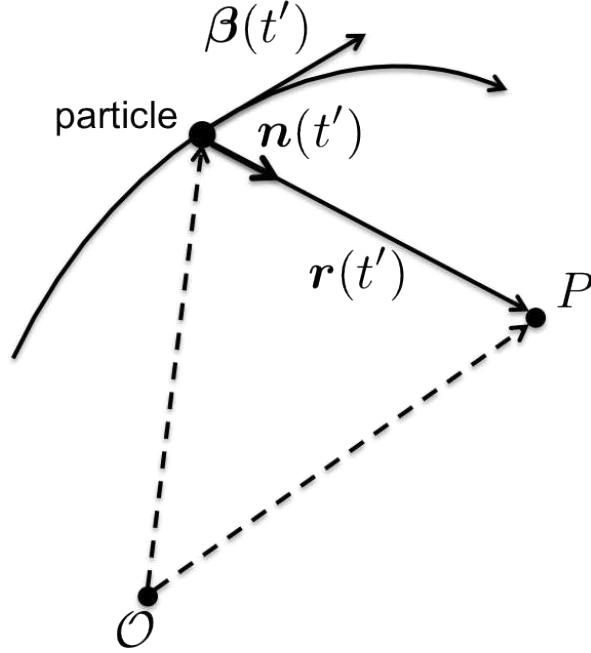


FIGURE 2.1. A particle on some arbitrary trajectory with instantaneous velocity  $\beta(t')$  at time  $t'$ . The fields from the particle are observed at a point  $P$  at some later time  $t'$ . The unit vector  $\mathbf{n}(t')$  points from the particle to  $P$  and the vector between the particle and  $P$  is  $\mathbf{r}(t')$ .

$$(3) \quad \mathbf{E}(t) = \frac{e}{4\pi\epsilon_0} \left\{ \frac{(\mathbf{n} - \boldsymbol{\beta})}{\gamma^2 (1 - \mathbf{n} \cdot \boldsymbol{\beta})^3 r^2} + \frac{\mathbf{n} \times ((\mathbf{n} - \boldsymbol{\beta}) \times \dot{\boldsymbol{\beta}})}{c (1 - \mathbf{n} \cdot \boldsymbol{\beta})^3 r} \right\}_{\text{retarded}},$$

$$(4) \quad \mathbf{B}(t) = \frac{\mathbf{n}_{\text{retarded}} \times \mathbf{E}}{c}.$$

The first term in Eq. 3 is referred to as the Coulomb field and has a  $\gamma^{-2}$  dependence. This will also be seen in calculations of the space charge field later. The second term will only be nonzero when the charge is accelerating, due to the presence of  $\dot{\boldsymbol{\beta}}$ . It is this term that gives rise to synchrotron radiation.

2.1.1. TEMPORAL COHERENCE. In the previous section, synchrotron radiation was considered mostly from the standpoint of a single particle. However, in an accelerator, or most physical systems, there will be numerous electrons all radiating simultaneously over a broad

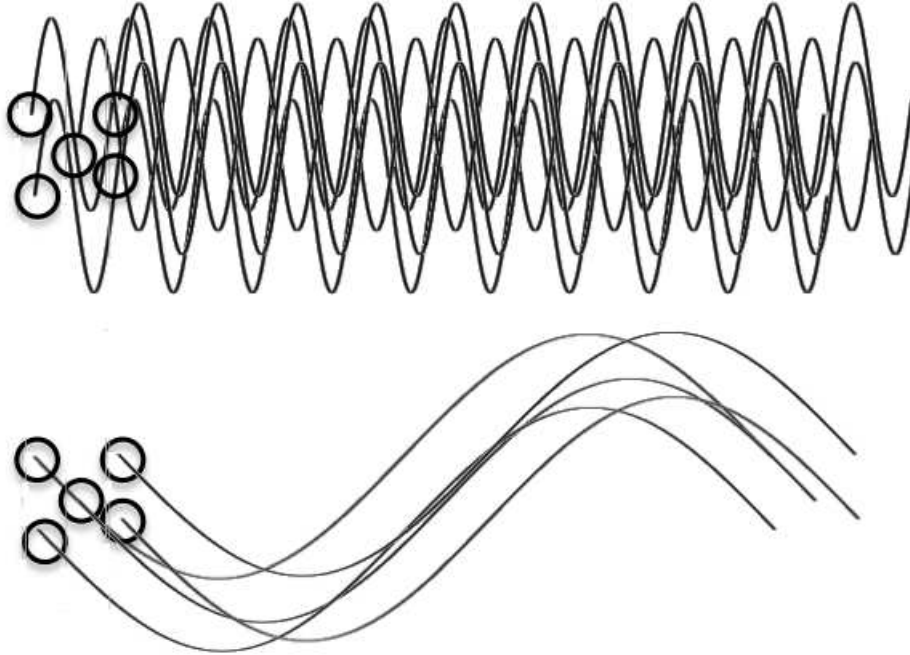


FIGURE 2.2. A qualitative illustration of incoherent and coherent radiation produced from a group of electrons. Above, for short-wavelength radiation, all electrons emit at vastly different, random phases leading to incoherence. Below, for long-wavelength radiation, the relative phase differences are small and the radiation is coherent.

spectrum of wavelengths. Because the electrons are randomly distributed in space the phase differences at a chosen wavelength between all the electrons will be random. The observed power will scale linearly with the number of electrons. However, since synchrotron radiation is a broad-spectrum effect it is possible to have wavelengths produced that are much longer than the bunch length. In this case, the contribution from all the electrons may effectively be in phase, leading to temporal coherence of the radiation. These two cases are illustrated qualitatively in Fig. 2.2

This process can be described in a more quantitative fashion [18] beginning with the emission for the  $i$ th electron in a bunch

$$(5) \quad E_i \propto e^{i(\omega t + \phi_i)}$$

with frequency  $\omega$  and a phase given by  $\phi_i = 2\pi z_i/\lambda$  described in terms of the relative distance from the center of the bunch  $z_i$ . The radiation power is then given by summing over the square of the contributions for all electrons of the bunch

$$(6) \quad P \propto \sum_{i=0}^N \sum_{j=0}^N e^{-i(\omega t + \phi_i)} e^{i(\omega t + \phi_j)} = N + \sum_{i \neq j}^N e^{i(\phi_i - \phi_j)}$$

the first term is the incoherent power which scales linearly with particle number. The second term will average to zero if the phases  $\phi_{i,j}$  are random and uncorrelated unless the radiation wavelength is large. For a specified, symmetric longitudinal density function  $\lambda(z)$  the radiated power can then be written as

$$(7) \quad P(k) = p(k) \left( N + N(N-1) \left| \int_{-\infty}^{\infty} \lambda(z) e^{-ikz} \right|^2 \right),$$

where the integral is the so-called form factor that represents the dependence on the electron distribution. As will be seen this dependence on the electron distribution will play a large role in how CSR impacts the bunch. Since there are normally on the order of  $10^8$  electrons in a bunch the quadratic term for coherent radiation will be quite significant.

2.1.2. MODELING 1D CSR. While it is certainly possible to use Eq. 3 to directly compute the fields for a collection of charges this effort is highly inefficient. The calculation will scale quadratically with the number of particles, and there is also a significant strain placed

on memory resources as it is important to store particle and field history at retarded times for the calculation. In the most widely used approximation for calculating CSR fields in a simulation without resorting to this direct, cumbersome calculation the electron distribution is projected onto a line tangent to its curved trajectory within the dipole field. Reducing the number of dimensions will reduce the complexity but introduces a singular term to the field due to the Coulomb field on the line. By subtracting out this term a simple closed form approximation can be derived for the CSR-induced energy loss along the length of the bunch. It is also assumed that the beam has  $\gamma \gg 1$  and that the Coulomb field is smaller than the radiation field. The energy loss per particle per unit distance as a function of position within the bunch  $s$  for particles orbiting on a circle is then found to be

$$(8) \quad \left( \frac{d\mathcal{E}(s)}{cdt} \right)_{\text{coh,steady}} = -\frac{2e^2}{3^{\frac{1}{3}}R^{\frac{2}{3}}} \int_{-\infty}^s \frac{ds'}{(s-s')^{\frac{1}{3}}} \frac{d\lambda(s')}{ds'},$$

where  $R$  is the bending radius of the dipole field. The dependence of the energy loss on the derivative of the longitudinal charge distribution  $d\lambda(s)/ds$  indicates that while particles along the tail of the bunch lose energy, the overtaking of particles at the head of the bunch by radiation generated from the tail of the bunch will cause some particles at the head to gain energy instead. However, the overall change in average energy for the bunch will be negative. The shape of the field for a bunch with a Gaussian distribution, as predicted by Eq. 8, is shown in Fig. 2.3.

In an actual accelerator the particles travel not on full circular trajectories but on arc segments inside dipole fields. To account for this, a transient term [19] must be introduced to the description of CSR-induced energy loss. This is because there is an overtaking length

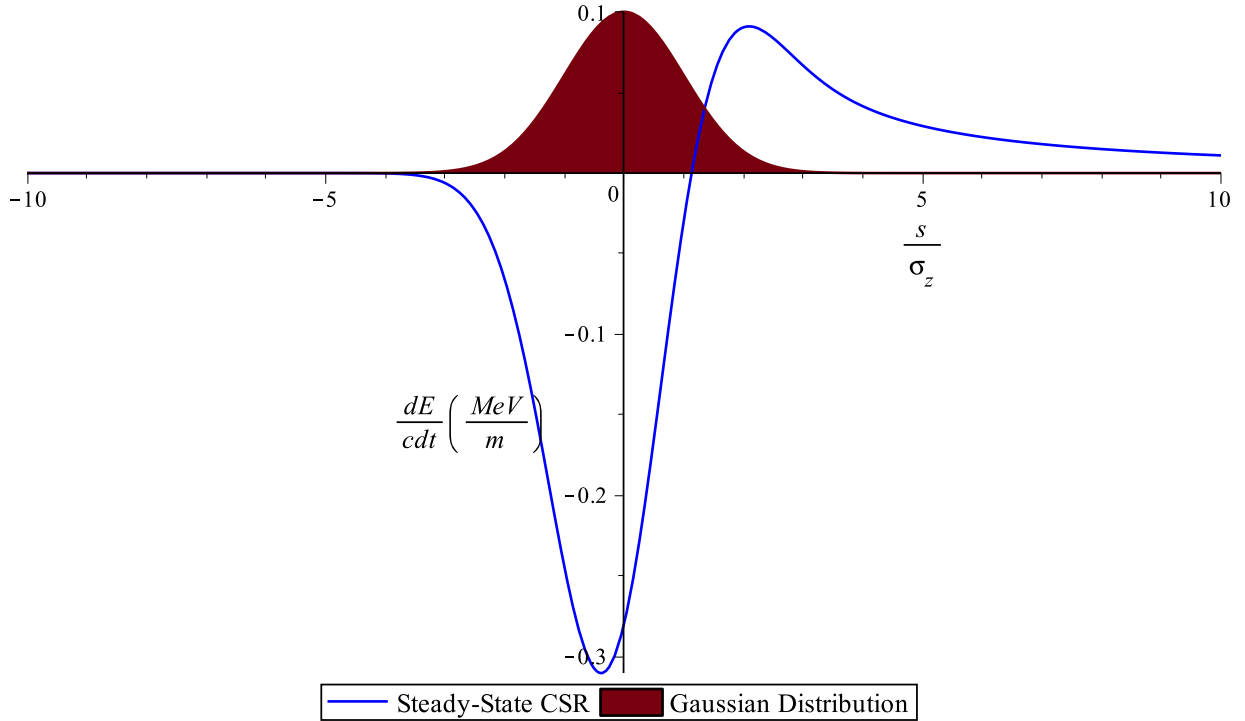


FIGURE 2.3. The CSR field from Eq. 2.4 for a 135 pC Gaussian bunch with rms length of 167 fs traveling through a uniform magnetic field on a radius of curvature of 1.2 m. This matches the conditions within the dipoles of the BC1 chicane of the JLab FEL. The Gaussian distribution is overlaid. The head of the bunch is located at  $s > 0$ .

$$(9) \quad L_{\text{overtaking}} = (24\sigma_z R^2)^{\frac{1}{3}}.$$

At the beginning of the dipole, radiation from the tail of the bunch will not yet have been able to catch up to the head. As the bunch travels farther into the dipole, radiation from farther back in the bunch will be able to overtake the whole bunch. At a distance  $L_{\text{overtaking}}$ , radiation from the tail will fully overtake the head. The CSR field, including this transient effect, is given by

$$(10) \quad \left( \frac{d\mathcal{E}(s, \phi)}{d(ct)} \right)_{Coh, total} = -\frac{2e^2}{3^{\frac{1}{3}}R^{\frac{2}{3}}} \left\{ \left( \frac{R\phi^3}{24} \right)^{-\frac{1}{3}} \left[ \lambda \left( s - \frac{R\phi^3}{24} \right) - \lambda \left( s - \frac{R\phi^3}{6} \right) \right] + \int_{s-\frac{R\phi^3}{24}}^s \frac{ds'}{(s-s')^{\frac{1}{3}}} \frac{d\lambda(s')}{ds'} \right\},$$

where the first term in square brackets accounts for the transient field that will grow at the beginning of the magnet before slipping by the bunch. As this transient term declines farther into the magnet the steady-state field given by the integral will come to dominate. In both terms the slippage length

$$(11) \quad L_{slippage}(\phi) = \frac{R\phi^3}{24}.$$

features very prominently. The slippage length accounts for the path length difference between the path of the particles and the radiation (Fig. 2.4). As the angular distance into the magnet  $\phi$  grows and if the length of the magnet  $R\phi_m \gg L_{slippage}$ , then the transient term in Eq. 10 will die out and the energy loss will be restored to Eq. 8.

An example of the CSR field (sometimes called the CSR wake), including the transient effects in Eq. 10, is shown in Fig. 2.5. As the bunch travels farther into the magnet the transient portion of the field moves ahead of the bunch while the steady-state field grows, eventually recovering the same form as in Eq. 8.

2.1.2.1. *Impact of CSR on Beam Quality.* The first impact of CSR on the beam is to raise the energy spread of the bunch. Because the longitudinal field applied from CSR will not be uniform along the length of the bunch (see Fig. 2.3) the energy spread of different

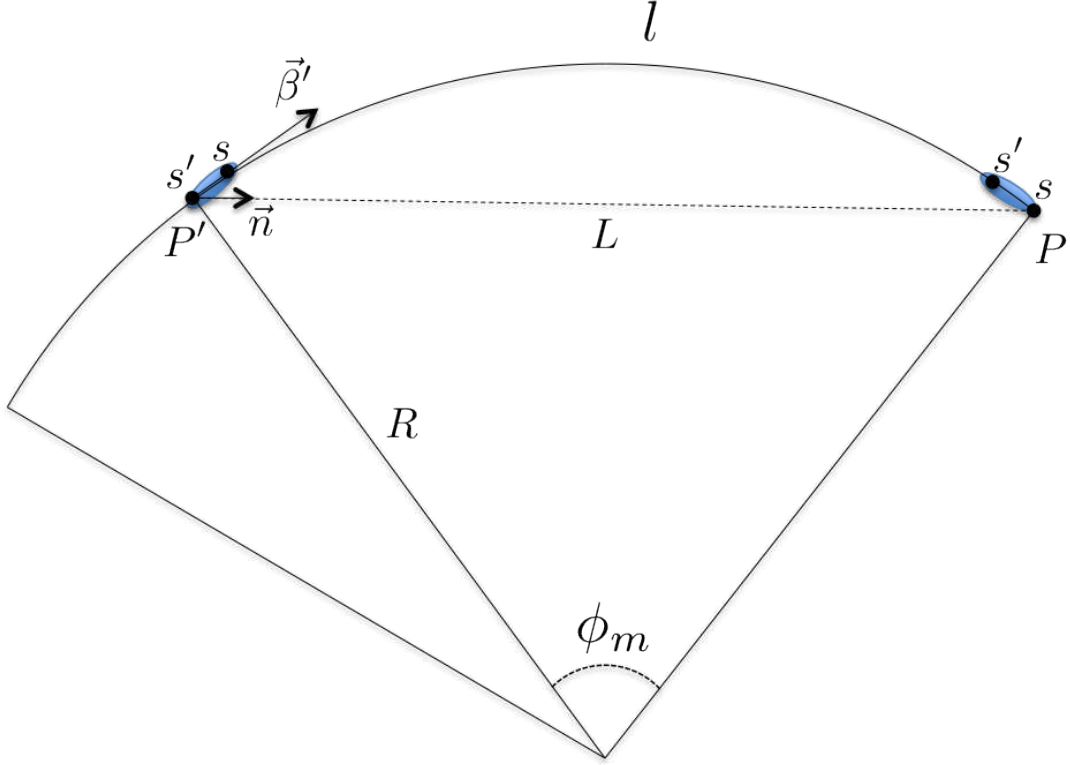


FIGURE 2.4. Within a magnetic field radiation produced by a particle at the tail of the bunch by a particle  $s'$  at a position  $P'$  within the magnet may catch up to the head of the bunch  $s$  at some later time at the position  $P$ . This is due to the bunch being constrained traveling on the arc of length  $l = R\phi_m$  between  $P'$  and  $P$  while the radiation travels on the chord  $\vec{n}$  between the two points.

longitudinal slices along the bunch will now vary. The impact of CSR to the energy spread of the bunch may be calculated in the steady-state approximation [19] as

$$(12) \quad \sigma_{\delta,CSR} = 0.2459 \frac{r_e Q L}{e \gamma R^{\frac{2}{3}} \sigma_z^{\frac{4}{3}}}.$$

Where  $r_e$  is the classical electron radius,  $e$  is the elementary charge,  $Q$  is the total bunch charge,  $\gamma$  is the relativistic factor,  $\sigma_z$  is the rms bunch length, and  $L$  and  $R$  are the dipole length and radius.

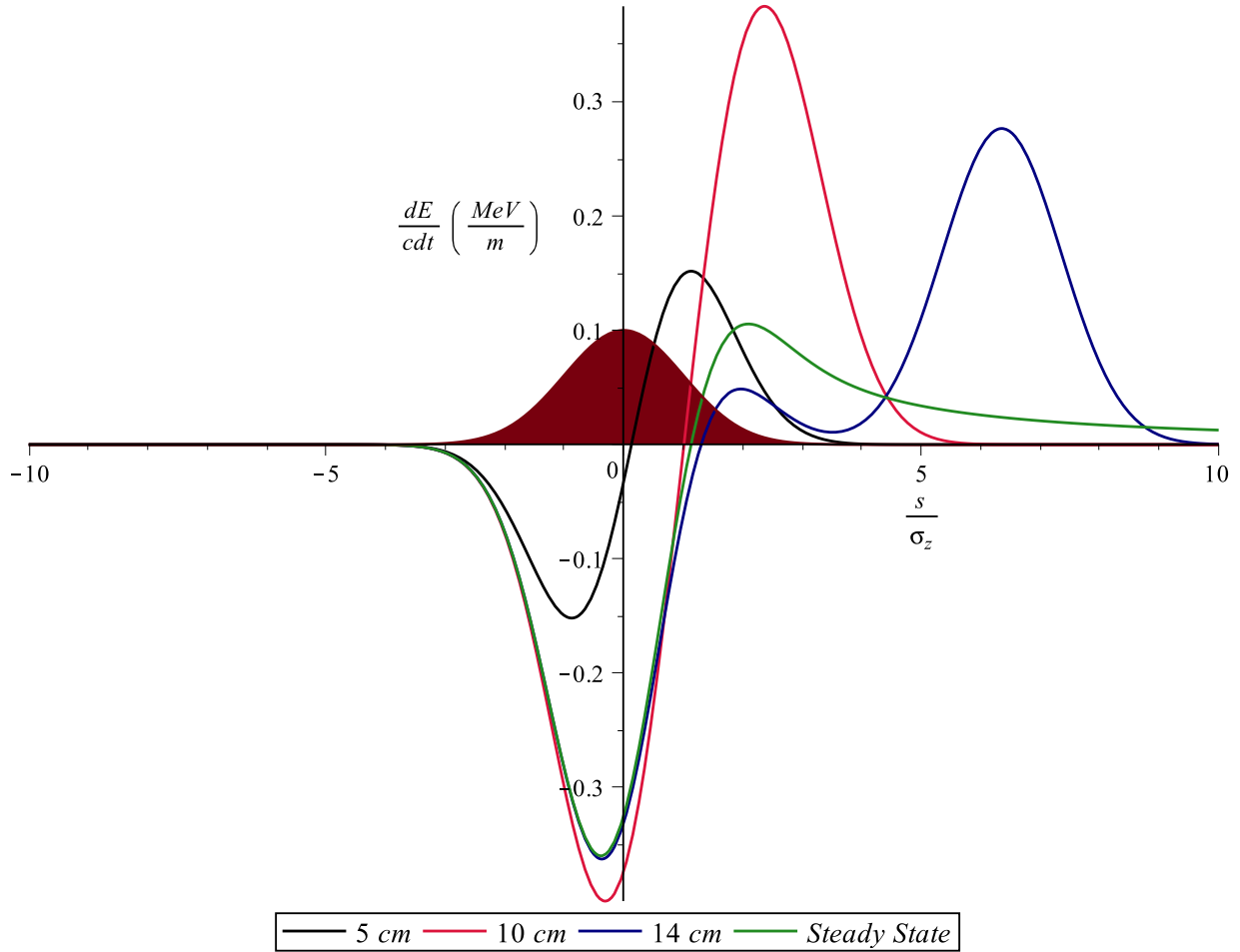


FIGURE 2.5. The CSR field from Eq. 2.4 for a 135 pC Gaussian bunch with rms length of 167 fs traveling through a uniform magnetic field on a radius of curvature of 1.2 m. This matches the conditions within the dipoles of the BC1 chicane of the JLab FEL. The CSR wake is shown at various distances into the magnet. As the bunch travels into the magnet the transient term of the field slips ahead of the bunch while the steady state term grows stronger. A Gaussian distribution is overlaid. The tail of the bunch is at  $s < 0$  and the head is at  $s > 0$ .

For particles moving in a dipole (see Fig. 2.6(a)) the horizontal position (see Appendix B for a discussion of accelerator coordinate conventions) without emission will be a superposition of the betatron and dispersive motion of the particle,  $x(s) = x_\beta(s) + x_\eta(s)$ . The dispersive motion is given in terms of the local dispersion as  $x_\eta(s) = \eta_x(s)\delta$ . At the point of emission  $\Delta x = 0$ , that is there will be no change in transverse coordinates of the particle

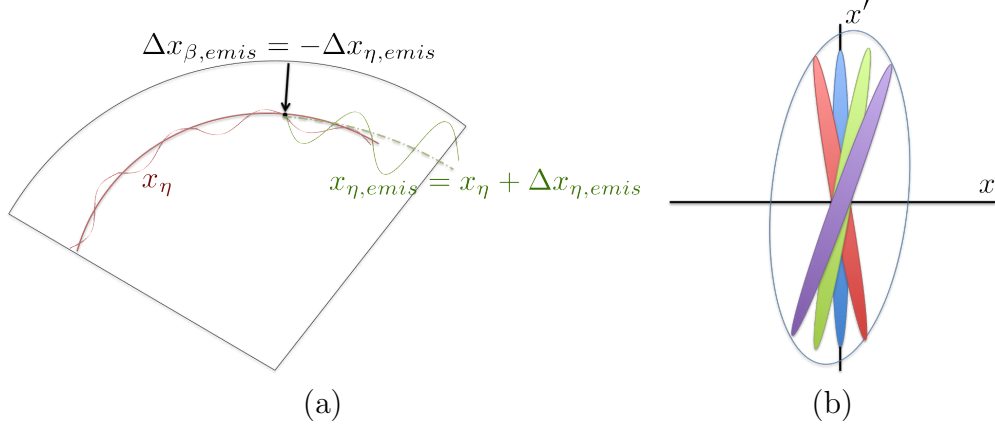


FIGURE 2.6. Shown in (a) for a particle on a reference dispersive trajectory  $x_\eta$  within a dipole at the point of emission  $\Delta x_{\beta,emis} = \Delta x_{\eta,emis}$ . The result is a new dispersive trajectory given by  $x_{\eta,emis}(s) = x_\eta + \Delta x_{\eta,emis}$ . The resulting effect on the emittance is shown in (b) where different longitudinal slices now have varying betatron functions, increasing the projected emittance.

and  $\Delta x_{\beta,emis} = \Delta x_{\eta,emis}$ . This results in the particle following a new dispersive trajectory  $x_{\eta,emis}(s) = x_\eta + \Delta x_{\eta,emis}$ . Since this new trajectory  $\Delta x_{\eta,emis} = \eta_x \Delta p_{CSR} / p$  depends on the energy lost by the particle to CSR and this energy loss varies with longitudinal position, different longitudinal slices will now follow new trajectories through the dipole. While the emittance of individual slices may be preserved the overall effect is that the different slices will no longer align in the bending plane and the projected emittance will be increased, as illustrated in Fig. 2.6(b).

The impact on the projected emittance may be quantified [20], for a single, averaged CSR kick, through the change to the beam matrix given by

$$(13) \quad \epsilon_f \approx \left( \det \begin{bmatrix} \epsilon_0 \beta_x + \eta_x^2 \sigma_{\delta,CSR}^2 & -\epsilon_0 \alpha_x + \eta_x \eta'_x \sigma_{\delta,CSR}^2 \\ -\epsilon_0 \alpha_x + \eta_x \eta'_x \sigma_{\delta,CSR}^2 & \epsilon_0 \gamma_x + \eta_x'^2 \sigma_{\delta,CSR}^2 \end{bmatrix} \right)^{\frac{1}{2}}.$$

Where  $\gamma_x = \frac{1+\alpha_x^2}{\beta_x}$ ,  $\sigma_{\delta,CSR}$  is given by Eq. 12, and  $\eta'_x$  is the dispersive dependence of  $x'$ . This result may be summarized as

$$(14) \quad \epsilon_f = \epsilon_0 \sqrt{1 + \frac{H}{\epsilon_0} \sigma_{\delta,CSR}^2}$$

Where the parameter  $H$  contains the initial horizontal motion parameters and takes the form

$$(15) \quad H \equiv \frac{\eta^2 + (\beta\eta' + \alpha\eta)^2}{\beta}$$

Assuming that the bunch becomes fully compressed only at the end of the third dipole of the chicane and that most of the contribution to the CSR induced emittance growth comes from the final dipole the energy spread increase and emittance growth may be estimated using Eqs. 12 and 14. Example values for the beam and lattice conditions, taken from simulations, are given in Table. 2.1 . The result is an energy spread increase from CSR of  $\sigma_{\delta,CSR} = 5.2 \times 10^{-4}$  and a growth to the projected emittance of  $\epsilon_f/\epsilon_0 = 1.25$ .

2.1.2.2. *Limitations of the 1D Model.* In the projected 1-D CSR model the CSR wake is calculated based on the charge distribution projected on a line tangent to the central path of the bunch. It is assumed that the bunch shape will not change significantly on the scale of the overtaking length. Two particles can then be causally linked using the slippage length, Eq. 11, based on the difference between the path on the arc followed by the electrons and a chord connecting the ends of that path. However, as illustrated in Fig. 2.7 when two particles have a large horizontal separation the true distance between them may be much

TABLE 2.1. Bunch properties and beamline parameters at entrance of the fourth dipole for the JLab bunch compression chicane. Values were obtained from simulations of the beamline. (Note that the geometric emittance is given here.)

Parameter (Units)	Value
$Q$ (pC)	135
$\gamma$	264
$\sigma_z$ (fs)	150
$\epsilon_0$ ( $\mu m$ )	0.1355
$L$ (m)	0.424
$R$ (m)	1.2
$\beta$ (m)	5
$\alpha$	0.35
$\eta$ (m)	-0.065
$\eta'$	0.35

greater than that predicted based on the 1D projection approximation. This calculation will, in general, need to account for the total transverse displacement of the particle. However, this effect is particularly significant due to the possibility of a large spread of the bunch in the bending plane of the chicane from dispersion. The vertical extent of the bunch normally remains well constrained.

The validity of the projected approximation can be estimated [21] from the condition

$$(16) \quad \sigma_x \left( \frac{1}{\sigma_z R^2} \right)^{\frac{1}{3}} \ll 1,$$

where  $\sigma_x$  and  $\sigma_z$  are the rms horizontal and longitudinal bunch sizes and  $R$  is the bending radius of the dipole. Since violation of this linear condition may lead to significantly more particles being causally connected, this effect would suggest that the impact of CSR will be over-estimated in the 1D model as compared to reality. However, the 1D model has in general shown good comparisons to experimental data, and especially in short-wavelength

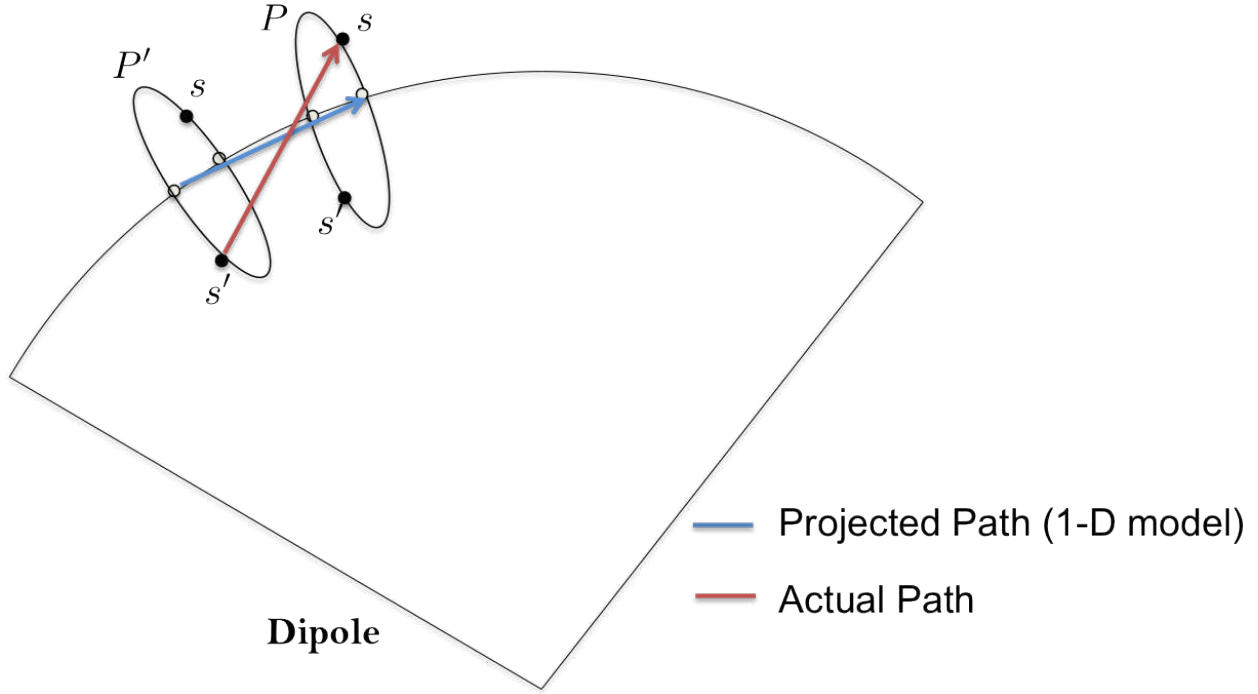


FIGURE 2.7. Radiation emitted by a particle at  $s'$  in the tail of the bunch at a position  $P'$  in the dipole will catch up to a particle at  $s$  at the head of the bunch at a later point  $P$ . The blue line shows the path assumed by the projected model while the red shows the true path that must be followed by the radiation for two particles with large horizontal separation.

FELs where both the emittance and energy spreads tend to be very small, the condition from Eq. 16 holds well. We will explore this issue in more detail in a later chapter.

## 2.2. TRANSVERSE SPACE CHARGE

For high-energy electron beams, with  $\gamma \gg 1$ , the transverse space charge forces can often be ignored. The reason for this is the cancellation of the transverse space charge forces in the beam in the ultra-relativistic approximation. To see this consider the simple model of a long cylinder of uniform charge  $\lambda$  and radius  $R$ ; the electric fields will be

$$(17) \quad E_r = \frac{\lambda}{2\pi\epsilon_0 r} \quad r > R$$

$$(18) \quad E_r = \frac{\lambda}{2\pi\epsilon_0 R^2} r \quad r \leq R$$

and the magnetic field will be given by

$$(19) \quad B_\phi = \frac{\mu_0 \lambda \beta c}{2\pi r} \quad r > R$$

$$(20) \quad B_\phi = \frac{\mu_0 \lambda \beta c}{2\pi R^2} r \quad r \leq R$$

The force on particles within the beam will then be given by the Lorentz force  $\mathbf{F} = e\mathbf{E} + e(\mathbf{v} \times \mathbf{B}) = (eE_r - e\beta c B_\phi) \hat{r}$  for a beam propagating along only the z axis at speed  $\beta$ . Substituting in the relevant expressions from Eqs. 17 and 19

$$(21) \quad F = \frac{e\lambda}{2\pi R^2} r \left( \frac{1}{\epsilon_0} - \mu_0 \beta^2 c^2 \right) = \frac{e\lambda}{2\pi\epsilon_0 \gamma^2 R^2} r \hat{r}$$

Thus the electric and magnetic fields for the beam will scale with  $1/\gamma^2$  leading to full cancellation in the limit  $\beta \rightarrow 1$ . For this reason the transverse space charge field of the beam can often be neglected in particle tracking for high energy electron beams.

### 2.3. LONGITUDINAL SPACE CHARGE

Longitudinal space charge forces will show the same  $\gamma^{-2}$  scaling as previously shown for transverse space charge [18]; however, under certain circumstances these forces may still become appreciable. For a cold, low-emittance electron beam, fluctuations in the longitudinal

charge density can lead to relatively large deviations in the local charge concentration along the beam. This density modulation leads to an appreciable buildup of the longitudinal space charge (LSC) forces along the beam. The LSC force in a modulated beam has been identified as one of the primary drivers of the microbunching instability [22]. While microbunching is not a concern in the work shown here, we will show later that LSC forces can still significantly impact the beam. This effect is most important in the coasting beam downstream of the compression section (arc or chicane). When the bunch is highly compressed the integrated effect of the force from LSC along the 10's of meters of drift space where the beam remains unperturbed longitudinally can still lead to a significant effect in the energy spectrum of the beam that is observed in experiment and simulation.

The LSC model used in `elegant` is based on a free-space 1D approximation [22] that gives the impedance as

$$(22) \quad Z_{LSC}(k) = \frac{iZ_0}{\pi k r_b^2} \left[ 1 - \frac{k r_b}{\gamma} K_1 \left( \frac{k r_b}{\gamma} \right) \right],$$

where  $Z_0 \approx 377\Omega$  is the impedance of free-space,  $r_b$  is the average beam radius,  $\gamma$  is the Lorentz factor, and  $k = 2\pi/\lambda$  is the wavenumber. A comparison between the LSC impedance per meter in Eq. 22 and the CSR impedance (based on Eq. 8) is shown, for a Gaussian charge distribution with rms width of 150 fs, in Fig 2.8. It is significant to observe that the absolute value of the CSR impedance is much greater than that of the CSR in the spectral region for a Gaussian bunch. However, the reason that LSC can still remain significant to the bunch's development is that CSR will exist only in the dipoles and then quickly die off. The LSC force will remain constant as long as the bunch remains compressed which can be

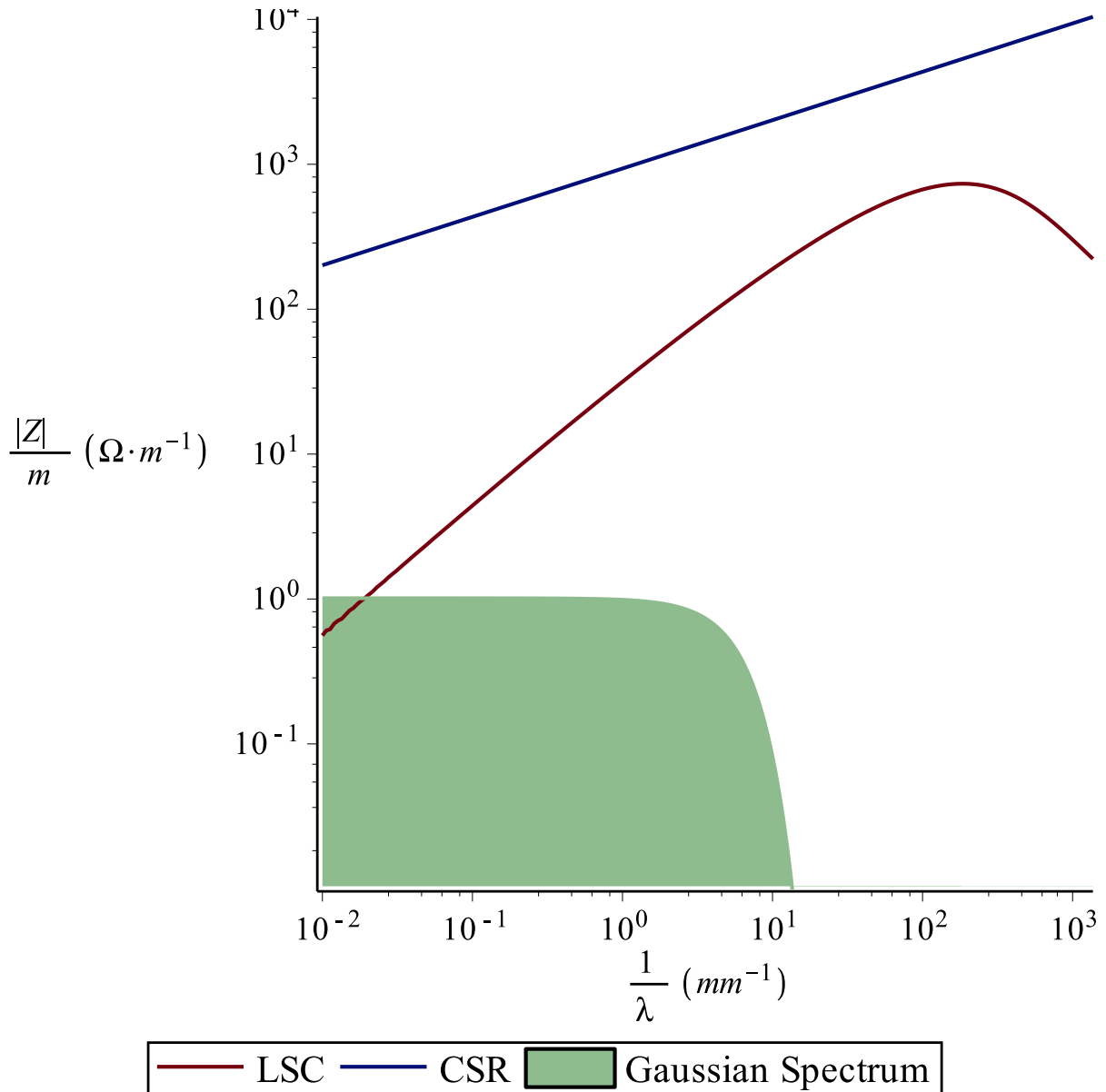


FIGURE 2.8. Impedances for LSC (red) and CSR (blue) as a function of  $\lambda^{-1}$  with the spectrum of a Gaussian bunch with rms length 150 fs overlaid (green).

over a distance of as much as 40 m. This means that the integrated impact of LSC can be much more significant than CSR, depending on the length of the beamline.

## CHAPTER 3

# EXPERIMENTAL SETUP

### 3.1. THE JEFFERSON LABORATORY ENERGY RECOVERY LINAC DRIVEN FREE ELECTRON LASER

The Jefferson Laboratory energy recovery linac (ERL) free-electron laser (FEL) (Fig. 3.1) is designed to provide high average-power light in the 1-14  $\mu m$  range from the IR undulator line [23] and 250 - 1000 nm from the UV line [24].

The electron beam is produced in a DC photocathode injector and accelerated to 9-10 MeV before being passed to the linac. The linac uses superconducting rf (SRF) cavities, housed in three cryomodules for acceleration of the beam up to 100-160 MeV. After passing through the undulator, where the FEL light is produced, the beam is then recirculated back to the linac with a 180 degree offset from the accelerating phase. This allows for the recapture of a significant fraction of the beam energy, greatly increasing machine efficiency. This energy recovery process makes operation of a very high average-power accelerator, much more palatable in terms of operational costs, but does increase the complexity of the accelerator. The payoff is quite significant though, the JLab IR FEL has produced a record operational output of 14.3 kW average power at 1.6  $\mu m$  [23].

Of particular relevance for this work are the additional complications with respect to longitudinal beam dynamics that must be dealt with. Careful management of the longitudinal phase space is required for the FEL process and for energy recovery. There will be a large increase in the fractional energy-spread both from the FEL and from the deceleration process. This can lead to great difficulty in controlling the beam and can lead to undesirable loss of the beam if not dealt with. To prevent this it is necessary to properly shape the higher-order

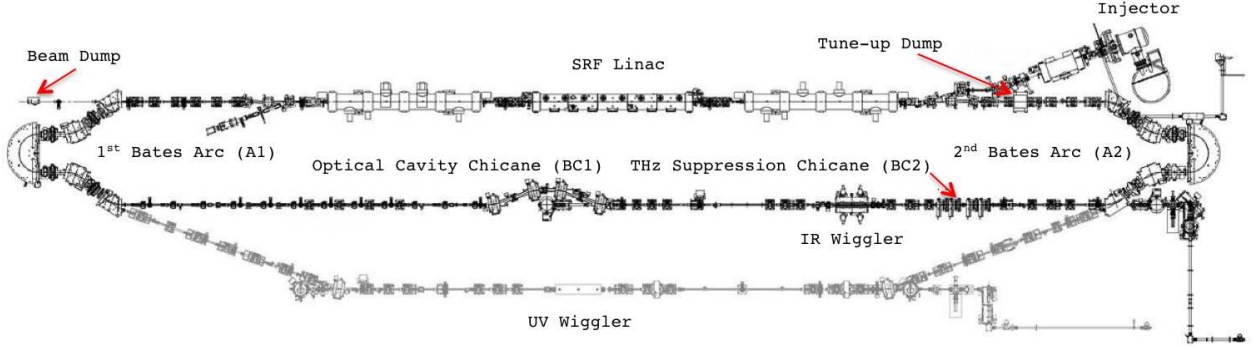


FIGURE 3.1. Layout of the FEL at Jefferson Laboratory. The IR FEL system, shown in black, was used for these measurements. The grey is the UV line and was not used in this experiment.

moments of the beam through use of sextupoles and magnets in the second recirculation arc [25]. This same mechanism of momentum compaction<sup>1</sup> control also allows for a very easily controllable knob over CSR emission in various regions of the machine. As will be shown, manipulation of the first-order momentum compaction can be used to control the region of the beamline where the bunch length is at a minimum (and produces the greatest levels of CSR). This allows for a novel experiment examining CSR under a much wider array of beam dynamics conditions than in previous experiments on other facilities [26–28].

### 3.2. BASIC PRINCIPLE OF FEL OPERATION

In passing through the fields of an undulator magnet electrons will perform an oscillatory motion due to alternating dipole fields of the undulator. This will cause the bunch to radiate around a wavelength  $\lambda_L$  determined by

$$(23) \quad \lambda_L = \frac{\lambda_u}{2\gamma^2} \left( 1 + \frac{K^2}{2} \right),$$

<sup>1</sup>In this work we will refer to  $R_{56}$  as the momentum compaction of a transfer line as opposed to the commonly used definition for circular accelerators of  $\alpha = \frac{dL/L}{dp/p}$  for momentum compaction, a global property of such accelerators.

where  $\lambda_u$  is the undulator period,  $\gamma$  is the Lorentz factor given by  $\gamma = E/m_e c^2$ , and  $K$  is defined as

$$(24) \quad K = \frac{eB_u \lambda_u}{2\pi m_e c},$$

in terms of the charge of the electron  $e$ , the undulator magnetic field  $B_u$ , and the undulator period  $\lambda_u$ .

The JLab FEL uses an FEL oscillator configuration. For an FEL oscillator there is a short undulator set along an optical cavity. On either end of the cavity are two mirrors, one of which will ideally provide total reflection, while the other will be partially transmitting to out-couple the FEL light. When electron bunches first pass through the cavity they will radiate incoherently. However, if the pulses of radiation are synchronized with the passage of subsequent bunches the radiation power will grow and the electron bunch will begin to microbunch on the scale of  $\lambda_L$ . This will lead to coherent emission scaling quadratically with particle number  $N^2$ . This process is illustrated in in Fig. 3.2. The growth in the power of the light is then a function of the number of passes,  $n$ , and the power out-coupled from the FEL is given by

$$(25) \quad P_{out} = P_0 (1 + g_{ss} - \alpha)^n,$$

where  $P_0$  is the input power in the cavity,  $\alpha$  is losses do to absorption and transmission of the mirrors, and  $g_{ss}$  is the small-signal gain factor which may be estimated [29] from

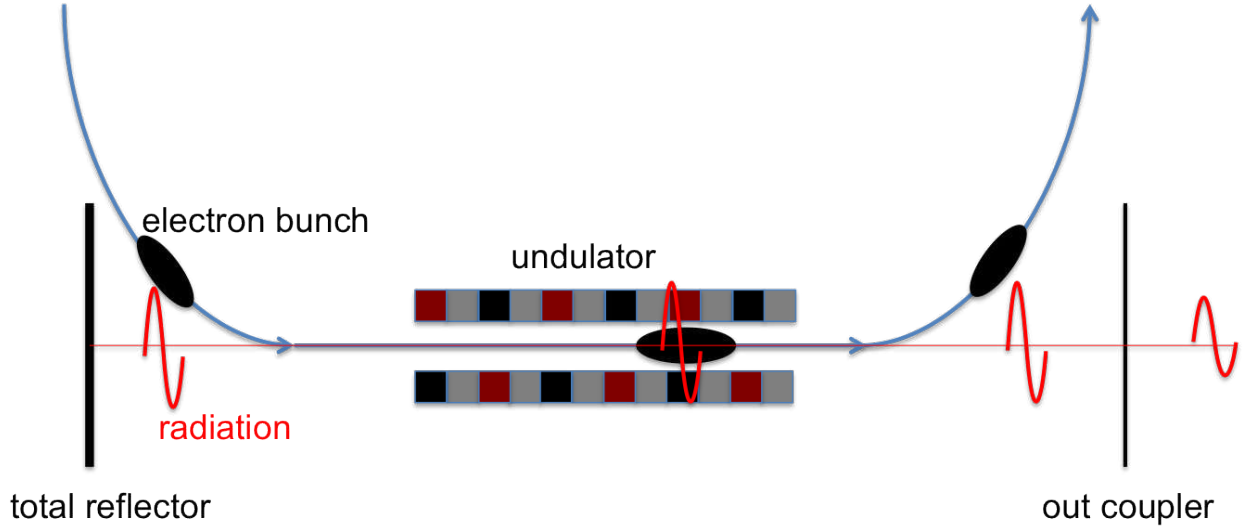


FIGURE 3.2. Electrons follow an oscillatory path (green) through the dipole fields of the undulator. As bunching occurs on the scale of  $\lambda_L$  the power in the optical pulse grows exponentially due to the coherent emission of the electrons (shown above in blue).

$$(26) \quad g_{ss} = 2 \frac{N_u^3 \hat{K}_u^2 \lambda_u^2 I_{peak}}{\gamma^3 \sigma_r^2 I_A}.$$

Where  $N_u$  is the number of periods in the undulator,  $I_{peak}$  is the peak current of the electron bunch,  $\sigma_r$  is the transverse dimension of the bunch, and  $I_A$  is the Alfvén current, defined as  $I_A = m_e c^3 / e$ . The parameter  $\hat{K}_u$  is defined to be

$$(27) \quad \hat{K}_u = K \left( J_0 \left( \frac{K^2}{4 + 2K^2} \right) - J_1 \left( \frac{K^2}{4 + 2K^2} \right) \right).$$

Where  $J_0$  and  $J_1$  are Bessel functions of the first kind. If the small-signal gain factor is larger than the losses,  $g_{ss} > \alpha$ , the power in the optical cavity will grow with each pass, up until the cavity saturates. If we wish to maximize power gain through the undulator the small-signal gain should be maximized. This makes it desirable to keep  $\sigma_r$  small and

consequently the transverse emittances  $\epsilon_{x,y}$  should also be small. Likewise,  $I_{peak}$  should be large. We emphasize these two conditions because the need for a high peak current is what necessitates a compression chicane, leading to CSR, which in turn will spoil the emittance  $\epsilon_x$ . If the FEL is to function efficiently CSR effects must be carefully controlled.

### 3.3. ACCELERATOR COMPONENTS

In this section we will provide an overview of the core components of the JLab FEL with a focus on the magnetic optics used to provide longitudinal manipulation and compression of the beam. We will then describe the experiment setup used to measure the impact of CSR on the beam as function of the maximum compression point in the beamline.

**3.3.1. THE INJECTOR.** The injector for the JLab FEL is a 325-kV DC GaAs photocathode gun. It can provide up to 10 mA of current from bunches with charges between 60-135 pC at a repetition rate of 75 MHz [30]. Use of a DC gun is necessary for efficient CW operation, but does raise issues with space charge as the beam cannot be as rapidly accelerated [31]. Bunches are generated with a length of approximately 13.5 ps. A 1.497-GHz buncher cavity is used to compress the bunch down to around 5 ps before being passed to the booster which consists of two 5-cell SRF cavities that provide acceleration up to an energy of 9-10 MeV. The bunch length is further reduced during this acceleration down to 2.5-3.5 ps.

**3.3.2. THE ACCELERATOR.** The beam from the injector is then merged onto the axis of the accelerator transport line. Acceleration is then provided via three sets of SRF cavity cryomodules with each cryomodule housing 8 accelerating cavities. Two of these cryomodules, the first and third, use standard 5-cell CEBAF superconducting-rf (SRF) cavities that operate at 1.497 GHz and can provide a 5 MV/m gradient. The second cryomodule is based

on an upgraded 7-cell design [32], still at 1.497 GHz, but with a maximum accelerating gradient of 20 MV/m. These three sets of cryomodules allow for a maximum final beam energy of 160 MeV.

Acceleration within the cavities is provided by a longitudinal electric field that has a sinusoidally varying structure. For the approximation of a thin RF cavity, the energy gained by a particle with a longitudinal position  $z$  defined so that a particle for which  $z = 0$  arrives exactly at the synchronous phase  $\phi_0$  and entering with some initial energy  $E_0$  is given by

$$(28) \quad E(z) = E_0 + E_{rf} \cos(kz + \phi_0),$$

where  $E_{rf}$  is the energy gain through the cavity,  $k = \frac{2\pi}{\lambda}$  is the wavenumber. By running the beam off crest, that is  $\phi_0 \neq 0$ , a time energy-correlation will be imparted to the bunch by the spatially varying electric field in the cavity. The nominal operating condition is to run the beam at a phase  $\phi = -10^\circ$  off of the crest (illustrated in Fig. 3.3). This is called the rising-rf side due to the positive slope here. For acceleration on the opposite side of the crest, at  $\phi = +10^\circ$  we have falling-rf acceleration. Running off crest will impart of positive time-energy correlation onto the beam for proper compression. Positioned between each of the cryomodules is a set of quadrupole triplets for providing transverse focusing of the beam.

**3.3.3. MAGNETIC COMPRESSION CHICANES.** As was discussed previously it is desirable to provide a beam with high peak current to the FEL; however, due to space charge forces it is necessary to keep the bunch length long at the injector. One must therefore compress the electron bunch somewhere along the beam transport system prior to passage through the fields of the FEL undulator. Because the beam is ultra-relativistic it is not possible to use

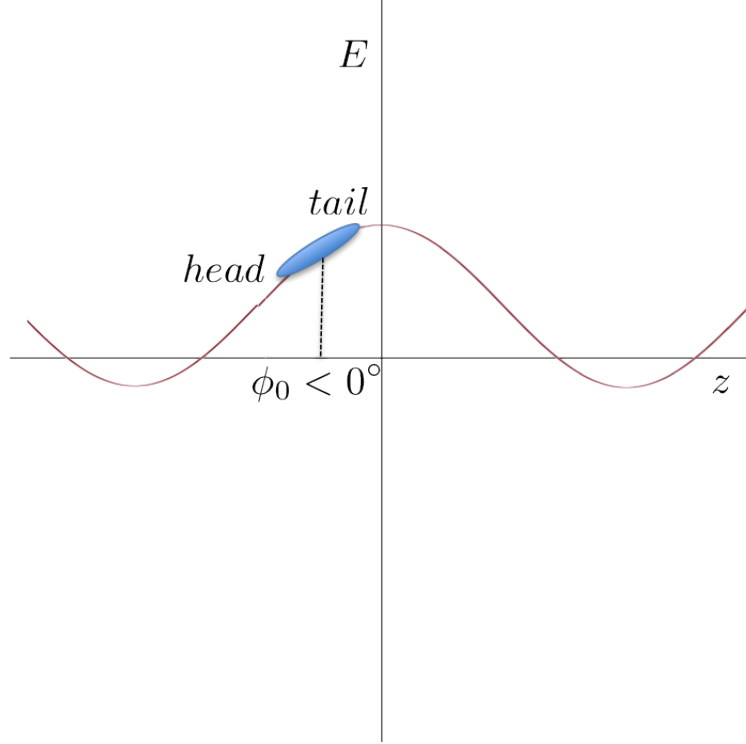


FIGURE 3.3. A bunch accelerated on the rf-wave at phase  $\phi_0 < 0$ , or on the rising-side. The head is at negative  $z$  coordinates with respect to the middle of the bunch while the tail is at positive  $z$  coordinates with respect to the middle.

velocity differences for compression. Instead, shortening of the bunch is normally achieved through a magnetic chicane structure, composed of four dipoles, as shown in Fig. 3.4.

For the chicane to work the bunch must first have a linear correlation between energy and longitudinal position. This can be achieved by passing the bunch off-crest through the linac. If we take the energy gain of particle at position  $z$  within the bunch to be  $E(z)_{linac} = E_0 + E_{rf}\cos(kz + \phi_0)$  and assume that  $kz \ll 1$  then the linear chirp  $h$  is given by

$$(29) \quad h \equiv \frac{dE(z)}{Edz} = -\frac{E_{rf}k\sin(\phi_0)}{E_0 + E_{rf}\cos(\phi_0)}$$

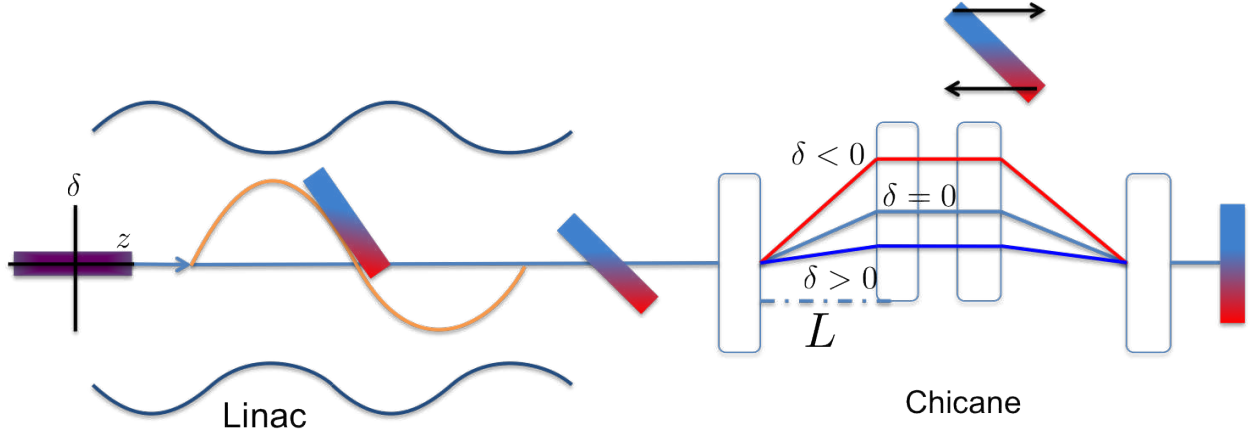


FIGURE 3.4. Schematic of a bunch compression system starting with a bunch passed off-crest through the linac before passing through a four-dipole chicane with legs of length  $L$ .

For particles entering the chicane there will be a deflection dependent on the particle momentum  $\delta = \frac{p-p_0}{p_0}$  taken relative to the reference momentum  $p_0$ . Particles with  $\delta < 0$  will be bent at an angle  $\theta_- > \theta_0$  i.e. greater than that for the central design path and will take a longer path, falling back towards the center of the bunch. Meanwhile, particles for which  $\delta > 0$  will experience a bending angle  $\theta_+ < \theta_0$  and follow a shorter path, catching up to the center of the bunch. In a dipole field the particle on the design energy will be bent at an angle  $\theta_0 = eBl/p_0$ . If each leg of the chicane has projected length  $L$  the induced path length difference for a particle bent through an angle  $\theta(\delta)$  will be

$$(30) \quad \Delta S = \frac{L}{\cos(\theta)} - \frac{L}{\cos(\theta_0)}$$

We can expand Eq. 30, assuming both angles are small, resulting in

$$(31) \quad \Delta S \approx \frac{L}{1 - \frac{\theta^2}{2}} - \frac{L}{1 - \frac{\theta_0^2}{2}} \approx L \left( \frac{\theta^2}{2} - \frac{\theta_0^2}{2} \right)$$

In general the bending angle will vary with momentum like  $\theta/\theta_0 = p_0/p$  leading to the relationship between energy deviation and bend angle of

$$(32) \quad \theta = \frac{\theta_0}{1 + \delta}$$

If this is substituted into Eq. 31 and expanded for  $1/(1 + \delta)^2$  we arrive at the final change in total path length through the (now accounting for both legs)

$$(33) \quad \Delta S = -2L\delta\theta_0^2$$

Or in terms of the  $R_{56}$  matrix element (see Appendix A for description of the transport matrix notation).

$$(34) \quad R_{56} \equiv \frac{\Delta S}{\delta} = -2L\theta_0^2$$

There are, of course, higher-order terms in the path length difference that have been neglected in this analysis that become very important in reality. As will be discussed later, the second-order dependence in  $\delta$  of the path length can exacerbate the curvature imposed by the rf wave and so create a strongly non-linear compression condition that will increase the minimum bunch length and create a very asymmetric current distribution with a long tail, harming the FEL efficiency. As will be shown later this non-linearity, when not corrected, can play an important role in the CSR interaction with the beam.

There are two chicanes in the JLab ERL IR line (see Fig. 3.1). The optical cavity chicane (BC1), which will normally provide final compression for the beam before the undulator, and serves to separate the electron beam from the optical beam at the end of the optical cavity of the FEL. After the FEL there is a second chicane, the THz suppression chicane (BC2). This serves to decompress the bunch before it enters the second recirculation arc. For short bunches entering the first dipole of the second arc there will be emission of CSR, at THz wavelengths (0.1 - 1 mm), which will cause undesirable heating of the FEL optics downstream of the point. By introducing BC2, to over-compress the bunch, this CSR radiation will be greatly reduced, improving FEL performance and reducing the need to shutdown the machine periodically for cooling.

3.3.4. THE BATES BEND. The recirculation arcs A1 and A2 (3.1) are laid out in what is known as the Bates design [33]. A schematic of the design is shown in Fig. 3.5. The design can be thought of as essentially a standard four-dipole chicane that has been split in half and bent around 180 degrees. Also included in addition to the dipole magnets are quadrupoles and sextupoles for control of the first and second order transfer matrix components. This design allows for achromatic and isochronous transport of the beam for recirculation, and also possesses sufficient acceptance to accommodate the large energy spread after the FEL process [34].

This design also has another useful characteristic for an FEL, namely, that through manipulation of the quadrupoles, the important  $R_{56}$ , or momentum compaction, component of the transfer matrix of the arc can easily be changed over a wide range of values, both positive and negative. The second-order  $T_{566}$  term may also be controlled through the use of the sextupoles in the arc. For both cases the same basic principle is used. Dipoles are used to generate a dispersive region where a particle's trajectory is energy dependent. Quadrupoles

and sextupoles are positioned in this region to induce energy dependent transverse kicks to the particle according to  $\Delta x'(x) = -Ax$  and  $\Delta x'(x) = -Bx^2$  where the x-position depends on the dispersion  $\eta$ , that is  $x_\eta = \eta\delta$ .

From the transfer matrix (see Appendix A) for a dipole, Eq. 35, we can see that  $R_{52} = -\rho(1 - \cos(\theta))$ , the term which correlates longitudinal position  $z$  to a particles horizontal momentum  $x'$ . From this the particle pathlength now has a dependence upon the horizontal kick imparted by the quadrupoles and sextupoles and it is possible to change the bunch length purely through manipulation of the quadrupoles and sextupoles. For the 180° bend  $\theta = \pi$  and the path length difference will be  $\Delta z(\delta) = -2\rho\Delta x'$ . It should also be noted that the second Bates bend includes a matching set of octupole magnets [35] to provide third-order correction necessary for managing the energy spread of the beam during the energy recovery process [36]. However, there are currently no octupoles installed in the first Bates bend, and the octupoles in the second bend were not necessary for this experiment as the beam was dumped before recovery.

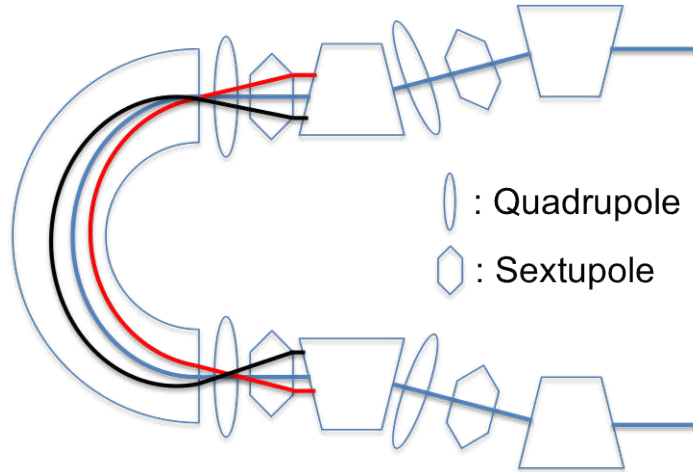


FIGURE 3.5. Schematic of the Bates bend design used in the recirculation arc. Dipoles are represented as trapezoids and in the case of the 180 degree bend by half a donut shape, quadrupoles as ovals, and sextupoles as diamonds. Trajectories for kicked particles are illustrated by the black and red lines, showing the path dependence through the 180 deg bend.

$$(35) \quad M_{dipole} = \begin{pmatrix} \cos(\theta) & \rho \sin(\theta) & 0 & 0 & 0 & \rho(1 - \cos(\theta)) \\ -\frac{\sin(\theta)}{\rho} & \cos(\theta) & 0 & 0 & 0 & \sin(\theta) \\ 0 & 0 & 1 & L & 0 & 0 \\ 0 & 0 & 0 & 1 & 0 & 0 \\ -\sin(\theta) & -\rho(1 - \cos(\theta)) & 0 & 0 & 1 & \frac{\rho \sin(\theta)}{1 - \rho L \beta^2} \\ 0 & 0 & 0 & 0 & 0 & 1 \end{pmatrix}$$

3.3.5. COMPRESSION WITH NONLINEAR EFFECTS. We have already described previously how to manipulate the bunch length to first order using the magnetic compression chicanes and Bates arcs. However, there are also nonlinear effects present, due to the higher-order terms of the sinusoidal rf-wave and nonlinearities which will always be present in the dipoles. To this end we take the longitudinal transport equations through second order in the accelerator to describe how maximum compression may be achieved through correction of the second-order nonlinearity. For longitudinal transport  $(z, \delta)$  through the linac we have

$$(36) \quad z_l = z_0,$$

$$(37) \quad \delta_l = \delta_0 + R_{65}^{\text{linac}} z_0 + T_{655}^{\text{linac}} z_0^2.$$

Here the subscript '0' indicates the particle coordinates at the linac entrance, 'l' for the linac exit, and 'w' for the wiggler entrance. If we neglect any impedance effects on the beam through the rest of the accelerator the longitudinal transport equations up to the undulator are given by:

$$(38) \quad z_w = z_l + R_{56}^{\text{und}} \delta_l + T_{566}^{\text{und}} \delta_l^2,$$

$$(39) \quad \delta_w = \delta_l.$$

By substituting Eqs. 36 and 37 into Eq. 38 we find the final longitudinal transport solution at the undulator

$$(40) \quad z_w = (1 + R_{65}^{\text{linac}} R_{56}^{\text{und}}) z_l + (R_{56}^{\text{und}} T_{655}^{\text{linac}} + T_{566}^{\text{und}} R_{65}^{\text{linac}^2}) z_l^2.$$

Where we have kept up to the quadratic terms in  $z_l$ . Since we only have quadrupole and sextupole magnets in the first arc we cannot manipulate any terms past the second order. Our goal here is to minimize the bunch length, which is equivalent to ensuring that  $z_w = 0$  at the undulator for any initial longitudinal particle position  $z_1$ . From Eq. 40 we can see that the conditions for the linear and quadratic terms respectively are then

$$(41) \quad R_{56}^{\text{und}} = -\frac{1}{R_{65}^{\text{linac}}},$$

$$(42) \quad T_{566}^{\text{und}} = -\frac{R_{56}^{\text{und}} T_{655}^{\text{linac}}}{R_{65}^{\text{linac}^2}}.$$

It is more suitable to cast these conditions in terms of the settings of the linac by using the rf energy gain of the bunch in the linac:  $E_{\text{linac}} = E_0 + E_{rf} \cos(kz + \phi_0)$  where  $k$  is the wavenumber of the rf and  $\phi_0$  is the central accelerating phase of the bunch. Expanding  $E_{\text{linac}}$

out to second order for small values of  $z$  and putting the energy in terms of  $\delta_{linac} \equiv \frac{E_{linac} - E_c}{E_c}$  where  $E_c$  is the central design energy of the linac

$$(43) \quad \delta_{linac} \approx \frac{E_0 + E_{rf} \cos(\phi_0) - E_c}{E_c} - \frac{E_{rf}}{E_c} k \sin(\phi_0) z - \frac{E_{rf} k^2 \cos(\phi_0)}{2E_c} z^2.$$

We can now see that in the linac  $R_{65}^{linac} = -k E_{rf} \cos(\phi_0)$  and  $T_{655}^{linac} = \frac{k^2 E_{rf} \cos(\phi_0)}{2}$ . Substituting these terms from Eq. 43 into Eqs. 41 and 42 we find a more useful description for achieving maximum bunch current for the FEL

$$(44) \quad R_{56}^{und} = \frac{E_c}{k E_{rf} \cos(\phi_0)},$$

$$(45) \quad T_{566}^{und} = -\frac{E_c^2 \cos(\phi_0)}{2 E_{rf}^2 k \sin^3(\phi_0)}.$$

This result matches with the original design specifications [37]. The condition derived here will also be seen to be important for correctly describing CSR energy-loss in the beam, as well as correcting CSR-induced fragmentation of the bunch.

### 3.4. DESCRIPTION OF THE EXPERIMENT

The primary goal of our experiment on the JLab FEL system was to examine the impact of CSR on the beam as a function of compression. While similar experiments have been described before [28, 38] these previous experiments were limited to adjusting compression by varying the chirp on the beam through adjustment of the accelerating phase. The JLab FEL system is more flexible in that regard and manipulation of the longitudinal phase space can be achieved not only by varying the RF phase (as in Eq. 44) but also through manipulation

TABLE 3.1. Nominal beam parameters for the experiment and relevant characteristics of the machine.

Symbol	Description	Value
$E_0$	Injection energy [MeV]	10
$E_f$	Final energy [MeV]	135
-	Charge per bunch [pC]	135
$\sigma_0$	Bunch length after injector [ps]	3.3
$\sigma_f$	Bunch length at max compression [fs]	150
h	Energy-position correlation (chirp) [ $m^{-1}$ ]	$\mp 5$
-	RF phase [degrees]	$\pm 10$
-	RF frequency [GHz]	1.497
$R_{56}^{BC1}$	Optical cavity chicane $R_{56}$ [cm]	-52
$R_{56}^{BC2}$	THz suppression chicane $R_{56}$ [cm]	-4.6
$R_{56}^{A1}$	Bates arcs $R_{56}$ [cm]	-7.5 to 85

of quadrupoles in the recirculation arc. This allows for a much broader exploration of the parameter space and for the opportunity to produce multiple compression points outside of the longitudinally dispersive regions while at the same time removing the impact on energy spread that comes with adjustment of the accelerating phase. Furthermore, the parameters of the beam, namely, the larger transverse emittance mean that conditions in the compression sections of the accelerator are much farther into the region where 2-D CSR effects are believed to be important allowing for a more closer examination of the approximations made in the theories and dependent simulations.

During the experiment the FEL remained off and the beam was not fully recirculated for energy recovery, but was instead dumped at the tune-up dump shown in Fig. 3.1. A full description of relevant machine parameters during the experiment are given in Table. 3.1.

3.4.1. ENERGY LOSS MEASUREMENTS. To perform these measurements the quadrupoles labelled MQT2F07, MQT2F08, MQT2F09, and MQT2F10 in A1, shown in Fig. 3.6, were scanned to adjust the total  $R_{56}$  in the machine. To maintain achromaticity the quadrupole settings across the arc must be mirrored. That is  $K_1^{(07)} = K_1^{(10)}$  and  $K_1^{(08)} = K_1^{(09)}$  where the superscript for the quadrupoles strengths  $K_1$  denotes the quadrupole in Fig. 3.6. The second

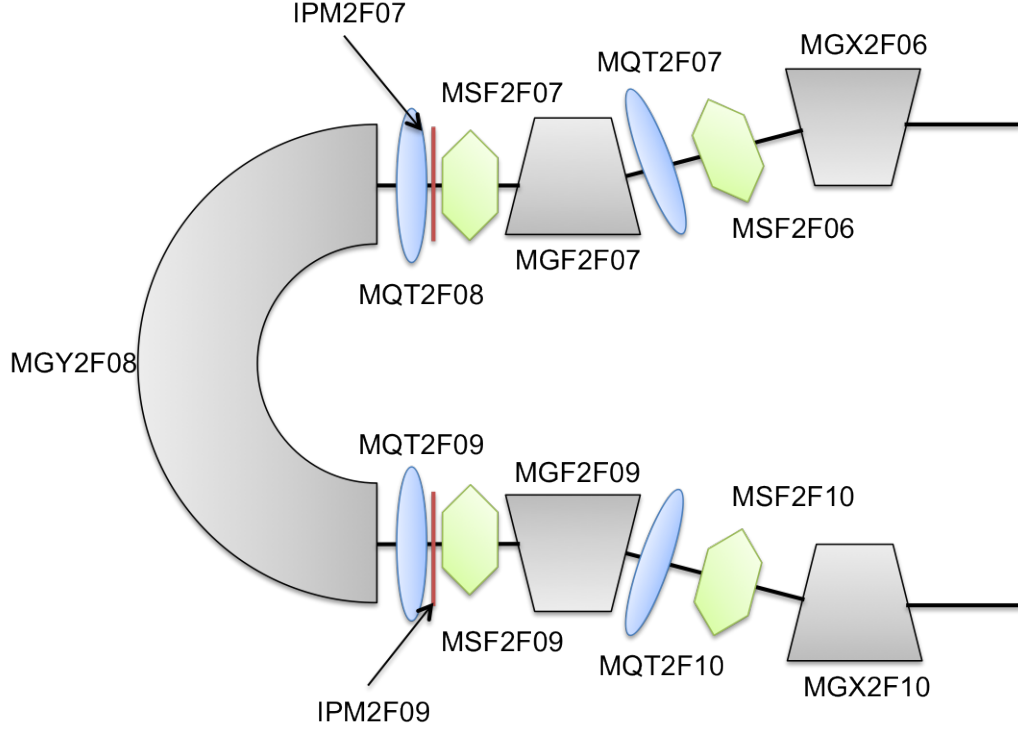


FIGURE 3.6. Layout of the first arc (A1) section of the JLab FEL. Dipoles are represented by gray trapezoids, quadrupoles are blue ovals, and sextupoles are shown as green diamonds. Two beam position monitors are represented by vertical red lines.

condition that must be maintained is that  $K_1^{(08)}/K_1^{(07)} = -7$  to keep the horizontal, angular dispersion  $\eta'_x \approx 0$  at the midpoint of the bend, and allow horizontal dispersion  $\eta_x$  to go to zero at the end of the arc. By the first condition this must also hold for the quadrupoles on the second half of the arc.

As the momentum compaction in the arc,  $R_{56}^{A1} = -2\rho\Delta x'$ , is changed by adjustment of the horizontal kick  $\Delta x'$ , through manipulation of the quadrupoles in the arc, the bunch can be made to compress at different positions along the beamline. This change in compression position can then be observed by watching the CSR-induced energy loss of the bunch. The energy loss is monitored through the use of beam position monitors (BPMs) placed in dispersive regions of the beamline. In these regions the coupling of  $x$  to  $\delta$  will cause the centroid of the beam to shift as a function of offset from the central design energy of the

accelerator. We use an interesting feature of the Bates bend to help us with this measurement. The first order beam optics through the  $180^\circ$  dipole of the Bates bend produces a point-to-point image in the horizontal plane (see Appendix B for a description of the standard accelerator coordinate system) with a magnification of  $-1$ . This can be seen by again looking at Eq. 35, the transfer matrix for a dipole. For a bend angle of  $180^\circ$  the dipole matrix components  $R_{12} = R_{21} = 0$  providing point-to-point imaging and  $R_{11} = R_{22} = -1$  providing the  $-1$  magnification. If one averages the beam position at the entrance and exit of the bend then any betatron motion is canceled and the result is directly proportional to the beam energy and not to beam steering errors upstream of the measurement.

Jitter in timing system, and phases and voltages in the rf, however, can throw off this measurement. This jitter will cause changes in the average bunch energy and thus change the central path of the beam through the machine. Consequently, this will induce shot-to-shot variation in the BPM measurements. To adjust for the jitter another set of measurements are taken using BPMs in the first arc (IPM2F07 and IPM2F09 in Fig. 3.6), that are similarly averaged together. The beam will not have yet compressed at this point, and will have no energy loss to CSR, thus this measurement serves as a baseline (see Fig. 3.7(a) and (b)).

A second measurement is then taken using the BPMs in the second arc. Due to CSR energy losses accrued upstream from this position the average bunch energy will have changed by the time the bunch reaches this position. The shift in the bunch centroid position will then be a function of this energy loss from CSR, allowing for a measurement of CSR-induced energy loss. The BPM data from the second arc is shown in Fig. 3.7(c) and (d).

From this we arrive at the final result by now subtracting out the baseline measurement shown in 3.7(a) and (b) from the energy loss data in (c) and (d) respectively. This result is shown in Fig. 3.8.

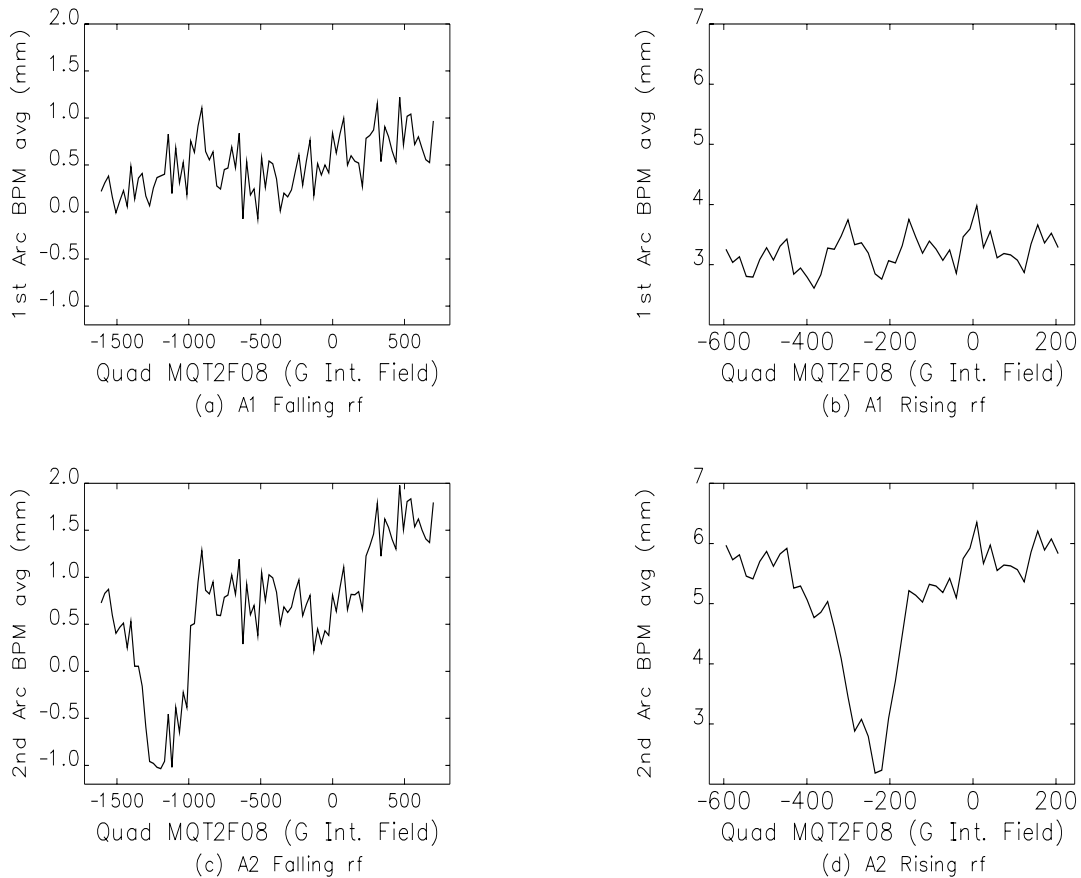


FIGURE 3.7. Plots of beam centroid position as function of integrated quadrupole field (in units of Gauss) in A1, where (a) and (b) are the BPM readings in the middle of A1 for falling-rf and rising-rf acceleration respectively and (c) and (d) are the BPM readings in the middle of A2 for falling-rf and rising-rf acceleration respectively.

We have already discussed that one novel factor for performing CSR studies on the JLab ERL is the wide range of compression dynamics which are possible in the machine. Here we now see this action. For Fig. 3.8(a), the falling side (for an accelerating phase  $\phi = +10^\circ$ ), we can resolve two distinct compression points along the beamline. We will later see that there is an additional compression point that is missing in this data due to the sextupole settings. In Fig. 3.8(b), the rising side (for an accelerating phase  $\phi = -10^\circ$ ), we observe two compression points. Here we are limited by the scan range, which is much smaller than

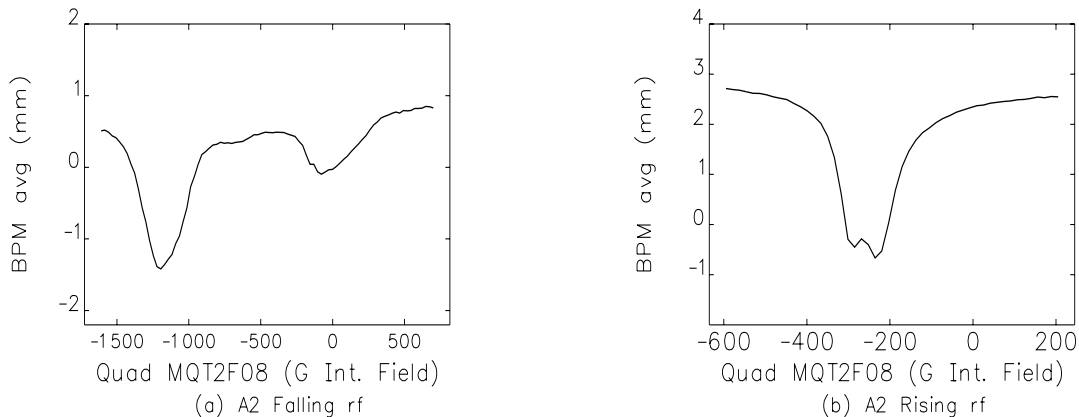


FIGURE 3.8. Plots of beam centroid position with the baseline reading subtracted from the energy loss data. The data for falling-rf acceleration is shown in (a) and the rising-rf acceleration data is shown in (b).

that used for the falling side. However, we observe the compression point after both BC1 and BC2 (Fig. 3.1), which is missing from the falling side.

To understand where each feature of these plots arise it is helpful to review how the bunch rotates in the longitudinal phase space as a function of the  $R_{56}$  settings. To help illustrate the complicated longitudinal dynamics of the JLab FEL we will use plots like the one shown in Fig. 3.9. Here the beamline is illustrated along the bottom of the plot. The linac sections are presented as an oscillating line, the quadrupole magnets as tall, vertical lines, finally the dipoles are the short rectangles. The compression of the bunch given by  $C = (1 + hR_{56})^{-1}$  is plotted along the beamline. Finally, centered around the representation of the beamline elements is a plot of the sign of the chirp,  $h$ ,  $sgn(h) = \langle s\delta \rangle / |\langle s\delta \rangle|$ . The significance of  $sgn(h)$  being that whenever the chirp switches sign from positive to negative the bunch passes through full compression. In this plot  $sgn(h) = +1$  is represented by the blue line being above the beamline representation while  $sgn(h) = -1$  is below.

For the falling side case, which has a negatively chirped bunch, the first Bates arc (A1 in Fig. 3.1) has a large negative  $R_{56}$  contribution from the second dipole that dramatically

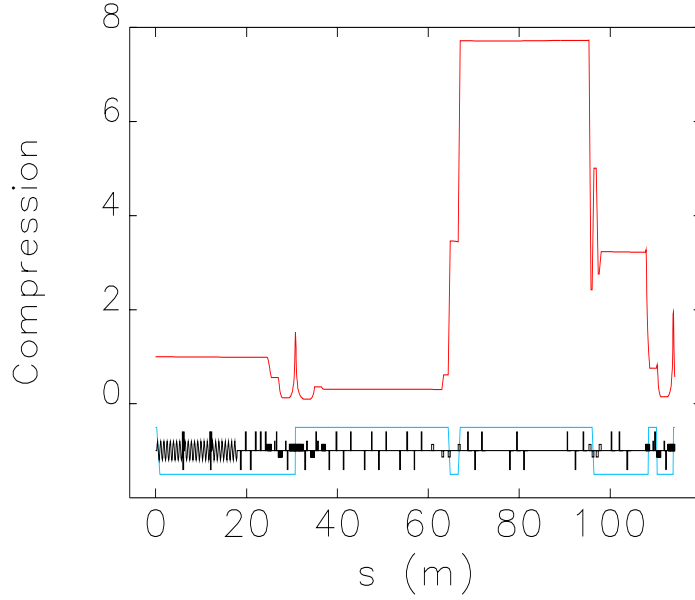


FIGURE 3.9. Example plot showing the beamline elements along the bottom in black, with the compression of the bunch (defined as  $\text{Compression} = (1 + hR_{56})^{-1}$ ) in red, and the sign of the chirp,  $h$ , plotted in blue.

increases the bunch length, but will keep the same sign for the chirp. As the bunch traverses the 180 degree dipole, it is rapidly over-compressed, reversing the initial orientation of the head at high energy and tail at low energy so that at the dipole exit the head is at low energy and the tail is at high. This is shown in Fig. 3.10 with the middle of the 180 degree dipole at 30 m. After this rapid parasitic compression, the remainder of the transport to the second arc will then compress the bunch, with the location of the shortest bunch length depending on the  $R_{56}^{\text{A1}}$  setpoint of the first arc.

If the  $R_{56}$  in the first arc is large and positive (e.g.,  $R_{56}^{\text{A1}} \sim 1$  m), the downstream chicanes do not have adequately large negative momentum compaction to fully compress the bunch; instead, it is fully compressed only when it reaches the second dipole of the second arc, where the large negative  $R_{56}$  contribution from that dipole can serve to reduce the bunch length.

As in the first arc, the 180 degree dipole then reverses the sign of the chirp, introducing yet another parasitic compression, see Fig. 3.10(A).

As the  $R_{56}$  of the first arc is reduced from large positive values, the compression point moves upstream through the machine. At  $R_{56}^{A1} \sim 0.75$  m the bunch is fully compressed at the end of the THz chicane, as in Fig. 3.10(B); further reduction to  $\sim 0.7$  m moves the point to the end of the optical cavity chicane just upstream of the undulator. In this case with full compression at the end of the chicane, the bunch undergoes two parasitic compressions. The initial cross-over is, as described above, in the arc; the second cross-over is in the third dipole of the chicane, where the bunch must be slightly over-compressed which will insure the bunch is fully compressed after traversing the final dipole, which provides a small positive contribution to the momentum compaction. This scenario is shown in Fig. 3.10(C).

Further reduction of the first Bates arc  $R_{56}$  moves the compression point upstream as shown in Fig. 3.10(D). When  $R_{56}^{A1} = 0.2$  m, the bunch is fully compressed at the end of the Bates arc itself, Fig. 3.10(E). As the momentum compaction is lowered past zero the bunch will fail to compress (except for parasitically) at any point, Fig. 3.10(F). This covers the three possible compression points achievable in a non-dispersed region upstream of A2 when the bunch is accelerated at 10 degrees past the crest of the RF waveform. For  $R_{56}^{A1} = 0.75$  m the beam is compressed following the THz chicane; for 0.7 m it is compressed between the optical cavity chicane, through the undulator, and up to the THz chicane; for 0.2 m it is compressed between the first Bates arc and the optical cavity chicane. All other values result only in rapid parasitic compressions at locations where the beam is transversely dispersed.

For acceleration on the rising-rf side the three key compression points, at the end of A1, the end of BC1, and the end of BC2 (the first and second chicanes in Fig. 3.1), will remain unchanged. However, dynamics in A1 will differ considerably. A bunch with positive

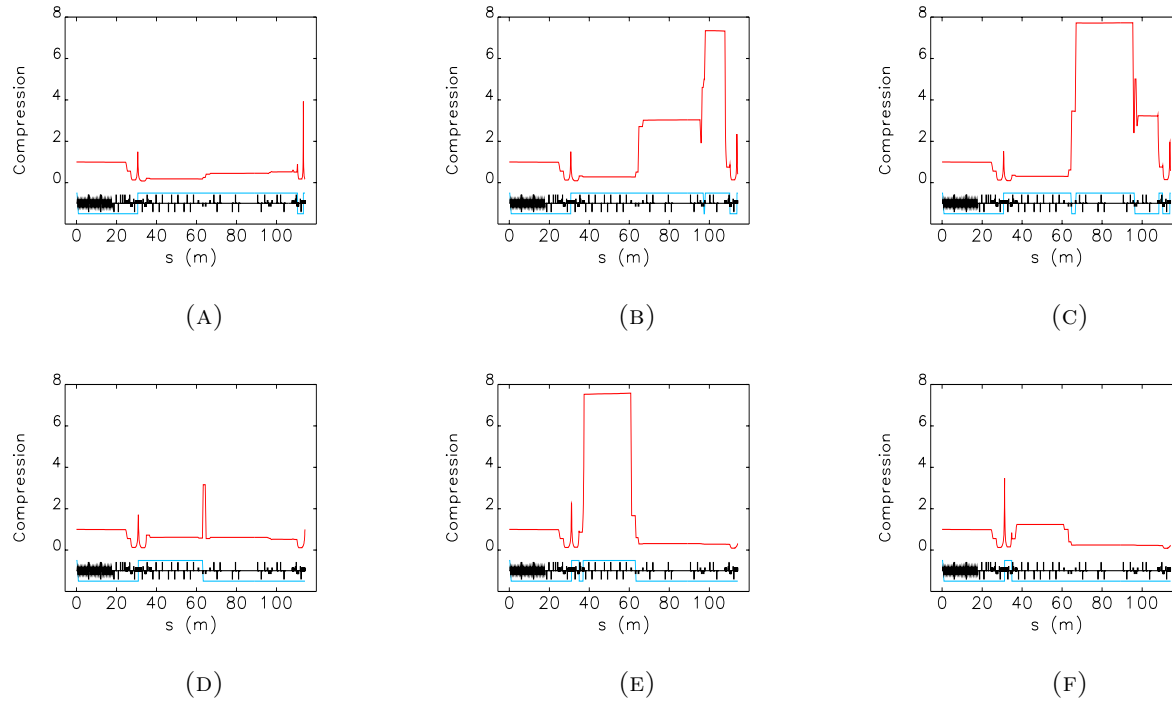


FIGURE 3.10. For falling rf acceleration the compression ratio (red) and the normalized sign of the chirp (blue) are plotted along the beamline. Shown in (A) - (C) are the undercompressed, fully compressed, and overcompressed cases for BC1 compression. The same are represented in (D) -(F) for compression in the first arc. Parasitic compressions can be observed when the sign of the chirp (blue) changes, then changes back in a single dipole.

chirp will undergo a rapid compression as it traverses the large  $R_{56}$  contributed by the second dipole of the first Bates arc, and change the sign of the chirp. A second parasitic compression then soon follows as the bunch moves through the (large positive momentum compaction of the) 180 degree dipole and the head and tail are again reversed, restoring the initial positive chirp. The ensuing dynamics then, as before, depend on the momentum compaction setpoint of the Bates arc. If  $R_{56}^{A1}$  is large and positive, the bunch is, again, fully recompressed only when it reaches the second dipole in the downstream Bates arc. As the momentum compaction is reduced, the compression point again moves forward, with the bunch being fully compressed between the THz-suppression chicane and the second arc when  $R_{56}^{A1} \sim 0.35$  m, in Fig. 3.11(A). Further reduction to  $R_{56}^{A1} = 0.3$  m puts the machine into the nominal lasing configuration, with the bunch fully compressed ( Fig. 3.10(B)) between the optical cavity and THz chicane with the undulator. As above, an additional parasitic compression, the third of such, occurs in the third dipole of the optical cavity chicane when the bunch is brought to full compression in this region.

Further reduction moves the compression point upstream through the optical cavity chicane Fig. 3.11(C). The beam will only reach full compression in the arc-to-chicane nondispersed transport for  $R_{56} = -0.2$  m. However, in the experiment the momentum compaction was not swept that far. It is of interest to note, however, that though the notional design dynamics of this system generate bunch compression using a positive chirp, there is actually one fewer parasitic compression when the system is operated with acceleration on the falling side of the RF waveform. This suggests that non-standard operation with a negative chirp may actually provide superior performance [39].

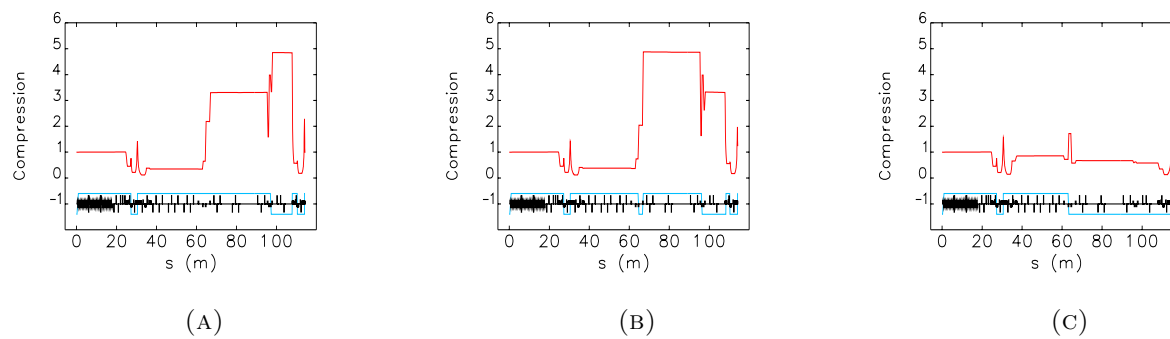


FIGURE 3.11. For rising rf acceleration the compression ratio (red) and the normalized sign of the chirp (blue) are plotted along the beamline. Shown in (A) - (C) are the undercompressed, fully compressed, and overcompressed cases for BC1 compression. Parasitic compressions can be observed when the sign of the chirp (blue) changes, then changes back in a single dipole.

3.4.2. ENERGY SPECTRUM MEASUREMENT. A synchrotron light monitor (SLM) was operated in the second recirculation arc, A2 in Fig. 3.1, during measurement on the falling-rf side. At this position the beam is transversely dispersed, coupling the transverse position to energy. Particle position is determined by  $x(s) = x_\beta(s) + \eta(s)\delta$ , where  $x_\beta$  is the betatron component of the position. By minimizing the betatron function  $\beta_x$  the position  $x(s)$  will be dominated by the dispersion  $\eta \equiv dx/d\delta$ . As the beam radiates in the dipole the measurement from the synchrotron light monitor will provide a picture of the beam's energy spectrum.

While measurement of the CSR energy losses with the BPMs provides a picture of how the bunch changes on average as a function of compression it is also vital to gain some understanding of what is happening within the bunch. Because the CSR field varies along the bunch, and is itself a function of the bunch's longitudinal density it is essential that we be able to see more than just the averaged properties of the bunch. By taking a measurement of the energy spectrum as a function of compression we gain better insight, albeit indirectly, into how the CSR wake is impacting different longitudinal slices of the bunch, and how to minimize this impact.

An example of the output from the SLM is shown in Fig. 3.12. Because CSR energy loss is not uniform over the length of the beam it is possible for the energy spectrum to 'fragment' and develop several peaks and valleys, seen in comparing Fig. 3.12(A) to (B). LSC also appears to strongly enhance this effect, as will be shown later. Monitoring for this effect provides a method for checking for possible microbunching. With the multiple longitudinally dispersive regions present in the JLab FEL such fragmentation in energy could possibly be converted to density fragmentation.

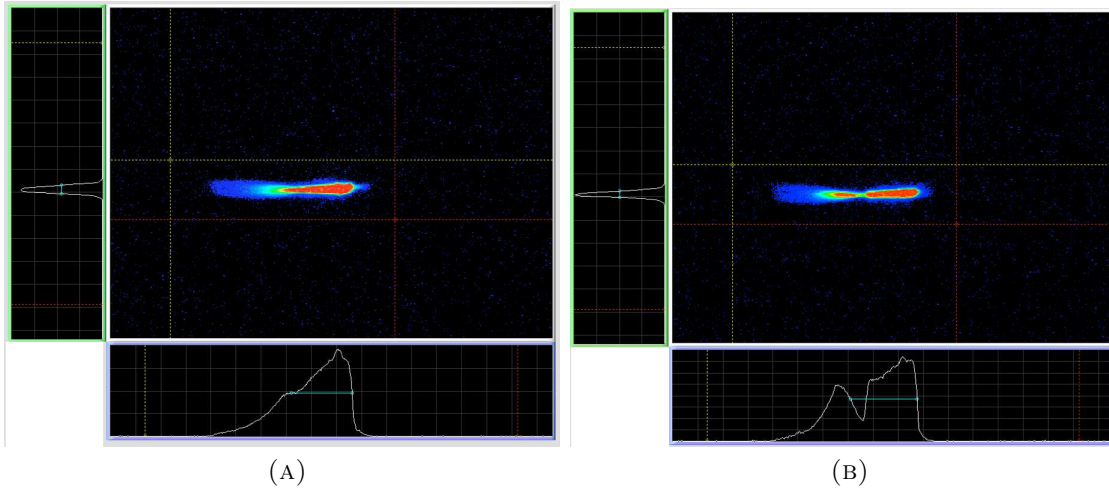


FIGURE 3.12. Examples of the beam distribution from the synchrotron light monitor operated in A2. Plots to the left and below the center image show the projection of the y and x distributions respectively. The x-distribution corresponds directly to the energy spectrum of the beam. Shown in (A) is an example of the spectrum for an uncompressed bunch. Shown in (B) is the spectrum of a bunch that has compressed at the end of BC1.

## CHAPTER 4

# ANALYSIS WITH A 1-D CSR MODEL

### 4.1. MODELING COLLECTIVE EFFECTS

The longitudinal dynamics of the beam and CSR-beam interaction represent a complicated system. To ensure we fully understand the results of our experiment it is necessary that we be able to represent the experiment in simulation in a manner that will capture these aspects. There exist a wide variety of codes for the simulation of accelerators. These employ a number of different techniques to ensure that the physics is correctly captured in different regimes. For our simulation we choose to employ the code `elegant` [40]. `elegant` is a macroparticle tracking code that provides single particle tracking through a large variety of included field element types. This tracking can be performed via transfer matrices, up to second order in most element types; canonical integrators, up to fourth-order are also available for dipoles, quadrupoles, and sextupoles. However, `elegant` does not, in general, model the collective interaction of the bunch. It does, though, include specialized elements for tracking beams with CSR and longitudinal space charge (LSC) effects included, utilizing one-dimensional approximations of both these collective effects. Coherent synchrotron radiation modeling is available in `elegant` in dipoles and in drift sections immediately following a dipole. The 1D model of Saldin et al. [19], discussed in Chapter 2 is used. The calculation of LSC forces is available with rf cavities and drifts. A 1D model [41], also discussed in Chapter 2, is used to calculate the LSC force on the beam within these elements.

In this chapter we will first detail the setup of the `elegant` simulations and calibration of the measurement results. Comparisons between simulation and measurement are shown

and explanations of a number of key features of the experimntal results are discussed with the aid of the simulations.

## 4.2. CONTROLLING NUMERICAL NOISE

While the CSR wake may be readily computed using the method outlined in Chapter 2 this calculation requires both a numeric derivative and integration. In `elegant` the wake is computed by binning the longitudinal distribution, smoothing the resulting histogram with a fast-Fourier transform convolution utilizing a Savitzky-Golay filter [42], and then taking the derivative of this distribution and subsequently integrating. Care must therefore be taken during this process to ensure that the result does not overly suffer from noise. Furthermore, due to the fact that each particle can loose or gain energy from the CSR wake proper modeling requires that we split the dipole into a number of slices. At the end of each slice a fourth-order canonical integration is used to calculate the kick on the beam due to the dipole fields, and following this the energy change from the CSR wake is applied. This gives a number of parameters for the simulation that must be carefully checked to ensure proper convergence of the results. For this reason we first look at varying the macro-particle count in the simulation, the number of bins used in the histogram, and the number of dipole kicks.

The macroparticle count is set at the start of a simulation when `elegant` is used to create a beam. Since we begin our simulations with a bunch starting at the linac entrance, without the benefit of an injector simulation that can properly handle the space-charge forces in that region, we must use an idealized bunch distribution. We choose to use a beam with Gaussian distributions in the transverse planes and a top-hat distribution in the longitudinal plane. Our main concern here is guaranteeing that the bunch will contain sufficient particles such

that binning for the CSR calculation will not be overly subject to noise. As figures of merit to check for convergence we examine both  $\langle\delta\rangle$  the average fractional deviation of the beam energy at the end of the beamline and the horizontal emittance  $\epsilon_x$ . The parameter  $\langle\delta\rangle$  is one of the primary measured quantities of our experiment, while for  $\epsilon_x$  we expect it to be strongly impacted by CSR. As the CSR wake reaches convergence the projected emittance growth should also converge. Surprisingly, we see in Fig. 4.1 that there is little discernible convergence for  $\langle\delta\rangle$  over greater than two order of magnitude variation in particle number. For  $\epsilon_x$  the situation is slightly better but there is still not strict convergence even out to 5 million particles. The main constraint then for choosing particle number for our simulations is runtime. To keep simulation times for a full run to around twenty-four hours we settle for 200,000 macroparticles.

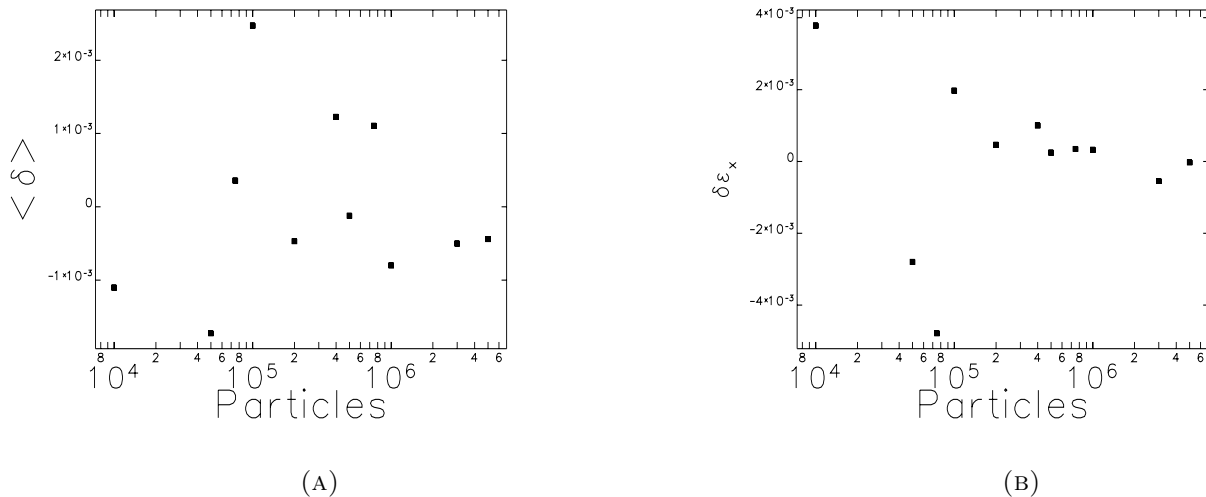


FIGURE 4.1. Scan over the number of particles in the simulation. Shown in (A) is  $\langle\delta\rangle$  as a function of the number of particles and in (B)  $\delta\epsilon_x$ , the fractional deviation of the emittance as a function of the number of particles.

In *elegant* CSR can only be produced within dipoles. As previously discussed, part of the process for calculating the CSR field requires that the longitudinal distribution be binned prior to taking the derivative. It is important to make sure than a sufficient number

of bins is being used to guarantee convergence of the calculation or else the CSR field will again suffer from noise and its contribution may be severely underestimated. To test the effect of binning we vary the number of bins used in taking the histogram of the longitudinal density from 100 - 1000 and run our simulation with the quadrupoles of A1 set for maximum compression after BC1.

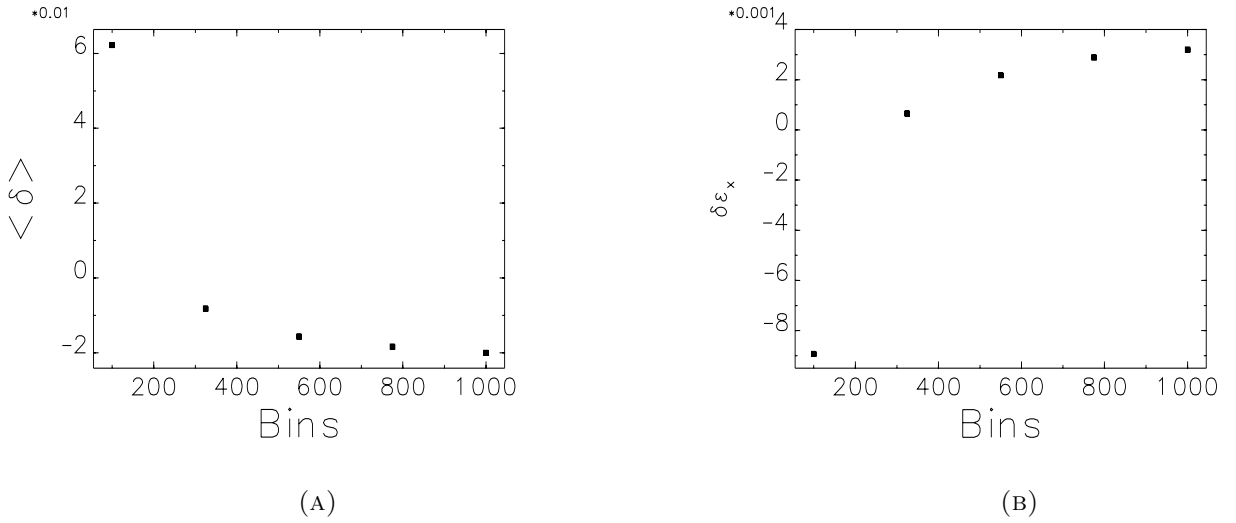


FIGURE 4.2. Scan over the number of bins used in each dipole to calculate the shape of the CSR wake. Shown in (A) is  $\langle \delta \rangle$  as a function of the number of bins and in (B)  $\delta \epsilon_x$ , the fractional deviation of the emittance as a function of the number of bins.

In Fig. 4.2 we see that the energy loss  $\langle \delta \rangle$  and transverse emittance  $\epsilon_x$  converge as bin number is increased. However, past 300 bins there is a relatively small change. Due to the increased time required for computation as bin number is raised we choose to use 300 bins per dipole kick for the CSR calculation.

For the so-called CSRDRIFT element in `elegant` the initial wake is taken from the output of the dipole immediately upstream of the drift. The calculated CSR energy change is then applied to the beam at regular increments. The step size for these increments must also then be checked for good convergence. Shown in Fig. 4.3 are the energy loss  $\langle \delta \rangle$  and

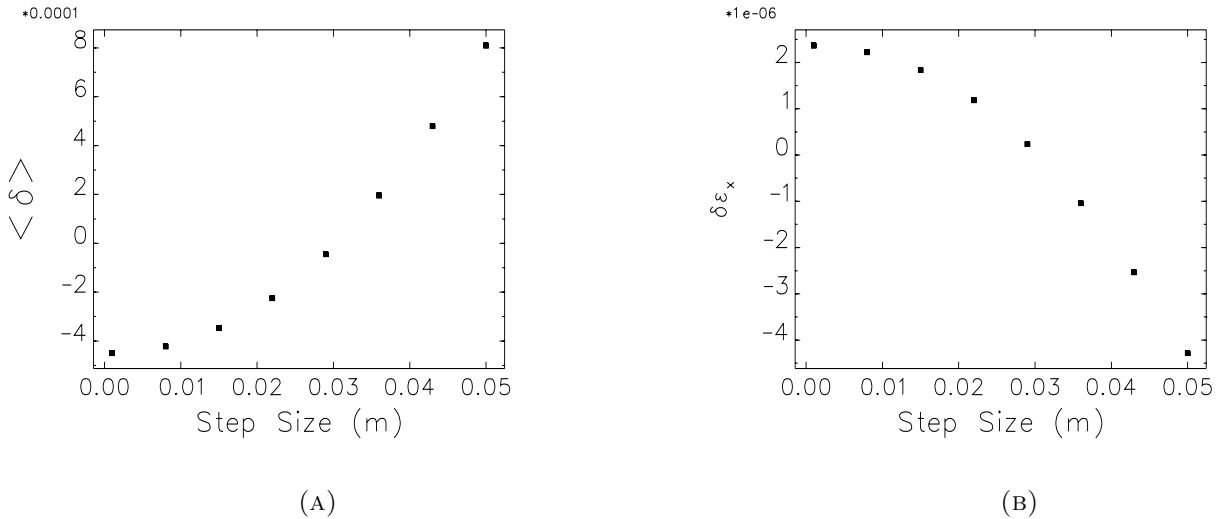


FIGURE 4.3. Scan over the step size interval at which the CSR wake calculation is performed in CSRDrift elements. Shown in (A) is  $\langle \delta \rangle$  as a function of the step size and in (B)  $\delta \epsilon_x$ , the fractional deviation of the emittance as a function of the step size.

transverse emittance  $\epsilon_x$  as a function of step size for the CSRDRIFT beamline elements. The convergence for step size is not as rapid but we note that the difference even between the largest and smallest step size is a few thousandths. For the step size we settle on a value of 0.01 m as a reasonable trade-off between computational effort and numerical convergence. It is not necessary to test for convergence of bin number for the CSRDRIFT calculation as the bin number is determined by the upstream dipole, and thus was accounted for in our previous test of binning.

### 4.3. MEASUREMENT CALIBRATION

The final step to be made before a full comparison between simulation and measurement may be made is to calibrate the raw data from the experiment. The energy loss measurements were taken based upon centroid position of the beam in the horizontal plane. This must be calibrated to energy loss based on the dispersion at the BPM positions. Second, the energy loss is varied in the experiment as a function of the momentum compaction along the

beamline, which is manipulated through control of the quadrupoles in the A1 arc. We must, therefore, also convert the quadrupoles settings to the more useful measure of momentum compaction in the A1 arc.

To calibrate the energy loss measurement from the BPMs we first find the dispersion at the BPMs, defined as  $\eta_x(s) = \frac{dx(s)}{d\delta}$ . This value will vary slightly with the setting of the quadrupoles in the arc. This variation may be found from a tracking simulation of the arc as there was no direct measurement taken. Shown in Fig. 4.4 is the dispersion as a function of the trim quadrupole MQT2F08. The position of the bunch centroid will then be based on  $\langle x \rangle_{BPM} = \eta_x \langle \delta \rangle + x_{offset}$ . Where  $x_{offset}$  is some static offset in the centroid position of the bunch. To estimate the offset in the centroid position we use the measurement of  $\langle x \rangle_{BPM}$  at the maximum and minimum quadrupole strengths, where the bunch should be long and losing little energy to CSR and thus be on its nominal trajectory ( $\delta \approx 0$ ). These two measurements are averaged together and subtracted from the data, to remove any offset, and allow comparison to the simulation where the ideal particle will follow a perfectly centered trajectory.

Finally, we change the independent variable of the measurements from the integrated field strength of quadrupoles MQT2F08 to the total momentum compaction of A1, which is varying as a function of quadrupole strength. The relationship between the two, found from prior tests of the machine, is  $M_T \equiv R_{56}/B_{Quad} = -0.0005 \pm 0.0001$  m/G [43]. By design the nominal offset in the arc, when the quadrupoles are at zero field, is  $R_{56}^{A1_0} = 20$  m. The linear relationship  $R_{56}^{A1}(B_{08}) = M_T B_{08} + R_{56}^{A1_0}$ , where  $B_{08}$  is the integrated field in quadrupole MQT2F08 can be used to calibrate the quadrupole field strength to the momentum compaction of the A1 arc. However, there are two issues with this conversion. First, the error in the phase transfer function measurement ( $\approx 20\%$ ) is not insignificant.

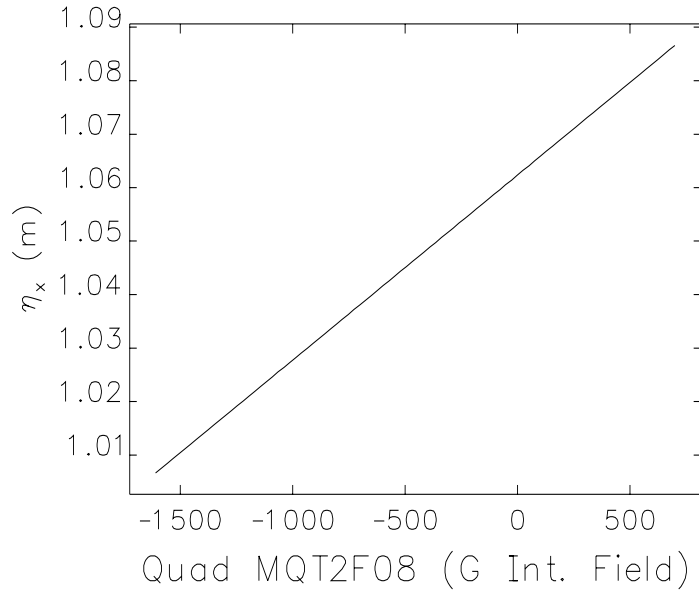


FIGURE 4.4. Dispersion calculated at the arc BPMs as a function of the MQT2F08 quadupole strength.

Secondly, we do not know the true starting longitudinal beam distribution as will be discussed in Sec. 4.4. To determine the calibration for our experiment, then, we add in an empirically determined offset to the slope, within the bounds of the measurement error, to match the measurement and simulation.

#### 4.4. DETERMINING INITIAL BEAM CONDITIONS

Ideally the beam is accelerated on crest through the injector and will arrive at the linac with no time-energy correlation. However, as we do not have a measurement of the distribution from the injector we must assume that this will not be perfectly true. Thus it is important to examine how the results of the experiment would vary with small changes to the chirp. It should be expected that a non-zero chirp at the linac entrance will lead to a small shift in the chirp at the exit and a subsequent change in the momentum compaction needed for full bunch compression. Scans over the accelerating phase and chirp at the linac

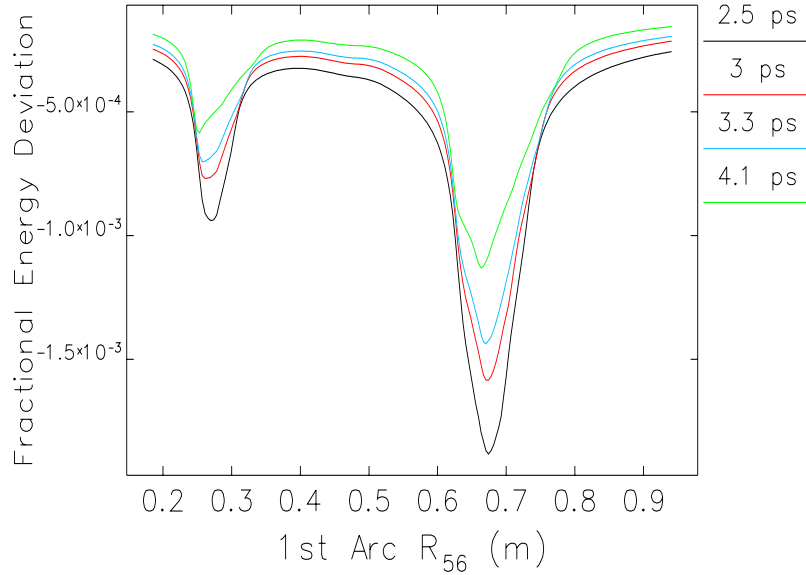


FIGURE 4.5. Comparison of energy loss for acceleration on the falling-rf side for various initial bunch lengths at the linac entrance.

entrance were performed. The minimum difference between the  $R_{56}^{A1}$  for experiment and simulation where maximum energy loss occurred along the entire beamline was found to be for a chirp of  $1 \text{ m}^{-1}$  and linac phase of  $102^\circ$ .

There is also the issue of what the initial bunch length from the injector was during the experiment. This was not directly measured during the course of the experiment and will, of course, have significant impact upon the results. For example, with a Gaussian bunch, energy loss due to CSR will scale as  $\Delta E_{CSR} \propto \sigma_s^{\frac{4}{3}}$ . Due to the bunch length not being fully known, the simulations shown will be run using an initial bunch length of 3.3 ps, as this is the normal operating condition for the injector. A scan over several initial bunch lengths (Fig. 4.5) shows that the magnitude of energy loss is of course altered with initial bunch length but the shape of the energy loss curve remains mostly unaltered.

## 4.5. SIMULATION RESULTS

Now that we have tested numerical convergence, determined appropriate initial conditions for the beam, and completed machine calibration we may now turn to studying the full results of the experiment. Here we will now compare the experimental data against our model of the accelerator implemented in `elegant`. This modeling will help to illuminate several important lessons from the experiment, namely, the role of the sextupoles in CSR emission and its impact back onto the bunch energy distribution, and the role of CSR in drifts after dipoles in impacting the energy distribution. Additional simulations will also show how LSC may contribute strongly to observed fragmentation of the longitudinal phase space and the role of nonlinearities in exacerbating this effect.

4.5.1. RISING RF ACCELERATION. As previously described the normal operating condition for the accelerator is to accelerate the beam on the rising side of the rf wave in the linac. This will impart a chirp  $h > 0$  to the beam. For a phase  $\phi = -10^\circ$  (before the crest) the chirp will be  $5 \text{ m}^{-1}$ . The naturally positive momentum compaction of the A1 arc is enhanced through the quadrupoles to  $R_{56}^{\text{A1}} = 0.3 \text{ m}$  and combined with the BC1 chicane momentum compaction of  $R_{56}^{\text{BC1}} = -0.52$  to provide full compression following that last dipole of BC1 and immediately before the wiggler. For this section of the experiment the quadrupoles in A1 were scanned around this point, varying the momentum compaction, and the energy loss from CSR was measured using the BPMs in A2 as outlined before.

There are two distinct dips observable in the experimental data shown in Fig. 4.6. The first occurs for  $R_{56}^{\text{A1}} \approx 0.34 \text{ m}$ , which corresponds to full compression after BC1. The compression point is slightly higher than the nominal value because of the small negative chirp on the beam entering the linac, decreasing the overall chirp of the bunch. The second

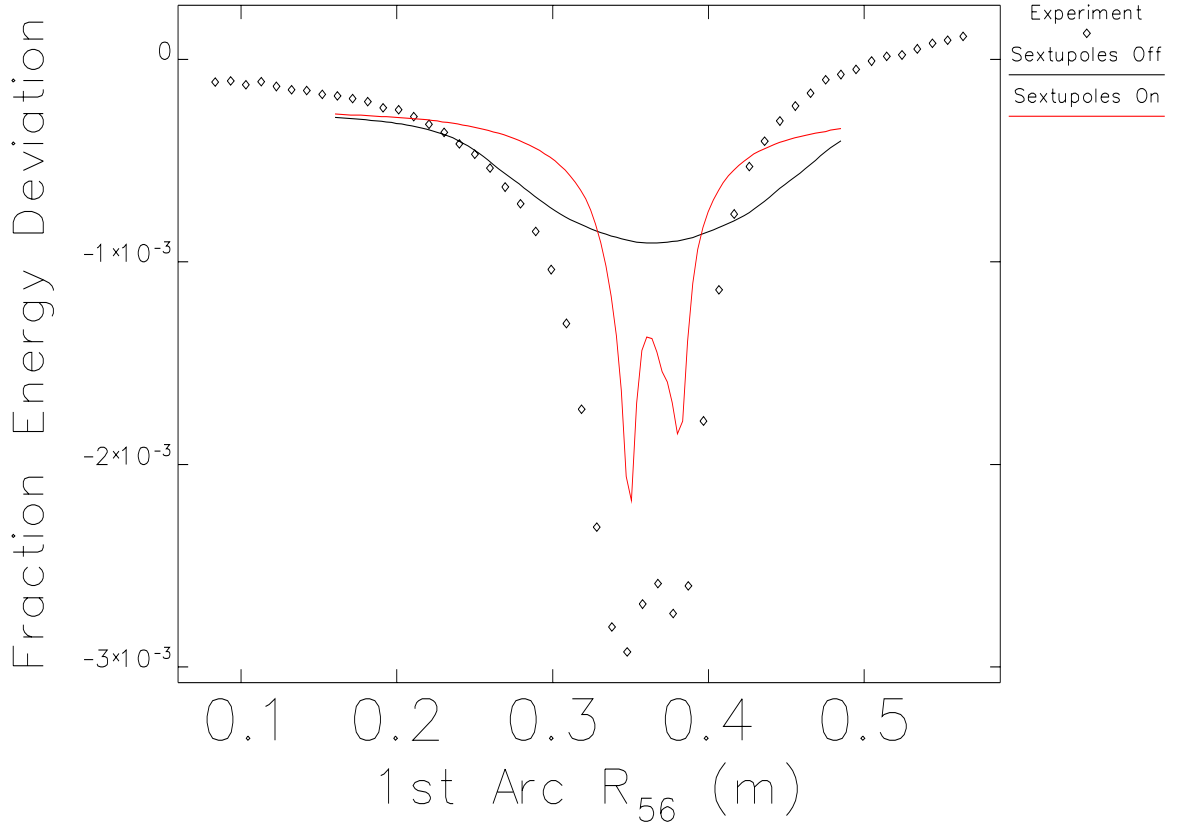


FIGURE 4.6. Fractional energy deviation of the beam as a function of the first arc momentum compaction  $R_{56}^{A1}$  for acceleration on the rising side of the rf. The experimental data is shown with the diamond symbols. The simulation is shown with sextupoles off in black and the sextupoles on in red.

compression point occurs at  $R_{56}^{A1} \approx 0.38$  m. This is due to BC2, the THz-suppression chicane, which has  $R_{56}^{BC2} = -0.046$ . If sufficient positive momentum compaction is generated in A1 the bunch does not get compressed fully by BC1 but does fully compress at the end of BC2. It is important to note that two different sets of simulations were run for comparison to this data. For one, the sextupole magnets in the A1 arc were completely turned off, while in the second the sextupoles were configured to fulfill the linearization condition  $R_{56}T_{655} + (T_{566}^{A1} + T_{566}^{BC1})R_{65}^2 = 0$  derived in Chapter 3. Here  $R_{56}$ ,  $R_{65}$ , and  $T_{655}$  are

the total quantities from the linac entrance up to the end of BC1. The value of  $T_{566}^{\text{BC1}}$  is fixed for the chicane at 0.85 m. The value for the sextupoles to meet  $T_{566}^{\text{A1}}$  is then determined by a simplex optimization routine in `elegant`. As can be observed in Fig. 4.6 the sextupoles clearly play a strong role in the measurement. Comparing the two simulation cases we can see that not only is CSR emission greatly enhanced with the sextupoles but without them it is not possible to see both compression points. That CSR output is greatly increased with use of the sextupoles is not surprising. The purpose of the sextupoles is to correct for the non-linear terms from the sinusoidal curvature of the rf field and the non-linear transport properties of the chicanes and arcs. With this correction implemented the bunch length drops from  $\sigma_t = 412$  fs to  $\sigma_t = 121$  fs after BC1, at full compression, explaining the greater energy loss. The linearization is also necessary for resolving the full-compression point for both chicanes. The mechanism behind this will be demonstrated further on.

4.5.2. FALLING RF ACCELERATION. We now turn to the second half of the experiment, on the falling-rf side. We note here that, unless otherwise stated, all further comparisons to simulation will be for the falling-rf measurement, as it was more complete of the two measurements. On the falling side of the rf  $\phi = +10^\circ$  there is a chirp imparted to the beam of  $h = -5 \text{ m}^{-1}$ . This is an abnormal running condition for most FELs as it gives the incorrect sign on the chirp ( $h < 0$ ) for achieving compression in a standard four-dipole chicane (with  $R_{56} > 0$ ). However, with the ability to provide both negative and positive momentum compaction using the Bates bend, compression can still be achieved after the chicanes. If  $(\Sigma R_{56})_{\text{und}} = R_{56}^{\text{A1}} + R_{56}^{\text{BC1}} = 0.2$  the bunch will fully compress after the BC1 chicane for a bunch exiting the linac with chirp  $h = -5 \text{ m}^{-1}$ , or if  $(\Sigma R_{56})_{\text{A2}} = R_{56}^{\text{A1}} + R_{56}^{\text{BC1}} + R_{56}^{\text{BC2}} = 0.2$  the bunch will fully compress after BC2. For this portion of the experiment the quadrupoles

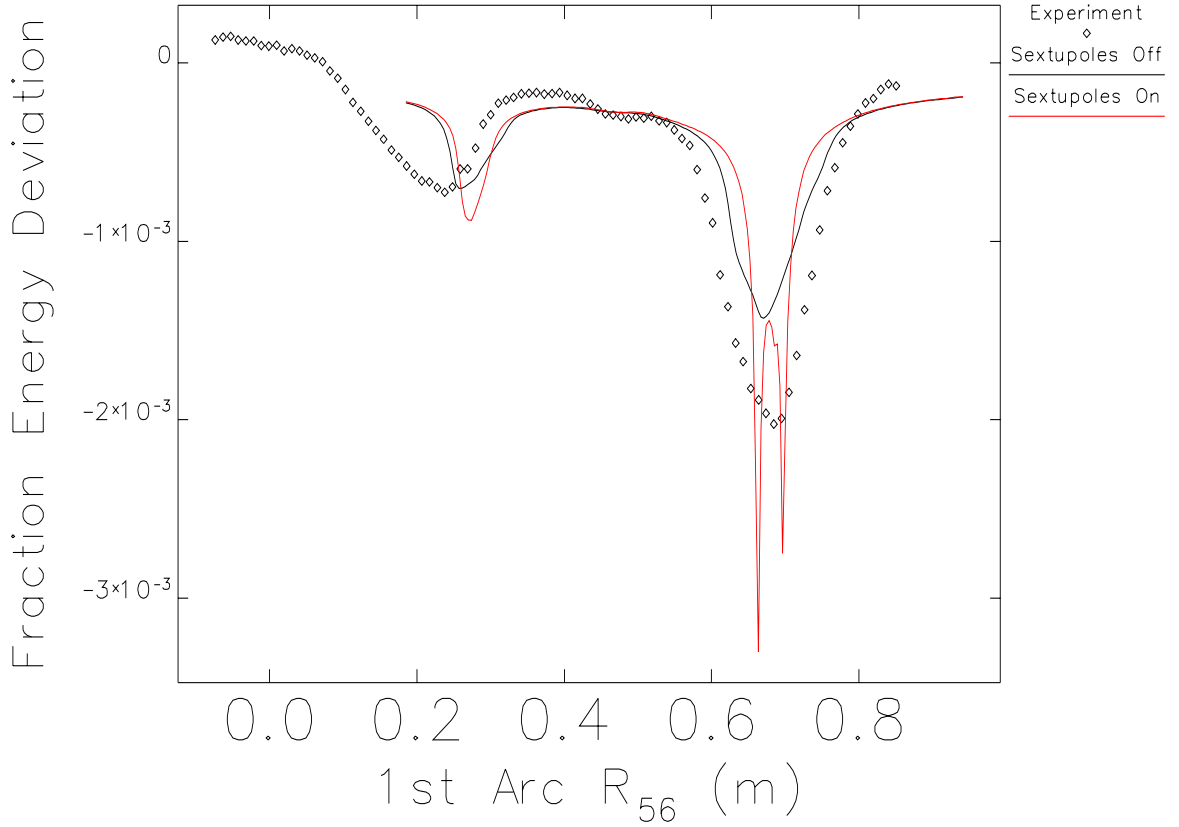


FIGURE 4.7. Fractional energy deviation of the beam as a function of the first arc momentum compaction  $R_{56}^{A1}$  for acceleration on the falling side of the rf. The experimental data is shown with the diamond symbols. The simulation is shown with sextupoles off in black and the sextupoles on in red.

were scanned over a much larger range of values that allowed for full compression to be observed after A1 in addition to downstream of BC1 and BC2.

Shown in Fig. 4.7 is the experimental data overlaid with simulated results. On the left-hand side the compression point at the end of A1 can be seen for  $R_{56}^{A1} = 0.2$  m. Because of the negative chirp the arc must now provide large positive momentum compaction to over-rotate the bunch if compression is to be achieved in the chicanes. Thus, at around  $R_{56}^{A1} = 0.7$  m we see the compression point for BC1 in the experimental data ( $R_{56}^{BC1} = 0.52$ ).

For this operating condition the sextupoles in A1 were not correctly set and it is not possible to resolve the compression point for BC2. This is also confirmed in the simulation, however, with the sextupoles on, in simulation, the two dips are able to be resolved.

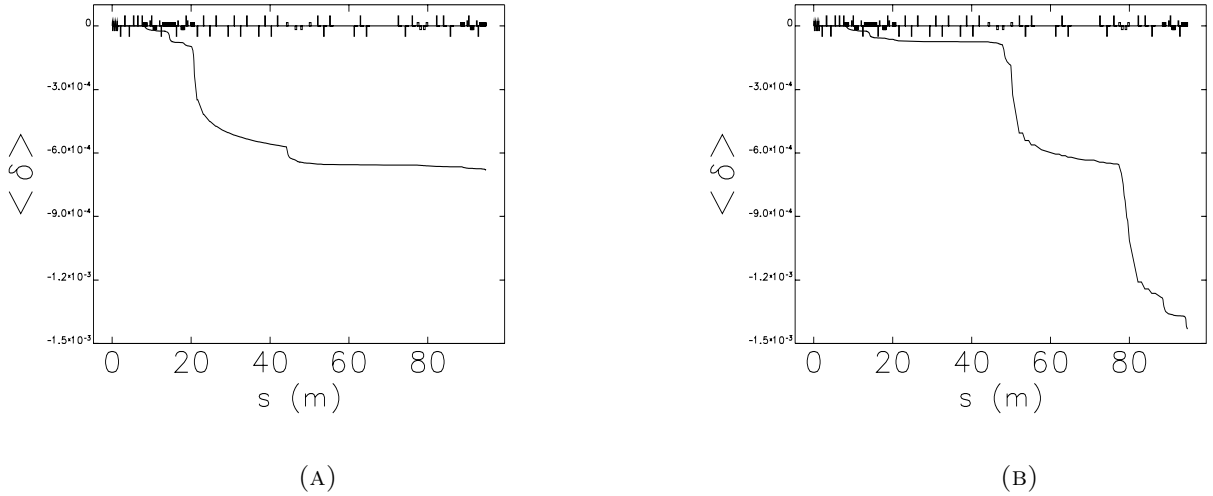


FIGURE 4.8. Fractional energy deviation as a function of position along the beamline. In (A) the result for full compression at the end of the first arc is shown. In (B) full compression is achieved at the end of the first chicane.

It is interesting to examine why there is much less observed energy loss for arc compression as opposed to chicane compression. We see from simulation that this result arises not from a difference in the compressed bunch length, but from the differing downstream features in each case. The fully compressed bunch length at the end of A1, without use of sextupole correction, is  $\sigma_t^{A1} = 415$  fs and at the end of BC1  $\sigma_t^{BC1} = 428$  fs. So it is clear that the bunch length after the arc is in fact slightly shorter than that at the end of the chicane, but this does not fully account for the difference. To resolve this discrepancy we examine the energy loss along the beamline for each case. When the bunch becomes fully compressed after the arc (4.8(A)), it will enter the BC1 chicane, which has a much larger momentum compaction strength. The bunch will grow by a factor of 4 within the first dipole alone. This may be contrasted with the case of compression after BC1, in Fig. 4.8(B) where the bunch

decompresses only slightly within BC2 due to the weaker momentum compaction. Here the bunch length will only double as it passes through the entire chicane. Due to the  $\sigma_t^{-\frac{4}{3}}$  scaling of CSR power, the bunch will only give up significant energy in the first dipole of BC1 due to the rapid decompression, while in BC2 the bunch may continue to emit significant CSR through all four dipoles.

4.5.3. SEXTUPOLE LINEARIZATION. As seen in both experiment and simulation the sextupoles play a large role in the CSR energy loss experienced by the electron beam. As has previously been mentioned, it can be seen that when the sextupoles are used to provide linearization of the longitudinal phase space there can be a large enhancement to CSR emission. It is also seen that the sextupoles allow for the observation of a compression point in the BC2 chicane. The enhancement to CSR obviously arises from the decrease in bunch length that comes with linearization (as was discussed in Section. 3.3.5). The bunch length with and without second-order correction may be calculated from the respective equations.

$$(46) \quad \sigma_f = \sqrt{(\sigma_0 (1 + R_{56}h))^2 + (R_{56}\sigma_\delta)^2}$$

$$(47) \quad \sigma_f = \sqrt{((1 + R_{56}h)\sigma_0 + (R_{56}k + T_{566}h^2)\sigma_0^2)^2 + (R_{56}\sigma_\delta)^2}$$

Using Eqs. 46 and 47 we may calculate the compressed bunch length without and with the second-order correction. These give a result of  $\sigma_t^{\text{BC1}} = 461$  fs without correction. With the sextupoles used to provide the second-order compression the bunch length is reduced to  $\sigma_t^{\text{BC1}} = 114$  fs. These values compare well to the simulation with respective bunch lengths of  $\sigma_t^{\text{BC1}} = 428$  fs and  $\sigma_t^{\text{BC1}} = 121$  fs. It was previously shown that the bunch length can be

minimized through cancellation of the  $z(\delta)$  terms in the longitudinal transfer function. The condition that must be fulfilled for the cancellation of the second-order term is given by

$$(48) \quad R_{65}^2 T_{566} + R_{56} T_{655} = 0$$

Under normal operating conditions it is desirable to minimize the bunch length at the entrance to the undulator. Therefore, the sextupoles must be configured such as to remove any longitudinal phase space curvature immediately following the BC1 chicane. The only contributions to the  $R_{65}$  and  $T_{655}$  terms will come from the linac. For the  $R_{56}$  term we must account for the momentum compaction of A1 and BC1. Likewise, there will also be a fixed contribution to  $T_{566}$  from BC1. This leaves just the free parameter of  $T_{566}^{A1}$  which can be adjusted to fulfill Eq. 48. This is accomplished with a simplex optimization routine built into `elegant` to adjust the strengths of the sextupoles in A1. With the condition that the strengths be mirrored across the arc, that is  $MSSF2F06 = MSF2F10$  and  $MSF2F07 = MSF2F09$ . Because the sextupoles were not adjusted in each step in the experiment, to account for the change in  $R_{56}^{A1}$ , we optimize only to a single setting, that achieves maximum compression in the drift after BC1.

The impact of the sextupoles on the longitudinal phase space immediately before the BC1 chicane can be seen in Fig. 4.9. The difference between the non-linearized and linearized bunch at the exit of BC1 is then shown in Fig. 4.10. From Fig. 4.9 it can be seen how slight the curvature and necessary correction are. This can be contrasted to the result downstream of BC1 in Fig. 4.10(B) showing how extreme the curvature can become if not corrected. This arises mainly from the non-linear terms of the chicane amplifying the curvature induced by the rf field. It can also be seen, with the sextupole correction enacted, there now exists a

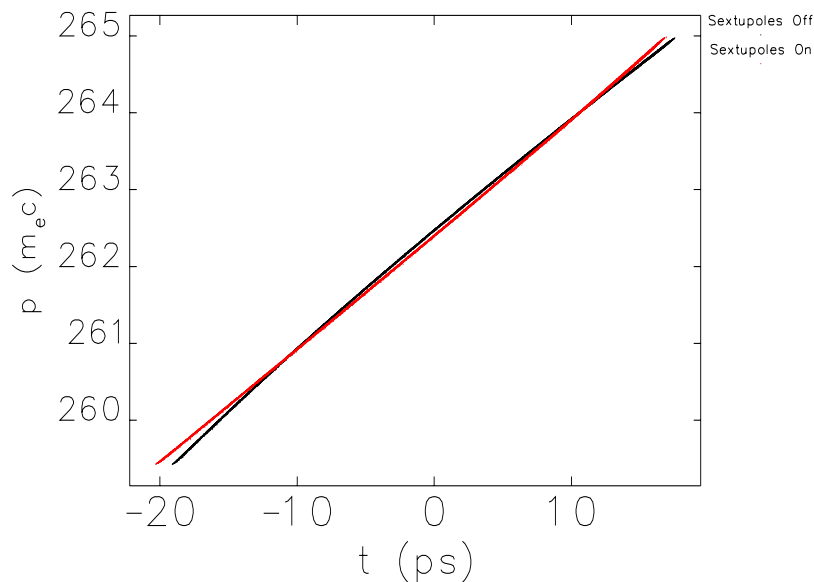
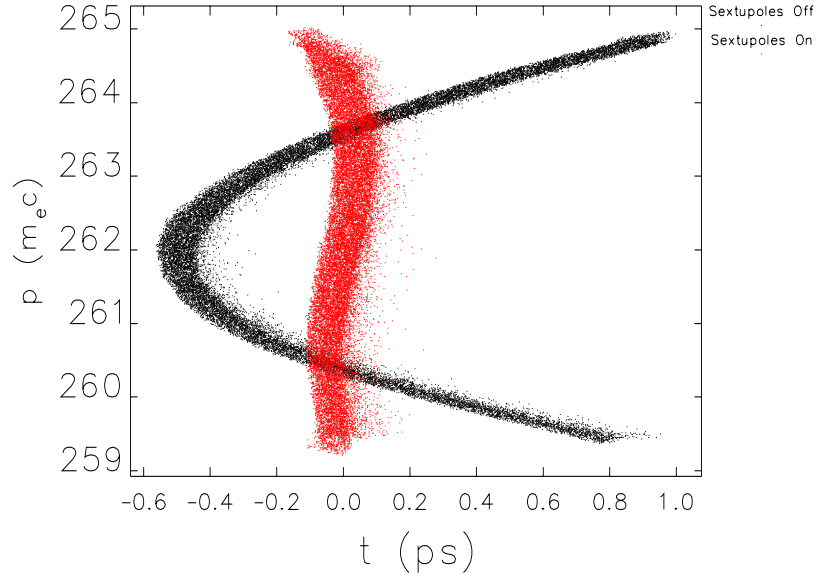


FIGURE 4.9. Comparison of a bunch with sextupoles off (black) and on (red). The longitudinal phase space immediately before the BC1 chicane is shown.

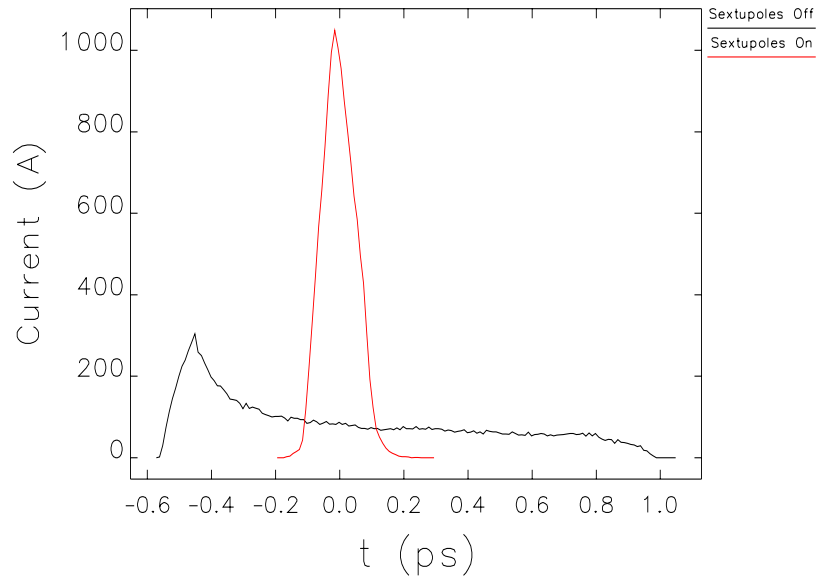
third-order distortion, a  $U_{5666}$  term, that presents itself. Correcting for this would require the use of octupole magnets which are not in place in the beamline except for in the A2 arc region.

It is interesting to examine how the energy loss along the beamline varies with the use of second-order correction and how this, in turn, interacts with the momentum compaction setting of the machine. In the condition that achieves maximum compression after BC1 it can be seen (Fig. 4.11) that the locations of energy loss for the two cases differs considerably. The corrected case shows that 85% of the energy is lost between BC1 and BC2, in contrast to the uncorrected case where the energy loss is split between BC1 and BC2 (45% and 41% respectively).

This result may seem somewhat surprising, but it is more easily understood by examining how the longitudinal phase space looks in-between BC1 and BC2. In the case where the



(A)



(B)

FIGURE 4.10. Comparison of a bunch with sextupoles off (black) and on (red). The longitudinal phase space immediately after BC1 is shown in (A), and (B) is the current distribution (histogram of (A)) at the end of BC1.

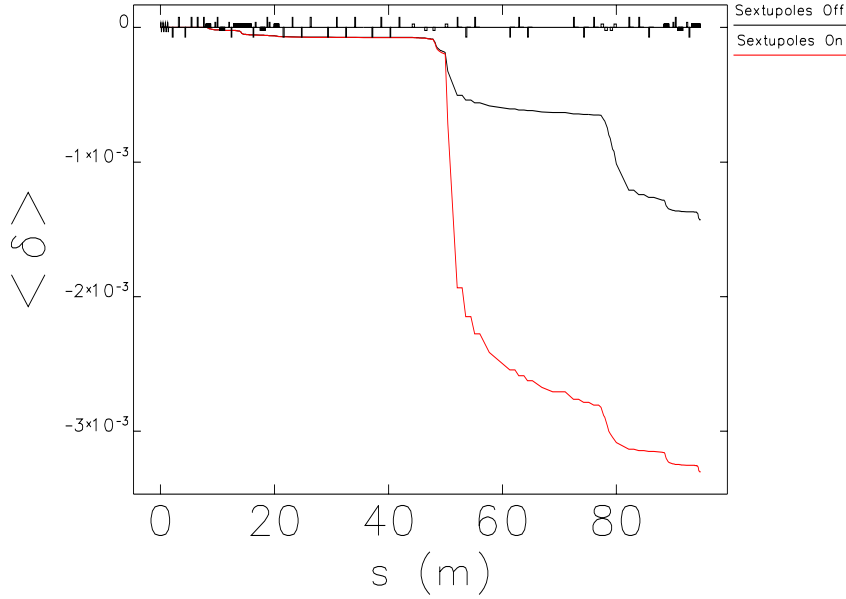
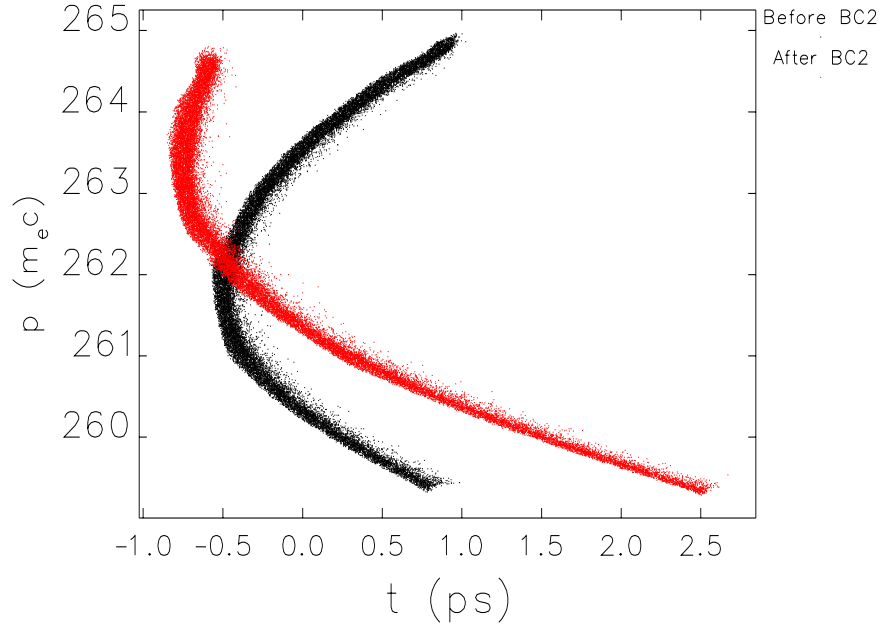


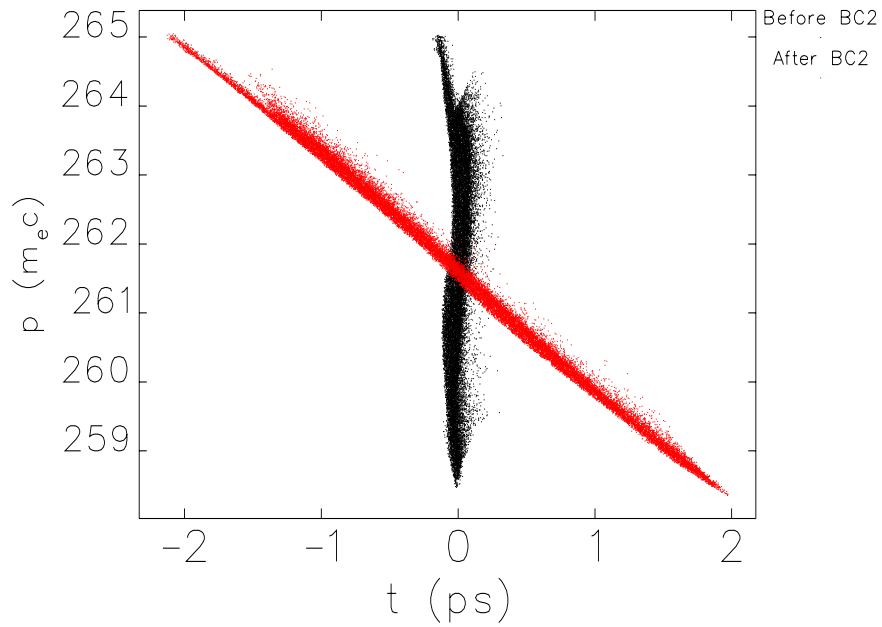
FIGURE 4.11. Energy loss as a function of position along the beamline at maximum compression after BC1 for sextupoles turned off (black) and on (red).

sextupoles remain off, as in Fig. 4.12(A), it can now be seen that because of the non-linearity the linear chirp will, of course, vary along the bunch. Because of this there exists a small region that will further compress in BC2. Leading to the observed split in energy loss between the chicanes. However, when the non-linearity is corrected the sense of linear chirp remains intact along the entire bunch. Indeed, for the fully compressed bunch we see that it is fully upright in phase space. Thus the entire bunch continues to rotate in the same fashion, and we immediately decompress within BC2, leading to the CSR emission greatly decreasing.

This mechanism, in fact, also provides the solution to one of the primary questions that arises when looking at the experiment in the rising-rf versus the falling-rf data. That is the appearance of an extra dip resolves in Fig. 4.6 but does not appear in Fig. 4.7. As surmised before, this second dip corresponds to a the bunch fully compressing after BC2.



(A)



(B)

FIGURE 4.12. The longitudinal phase space at the entrance (black) and exit (red) of the BC2 chicane. Shown in (A) is the phase space with the sextupoles turned off and in (B) with the sextupoles configured to provide linearization.

However, we can now see why it is necessary that the sextupoles be correctly configured for this to occur. Without the sextupoles, only a small fraction of the bunch will be compressed within BC2. While, with the sextupoles set up correctly to linearize, the entire bunch will be able to compress when the sense of chirp after BC1 is correct. Linearizing the bunch is also useful in reducing intense CSR from the high particle density gradient that occurs under nonlinear compression. As shown by Li [44] a bunch with the sharp current spike at the head, indicative of nonlinear compression will produce a much stronger CSR wake as compared to a Gaussian distribution even when the computed rms lengths are the same for both. While the entire bunch energy loss may not be as large the impact on other bunch properties can be significant. What will also be seen in the next section is that the sextupoles not only have an impact on CSR intensity, but will have a large role to play in how the CSR wake interacts with the bunch and influences the energy spectrum.

4.5.4. ENERGY SPECTRUM MEASUREMENT. During the measurements on the falling side of the rf a synchrotron light monitor (SLM) was also being used to monitor the energy spectrum at the center of the  $180^\circ$  bend in A2. This measurement shows how energy is being redistributed through the bunch due to the CSR and LSC forces.

In Fig. 4.13 there is the distinctive formation of a 'spike' and 'depletion region' in the energy spectrum. These structures are then seen to move, in a regular fashion, in position along the spectrum. This occurs both when there is full compression at the end of BC1 as well as at the end of A1. This movement of the 'spike' from the high to the low side of the energy spectrum proceeds as the bunch goes from under-compression through critical compression and on to over-compression. Such an effect has been observed in measurements at other facilities and even before during an earlier iteration of the JLab FEL [38][26][45]. It has been well understood that such fragmentation (also sometimes called filamentation)

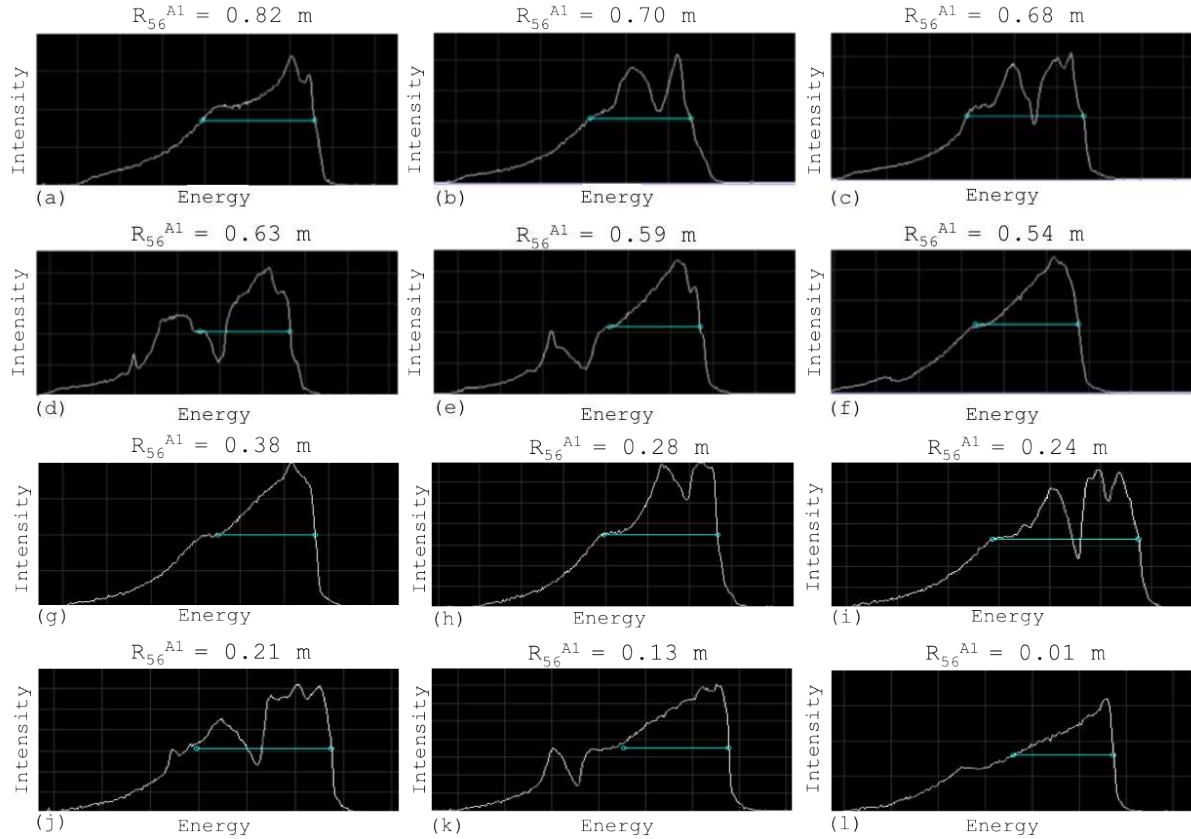


FIGURE 4.13. Measurements of the energy spectrum collected in the second Bates arc (A2). The vertical axis is the population (arb. units) and the horizontal axis is the energy (arb. units). As the compression is changed a distinct spike and depletion region form and shift along the spectrum, shown from (a) to (f) for the BC1 compression point and from (g) to (l) for the A1 compression point.

arises from the action of CSR and LSC forces on the beam. While, such effects have been previously observed, there has not been a careful study conducted of the development of fragmentation or what sensitivity it shows to changes in compression parameters. From the data collected during this experiment we can actually perform such studies and draw several significant conclusions about the formation of the fragmentation and about how it may be reduced.

4.5.4.1. *Development of the Spike.* As seen in the measurement the movement of the spike and trough move in a systematic fashion as the compression point in the machine is

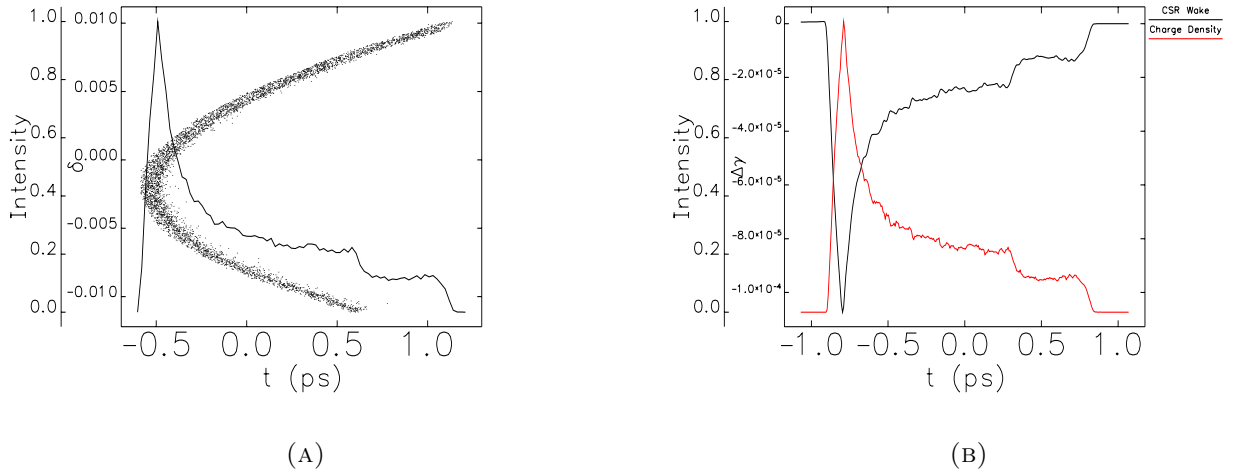


FIGURE 4.14. (A) The longitudinal phase space of a compressed bunch after BC1 is shown overlaid with the density distribution. (B) The density distribution is shown together with the CSR wake at the end of the fourth dipole in BC1. In both plots the head of the bunch occurs at  $t < 0$ .

being varied. It is clear that we should expect this phenomenon to have its origin in the dynamics of the bunch compression. It is important to recall that during the collection of the energy spectrum the sextupoles were not configured to properly suppress the bunch curvature after compression. It is this fact that provides an answer to how this fragmentation forms. As can be seen in Fig. 4.14 after compression at the end of BC1 the bunch has a strong degree of curvature and so develops a very nonuniform charge density. This resembles a spike at the head of the bunch with a long tail extending out from it. Because this spike represents a significant fraction of the bunch charge the CSR wake will be strongly localized to this area. Because of this a correlation is now drawn between particle energy and the strongest region of energy loss, and this varies as a function of the A1  $R_{56}$  setpoint.

It is also interesting to examine how the fragmentation develops along the length of the beamline. As was previously shown, while the bulk of energy loss from CSR occurs within the final dipoles of the chicane or arc there is still a non-negligible loss of energy in the drift following the final dipole. This is due to the coasting beam and CSR wake

continuing to propagate together and exchange energy. If we look, then, at how the energy spectrum develops under the influence of CSR we see an interesting thing. The fragmentation is almost non-existent when looking at the energy spectrum immediately after the final dipole of BC1, as noted by the black line in Fig. 4.15. Instead, when we look at the bunch again at the entrance to BC2 (the red line in Fig. 4.15) there is now a significant degree of fragmentation that has formed. The wake in the drift will be much weaker than that in the dipole, and the beam is no longer able to regenerate the wakefield and it will

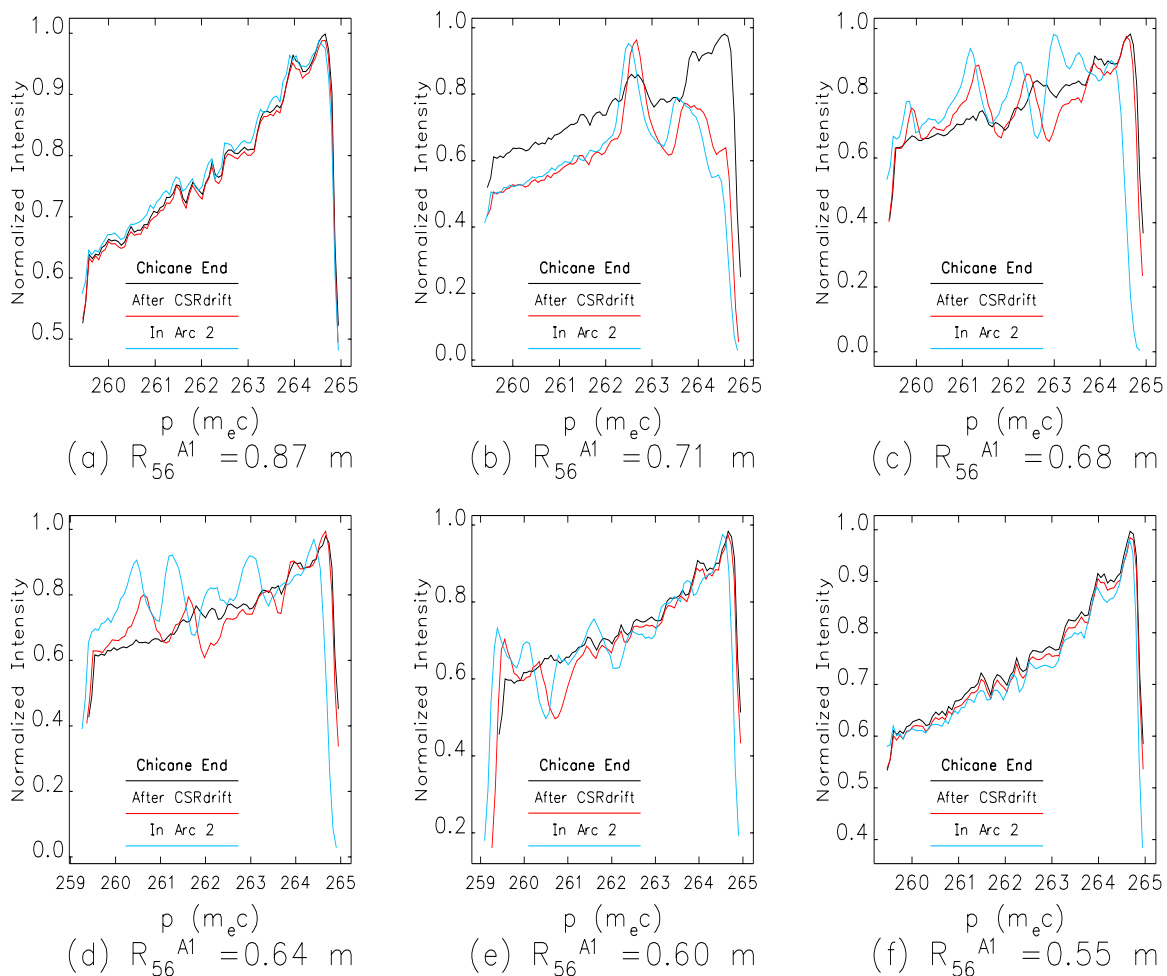


FIGURE 4.15. Simulation of the energy spectrum as the beam progresses in (a)-(f) from under-compressed to critically compressed to over-compressed. In each plot the energy spectrum is examined at the end of BC1 (black), the entrance to BC2 (red), and the middle of A2 (blue).

dissipate ultimately. Nevertheless, the bunch is also no longer rotating in phase space, thus the distribution the wakefield is acting on is stationary and there is a long period for the interaction to occur. So even though the total energy loss is much less after the dipoles, from the perspective of the energy spectrum what energy is lost and its impact on the bunch will be much more severe. This fragmentation effect does not grow very much past the entrance of BC2 as seen from the final energy spectrum at the measurement position in A2, shown by the blue line in Fig. 4.15 due to the decompression of the bunch in BC2.

4.5.4.2. *Movement of the Spike.* We make the assumption that the bunch entering the chicane is linearly chirped by some amount  $h$  where  $\delta = hz$ , therefore the transfer function through the chicane, to second order will be:

$$(49) \quad z_f(\delta) = z_0 + R_{56}\delta + T_{566}\delta.$$

Substituting in  $\delta$  for the initial position  $z_0$

$$(50) \quad \delta(h, R_{56}, T_{566}; z_f) = -\frac{(1 + hR_{56})}{2hT_{566}} \pm \frac{1}{2hT_{566}} \sqrt{(1 + hR_{56})^2 + \frac{4T_{566}}{h^2} z_f}.$$

It can be seen from Eq. 50 that the inflection point of the parabola, formed by the bunch, will shift in energy based upon  $-(1 + hR_{56})/2hT_{566}$ . This term depends upon the initial chirp which is held constant since the linac phase is not changed and due to the  $R_{56}$  and  $T_{566}$  settings of the lattice. Because these terms are changing during the experiment the position of the inflection point, where the charge density spike is located, will shift up or down in energy. As this shift occurs, there will be a corresponding shift in the region

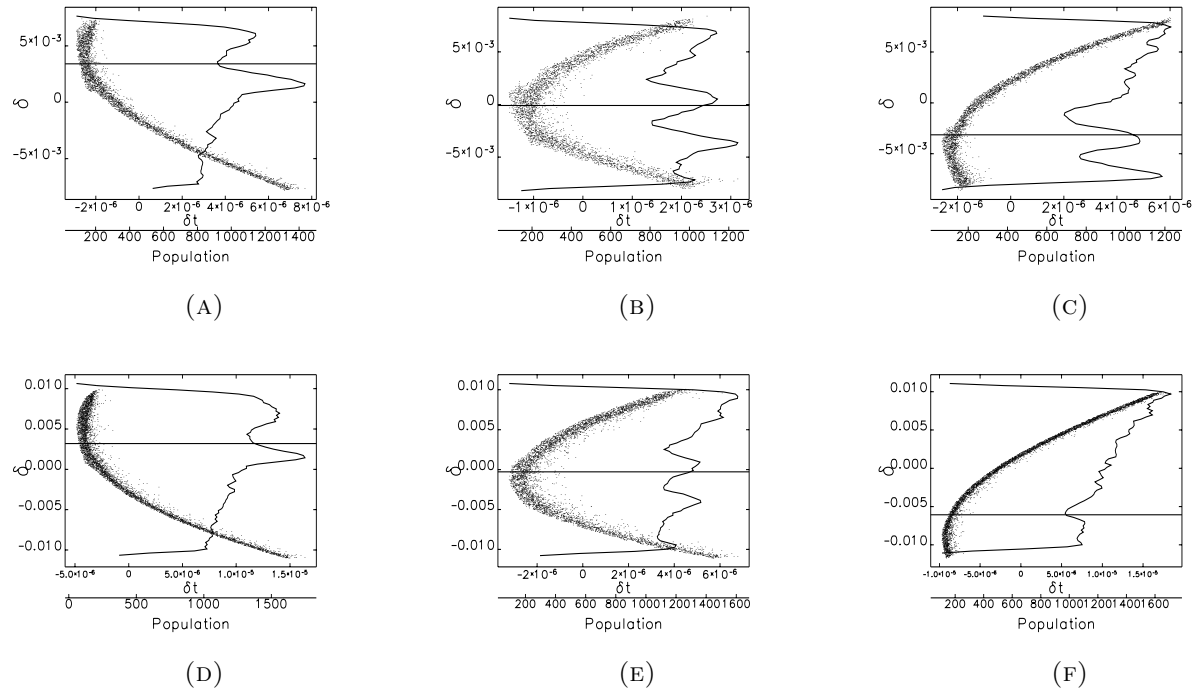


FIGURE 4.16. The longitudinal phase space overlaid with the energy spectrum at the beginning of BC2 (a)-(c) and the beginning of BC1 (d)-(f). The horizontal line is the predicted point from Eq. 50.

of the energy spectrum affected by the CSR wake. It is for this reason that we see, in the experiment, this progression from high energy to low.

This also agrees well with simulation. When the inflection point from Eq. 50 is plotted against the longitudinal phase space and energy spectrum (Fig. 4.16) there is a good match to the development of the bunch shape in the phase space as well as the main region of fragmentation which is centered around the predicted point.

4.5.4.3. *Impact of the Sextupoles.* Up to this point we have only considered the conditions under which the experiment was performed. That is, with sextupoles not tuned correctly to properly linearize bunch compression. We now look at what would happen in the case where the sextupoles are properly set to fulfill this condition. If we consider what will happen to the bunch in this case, we know that the charge density will be restored to a more uniform, Gaussian profile and that the bunch length will be much shorter at maximum compression. While the CSR wake will still be non-uniform along the bunch length the effect should be expected to be less severe. Because the  $z$ - $\delta$  correlation will remain mostly linear there will no longer be a significant correlation between the point of maximum field from the CSR wake and average particle energy. This would lead to the conclusion that with proper use of the sextupoles a condition can be achieved where the energy spectrum remains mostly undisturbed, albeit the overall energy loss at maximum compression would be larger.

A comparison between the energy spectra contrasting the result for correctly tuned sextupoles against the incorrectly tuned is shown in Fig. 4.17. Here the bunch is slightly over-compressed. From this, it can be seen that correctly removing the non-linear compression can have the added advantage of also removing the energy fragmentation. Of course it is already ideal to linearize the compression to reduce bunch length; however, this analysis

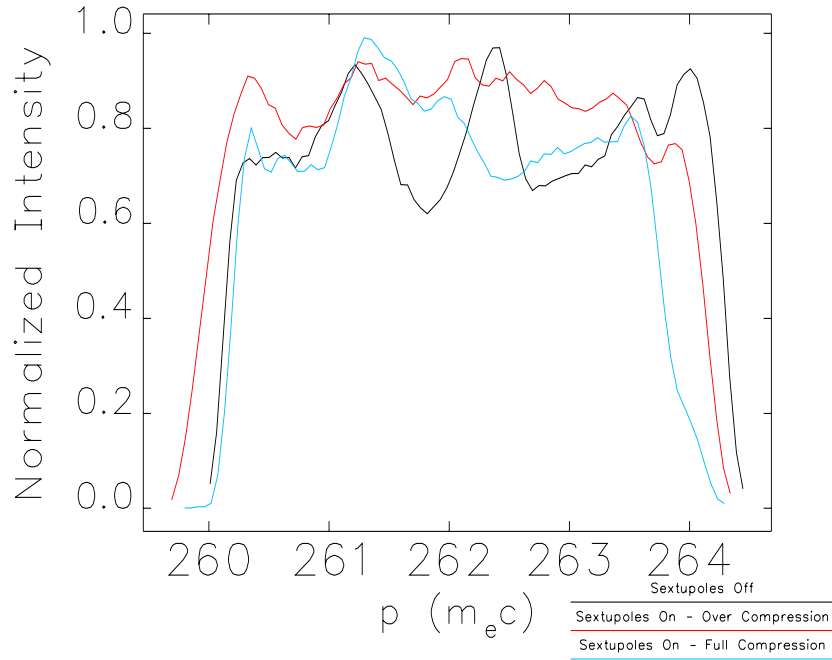


FIGURE 4.17. Energy spectrum before BC2 for maximum compression between BC1 and BC2. The spectrum with sextupoles off is shown in black. In red is the spectrum for full compression and sextupoles on. In blue the sextupoles are on but the bunch is slightly over-compressed. The vertical axis has been normalized.

demonstrates that for very short bunches it is necessary to correctly control curvature for reasons beyond bunch length.

To make a more systematic study of the impact of the sextupoles on fragmentation we also examine how variation in sextupole strength changes the energy spectrum again in simulation in *elegant*. Unfortunately, experimental time on the JLab FEL was extremely limited, and following our experiment the machine went into shutdown, removing any opportunity for further experiments. To perform this simulation we step the sextupole strength from 0 to 300% of the nominal setting. The quadrupoles were set in all cases so as to provide maximum compression at the end of BC1.

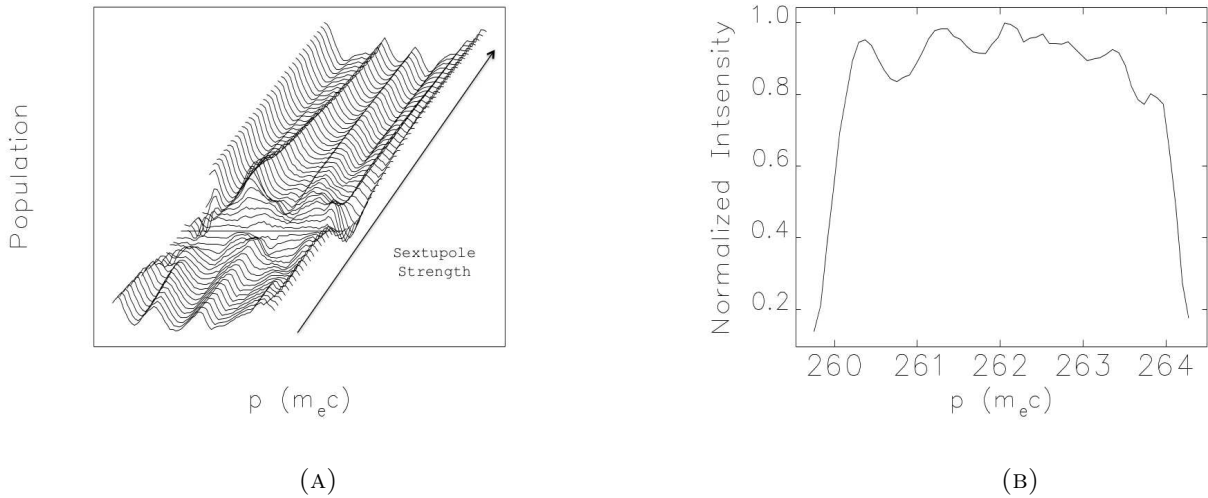


FIGURE 4.18. (A) Mountain range plot of the energy spectrum difference from the baseline taken when the sextupoles are correctly set. The sextupole strength is scaled from 0 to 300% of the correct setpoint for linearizing the bunch. At the bottom left the sextupoles are completely off while at the top right of the plot the sextupole strength has reach 300% of the correct setpoint. (B) Baseline momentum distribution when sextupoles are set to nominal strength.

The energy spectrum at 100% is taken as the baseline distribution (Fig. 4.18(B)), and we subtract it out from the spectrum at each step. We also clip 10% of the bins on either end to remove the impact of any edge effects. The resulting normalized spectra can be seen in Fig. 4.18(A). As the sextupole strength is varied the fragmentation forms and then dies off near the optimal sextupole set strength; however, once the sextupole strength overshoots this point the fragmentation tends to worsen significantly again. A quantitative description of this same data is shown in Fig. 4.19 which shows the standard deviation (A) and maximum deviation (B) of the spectra from the baseline. Both the standard deviation and maximum deviation tend to grow together, showing the formation of several large spikes. This is to be expected as the CSR impact is localized in position and there still exists a second-order correlation between energy and position after BC1 when the sextupole correction is not used or is set improperly.

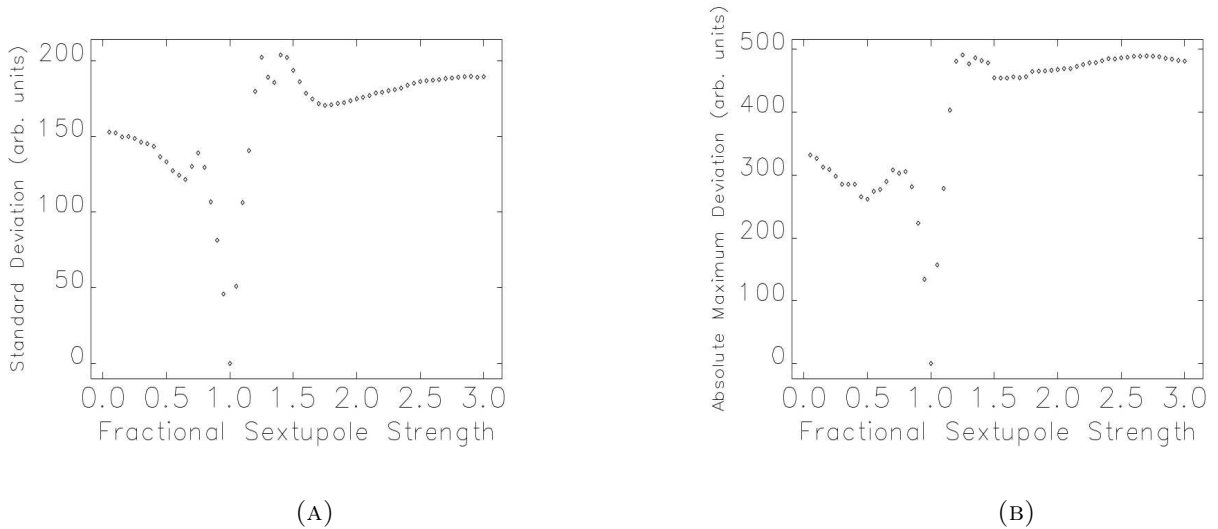


FIGURE 4.19. The standard deviation (A) and the maximum deviation (B) of the energy spectrum minus the baseline as the sextupoles are scaled from 0 to 300% of the correct sextupole setpoint for linearizing a bunch at full compression after BC1. For both calculations the edges of the distribution are excluded.

4.5.5. LSC SIMULATIONS. While transverse space charge forces are generally of lesser importance in the ultra-relativistic regime there is still potential for longitudinal space charge (LSC) forces to play a large role in beam physics for FEL drivers. In particular, when the bunch is highly compressed the large concentration of charge can lead to a large, integrated LSC force over a long transport section. As the beam coasts in the transport line, downstream of compression, the LSC force will act on it causing energy modulation along the beam based, in general, upon its 3-D distribution. However, as previously discussed we can employ an approximation based upon a 1-D model of the beam to calculate the LSC impact. The free-space 1-D LSC impedance per unit length [41] is then given in terms of the wavenumber  $k = 2\pi/\lambda$

$$(51) \quad Z_{LSC}(k) = \frac{iZ_0}{\pi k r_b^2} \left[ 1 - \frac{k r_b}{\gamma} K_1 \left( \frac{k r_b}{\gamma} \right) \right],$$

where  $Z_0$  is the impedance of free-space,  $r_b$  is the bunch radius, and  $K_1$  is the modified Bessel function of the first kind. It is important to note that in `elegant` this force is applied in the supported beamline elements using a kick-drift-kick model. To ensure that this model is accurate the space-charge oscillation period of the beam must be large in comparison to the drift length. The space-charge oscillation period may be calculated [46] from

$$(52) \quad k_{SC} = \left[ 4\pi k_0 \frac{I_0}{\gamma^3 I_A} \frac{|Z_{LSC}(k_0)|}{Z_0} \right]^{\frac{1}{2}}$$

Where  $I_0$  is the peak current of the bunch and  $I_A \approx 17\text{kA}$  is the Alfvén current for electrons. In the drift region between BC1 and BC2 the peak current is around 400A at peak compression, the energy is  $E = 135 \text{ MeV} = \gamma mc_0^2$ , and  $r_b \approx 0.5 \text{ mm}$  on average. A plot of the space charge oscillation period over a range of modulation wavelengths is shown in Fig. 4.20. From this we can see that even for extremely short wavelengths  $\lambda \approx 1 \mu\text{m}$  the period is much longer than the longest drift lengths  $L \approx 20 \text{ m}$ . Thus LSC forces will only result in the buildup of energy modulation within the beam but longitudinal positions of the particles will remain frozen along the drift.

4.5.5.1. *Simulation Setup.* As with the CSR simulation setup, close attention is paid to make sure that the simulation parameters chosen will produce convergent results and will not be overrun with numerical noise. Because the LSC force is calculated using the 1-D impedance, it is necessary to bin the longitudinal distribution so that it may be Fourier transformed. Noise from this process must be carefully controlled or it may artificially induce microbunching in the simulation [47]. Fortunately, we are primarily concerned with effects on a much larger scale than typical microbunching wavelengths, and the process we wish to examine does not start up from noise. Rather, energy fragmentation will lead to very

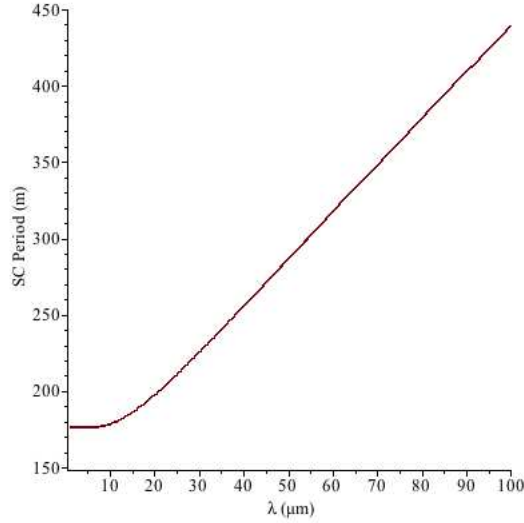


FIGURE 4.20. The space charge oscillation period as a function modulation wavelength (shown for typical beam parameters downstream of BC1).

long-wavelength density modulation of the bunch after passage through BC2 or in A2. To control high frequency noise in the LSC calculation `elegant` uses a low-pass filter of the form

$$(53) \quad F(f) = \begin{cases} 1, & f < c_1 f_N \\ \frac{f - c_2 f_N}{(c_1 - c_2) f_N}, & c_1 f_N \leq f \leq c_2 f_N \\ 0, & f > c_2 f_N \end{cases}$$

where  $f_N$  is the Nyquist frequency and  $0 < c_1 < c_2 < 1$ . Using 200 bins with  $c_1 = 0.25$  and  $c_2 = 0.3$  will suppress wavelengths below  $36 \mu\text{m}$ . Using this high bound for noise suppression allows for use of fewer particles than might otherwise be required while still suppressing the occurrence of artificially induced shot-noise microbunching [48]. An example is shown in Fig. 4.21 of the charge density distribution at the end of BC2 for a bunch near full compression and with sextupoles improperly set. In general, good convergence and noise reduction is

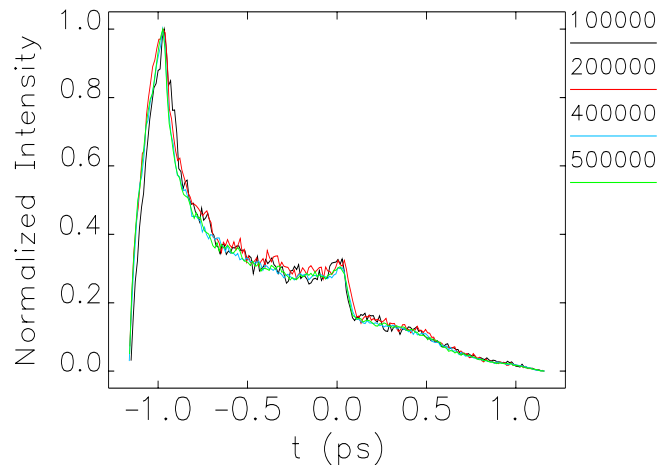


FIGURE 4.21. The longitudinal density distribution at the end of BC2 for various macroparticle counts in Elegant with LSC enabled.

seen for macroparticle counts beyond 400K so for the LSC simulations shown we will use 500K macroparticles.

4.5.5.2. *Simulation Results.* Since longitudinal space charge force is nothing more than the Coulomb force, we should expect that the inclusion of LSC now, in the simulation, should not significantly impact the results of the energy loss measurement. The bunch, in this instance, constitutes an isolated system and thus the space charge force acting within the bunch should not change the total energy. The energy loss along the beamline with LSC forces included in addition to CSR remains unchanged as shown in Fig. 4.22 when compared to simulation with only CSR enabled. There is some very slight deviation observable between the result with LSC on and off that can be seen which is due to the slight deformation of the bunch during acceleration in the linac. It will be seen, however, that energy fragmentation is further enhanced, which will lead to some density fragmentation when the bunch encounters a non-zero  $R_{56}$  region. This does not lead to much increase in CSR emission though. This is due to the fact that fragmentation always occurs when the bunch is most compressed,

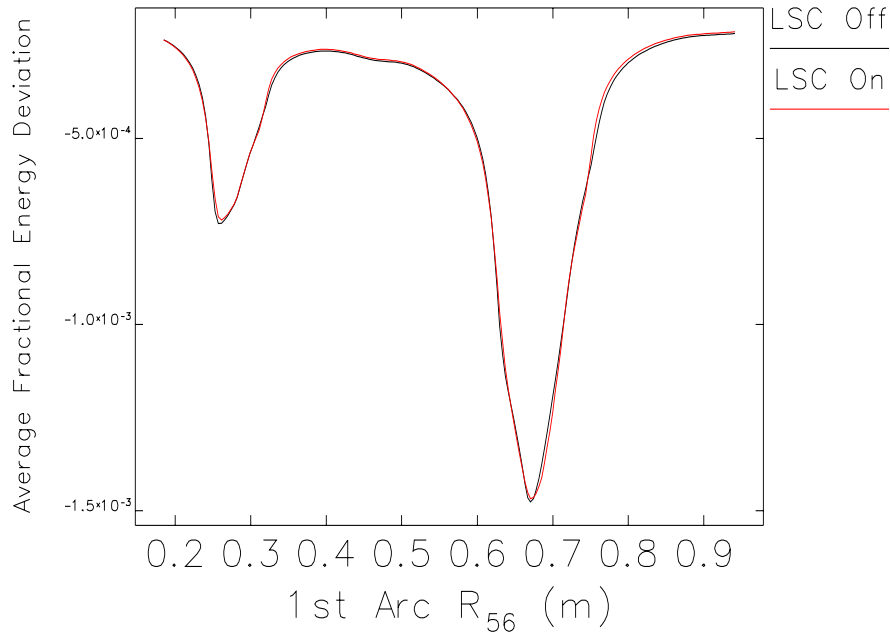


FIGURE 4.22. Simulated energy loss as a function of  $R_{56}$  setting in A1. The simulation without LSC is shown in black and with LSC is shown in red. In both cases CSR is enabled.

subsequently the bunch will decompress when additional momentum compaction is applied. Thus, even though density fragmentation may still form, the individual fragments remain quite long, on the order of picoseconds.

There is a significant enhancement in the energy fragmentation that occurs from the introduction of LSC into the simulation, however. As is suggested in Fig. 4.23 the shifts in particle energy that occur around the point of maximum field strength are equivalent or greater for LSC as compared against CSR in the beamline between BC1 and BC2. While the integrated contribution from LSC is quite significant the maximum force will be much less than that from CSR. However, the LSC force will remain almost constant over this whole distance until the bunch is decompressed in BC2. The force from CSR will quickly diminish as the radiation intensity drops off with distance due to the increasing solid angle. We can

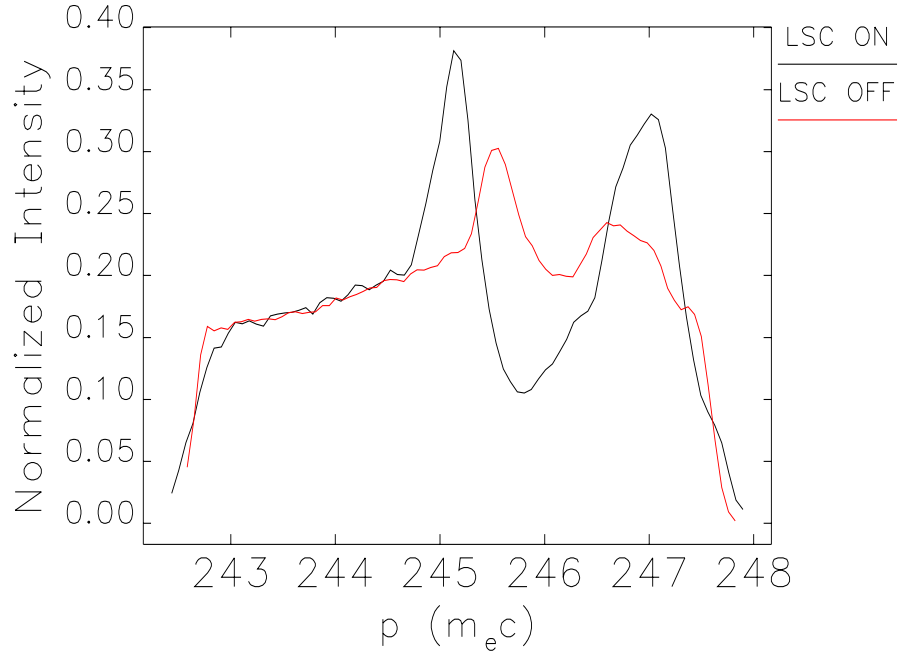


FIGURE 4.23. Energy spectrum at the center of A2 for simulations with LSC turned off (red) and on (black). CSR is enabled in both cases.

estimate the strength of CSR versus LSC to give a relative comparison of their impact.

Assuming a steady-state 1-D CSR wake and assuming a Gaussian distribution

$$(54) \quad \frac{dE_{CSR}(z)}{ds} = -\frac{2e^2 N}{3^{1/3} \sqrt{2\pi} R^{2/3} \sigma_z} \int_{-\infty}^z \frac{d}{dz'} e^{-\frac{z'^2}{2\sigma_z^2}} \frac{dz'}{(z - z')^{1/3}},$$

gives a maximum energy change of 320 keV/m at the end of the final dipole of BC1. A

simple estimate can be made of the LSC force from the equation [49]

$$(55) \quad \frac{dE_{LSC}(z)}{ds} = -\frac{2e}{\gamma^2} \frac{\partial \lambda(z)}{\partial z} \ln\left(\frac{b}{a}\right),$$

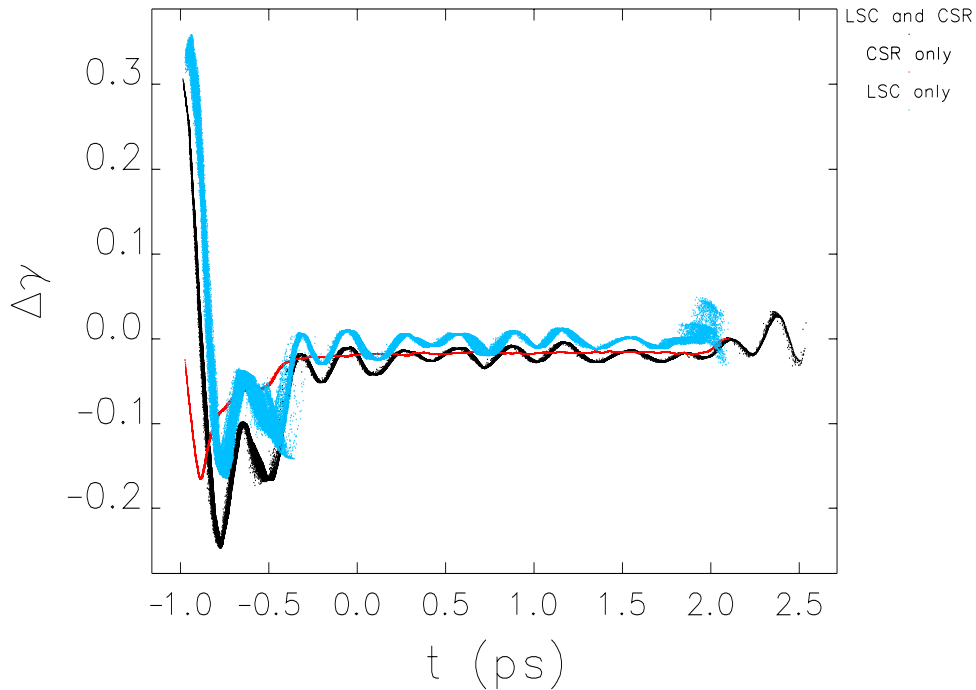
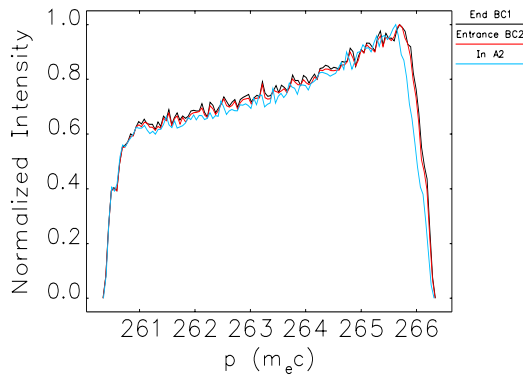


FIGURE 4.24. Comparison of total energy loss due CSR (red), LSC (blue), and both LSC and CSR (white) accumulated between BC1 and BC2 at full compression after BC1.

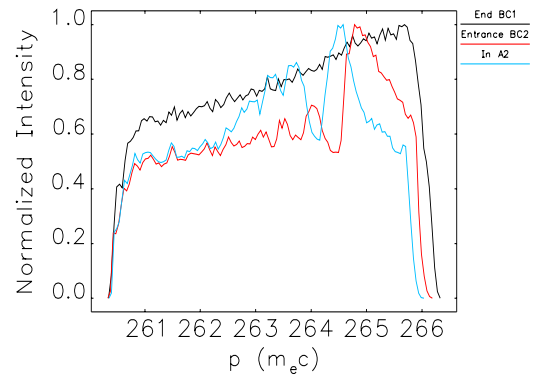
where  $b$  is the pipe radius and  $a$  is the beam radius and  $\lambda(z)$  is the linear charge density. This gives a constant change of 8 keV/m along the beamline. However, because both CSR and LSC forces are related to the derivative of the charge distribution they will have similar shaped wakefields and should contribute to energy loss and gain in roughly the same longitudinal regions. This leads to the large increase in energy fragmentation that can be seen in Fig. 4.23. The contributions from LSC and CSR may be separately quantified in `elegant` by looking at the change in energy particle by particle. The result is shown in Fig. 4.24. The LSC wake can be seen to impart fairly considerable energy gain to the head of the bunch, while the minima of the CSR and LSC wake are situated quite closely together.

It is also important to note that the LSC force contributes significantly to energy gain of particles at the head of the bunch. This energy gain will also help to increase the level of fragmentation as compared to the CSR-only result. The development of the fragmentation with both LSC and CSR enabled can be seen in Fig. 4.25. The fragmentation develops and moves along the energy distribution in much the same manner as before, though the relative depth is more consistent with that observed in the experiment in Fig. 4.13, as opposed to fragmentation with only CSR (as in Fig. 4.15). As before, fragmentation primarily develops in the distance between BC1 and BC2 (about 20 m), in BC2 the bunch will decompress causing LSC forces to be greatly reduced with the drop in peak current.

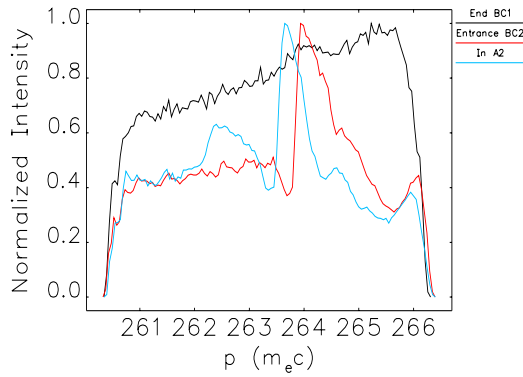
The same development is also observed along the 22-m length between A1 and BC1. Here, even with both intervening chicanes before the final observation point there is no significant further change in the energy spectrum after BC1, again due to decompression. It is particularly interesting to note in this case, though, that the  $R_{56}$  of the chicanes will cause transfer of the fragmentation from the energy spectrum into the longitudinal density profile of the beam. The density distribution corresponding to the energy spectrum in Fig. 4.26(c) is shown in Fig. 4.27. The modulation in the density that has formed is akin to microbunching, and of course, has the same basic formation mechanism. The energy fragmentation from CSR and LSC has caused lower energy electrons to shift ahead in position while higher energy electrons fall back when the bunch passes through a region with non-zero momentum compaction. The key difference from microbunching is that the density modulation does not arise stochastically. The effective modulation wavelength in this case is also an appreciable fraction of the bunch length. In the example the modulation wavelength is over 1500  $\mu\text{m}$ , much longer than the standard regime for microbunching of  $< 100 \mu\text{m}$ . Regardless, the strong fields formed after compression can still be seen to produce undesirable effects on the



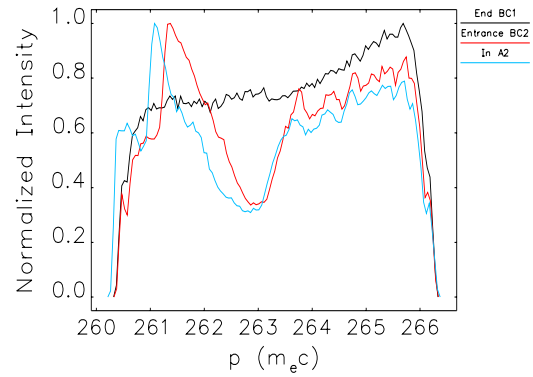
(A)



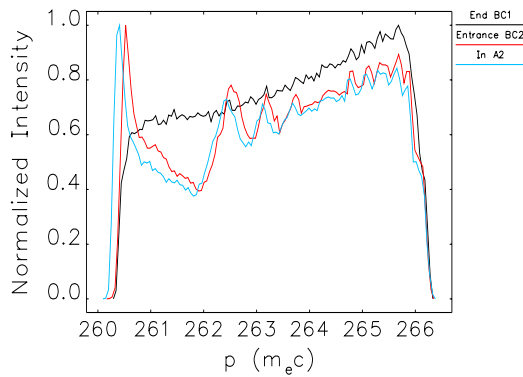
(B)



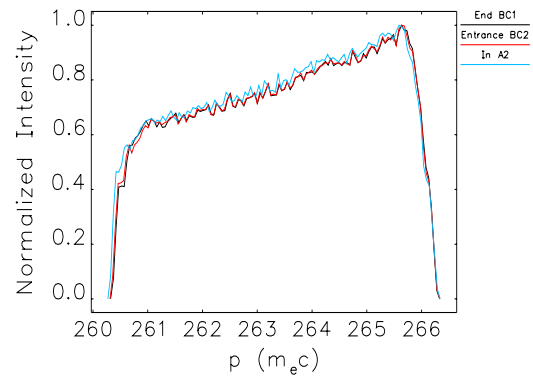
(C)



(D)



(E)



(F)

FIGURE 4.25. The energy spectrum of the bunch is shown at three positions: the exit to BC1 (black), the entrance to BC2 (red), and the middle of A1 (blue). Compression at the end of BC1 is varied from under-compressed through to over-compressed in (A)-(F).

beam and it is desirable to understand under what conditions we may minimize this strong fragmentation effect, in particular from LSC.

4.5.5.3. *Minimizing LSC Impact.* It is quite clear from both the experimental data and simulation that LSC can have a profound effect upon the longitudinal phase space of a highly compressed electron bunch. Energy fragmentation is seen to be an issue after compression and if multiple compression stages are desired in the accelerator this could possibly lead to density fragmentation [50]. To gain a better understanding of how the charge distribution impacts the magnitude of the LSC field we use Eq. 55 to calculate the induced field from LSC along the bunch. For ease of calculation we start with a Gaussian distribution in the longitudinal phase space that has an energy dependence described by  $\delta(z) = hz + kz^2$ . The distribution in the longitudinal plane  $\rho(z, \delta)$  is then

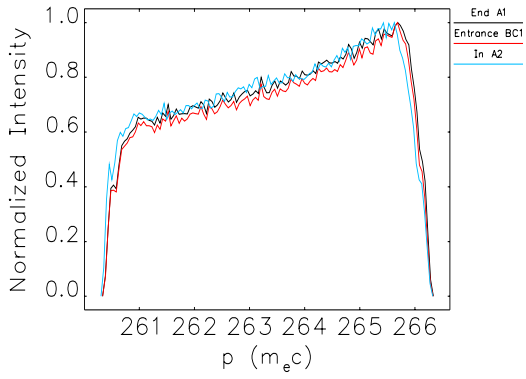
$$(56) \quad \rho_0(z, \delta) = \frac{N}{2\pi\sigma_z\sigma_\delta} e^{-\frac{z_0^2}{2\sigma_z} - \frac{(\delta_0 - hz_0 - kz_0^2)^2}{2\sigma_\delta}}$$

Up to second order and ignoring radiative effects, when the bunch compresses in some region the coordinates will be transformed to,

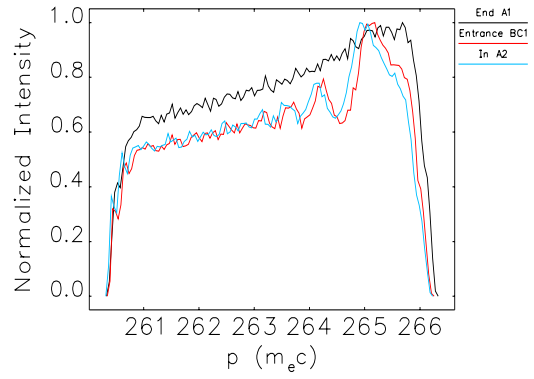
$$(57) \quad \delta_0 = \delta_f$$

$$(58) \quad z_0 = z_f - R_{56}\delta_0 - T_{566}\delta_0^2$$

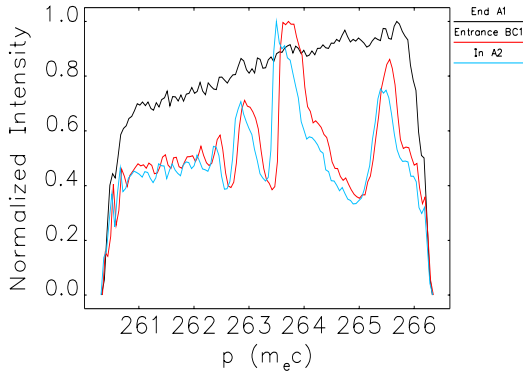
The transformed distribution will then be



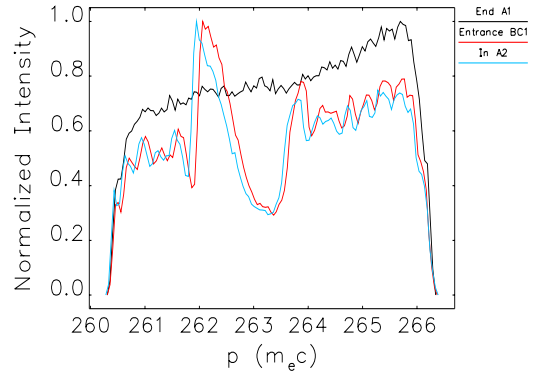
(A)



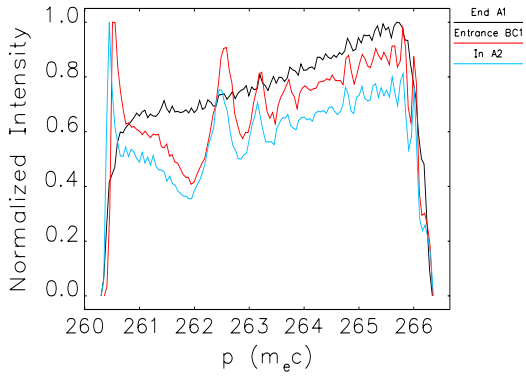
(B)



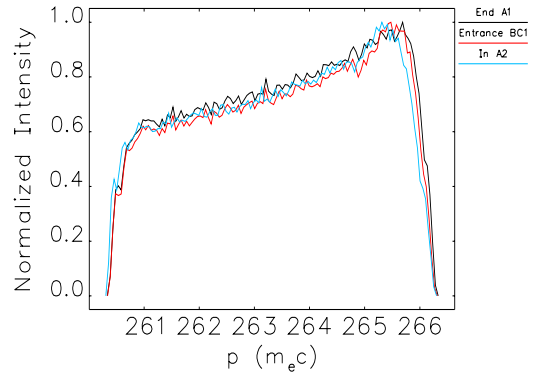
(C)



(D)



(E)



(F)

FIGURE 4.26. The energy spectrum of the bunch is shown at three positions: the exit to A1 (black), the entrance to BC1 (red), and the middle of A1 (blue). Compression at the end of BC1 is varied from under-compressed through to over-compressed in (A)-(F)

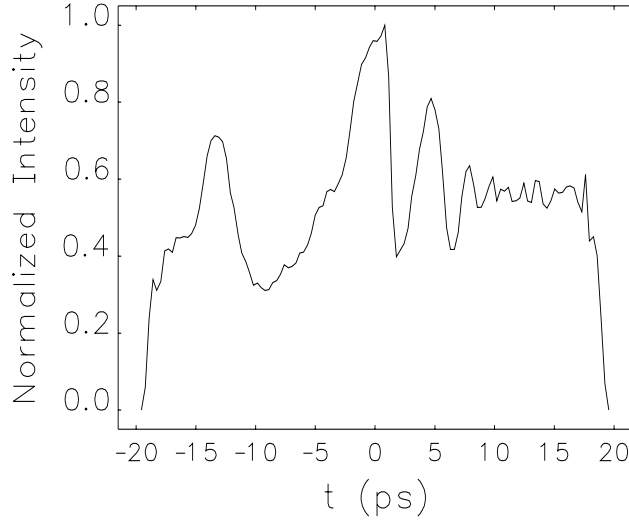


FIGURE 4.27. The longitudinal charge distribution at the entrance to A2 for a bunch compressed at the end of A1.

$$(59) \quad \rho_f(z, \delta) = \frac{N}{2\pi\sigma_z\sigma_\delta} e^{-\frac{(z_f - R_{56}\delta_f - T_{566}\delta_f^2)^2}{2\sigma_z}} e^{-\frac{(\delta_f - h(z_f - R_{56}\delta_f - T_{566}\delta_f^2) - k(z_f - R_{56}\delta_f - T_{566}\delta_f^2))^2}{2\sigma_\delta}}$$

The projected charge distribution  $\lambda(z) = \int_{-\infty}^{\infty} \rho_f(z, \delta) d\delta$  can then be used to find the corresponding LSC field. Two results are examined in Fig. 4.28 using the parameters given in Table. 4.1. In the first case the linear approximation is applied to the distribution and transport, that is  $k = 0$  and  $T_{566} = 0$ . This results in a purely Gaussian distribution both before and after compression. By contrast, the more realistic situation is examined for a bunch using typical parameters from the JLab FEL without second-order compensation via the sextupoles. After compression, the Gaussian distribution has morphed to a highly asymmetric distribution with a strong leading spike (as was seen in simulation under similar conditions). The result is that the peak LSC field grows by a factor of 20 for the nonlinear distribution as compared with the linear case.

TABLE 4.1. Parameters used to calculate bunch profile and LSC fields for linear compression, nonlinear compression, and compression with  $T_{566}$  corrected to linearize the bunch.

Type	Q [pC]	$\sigma_z$ [mm]	$\sigma_\delta$	h [ $m^{-1}$ ]	$[m^{-2}]$	$R_{566}$ [m]	$T_{566}$ [m]
Linear	135	3.2	5.00E-05	-5	0	0.21	0
Nonlinear	135	3.2	5.00E-05	-5	-450	0.21	-2.5
Corrected	135	3.2	5.00E-05	-5	-450	0.192	3.478

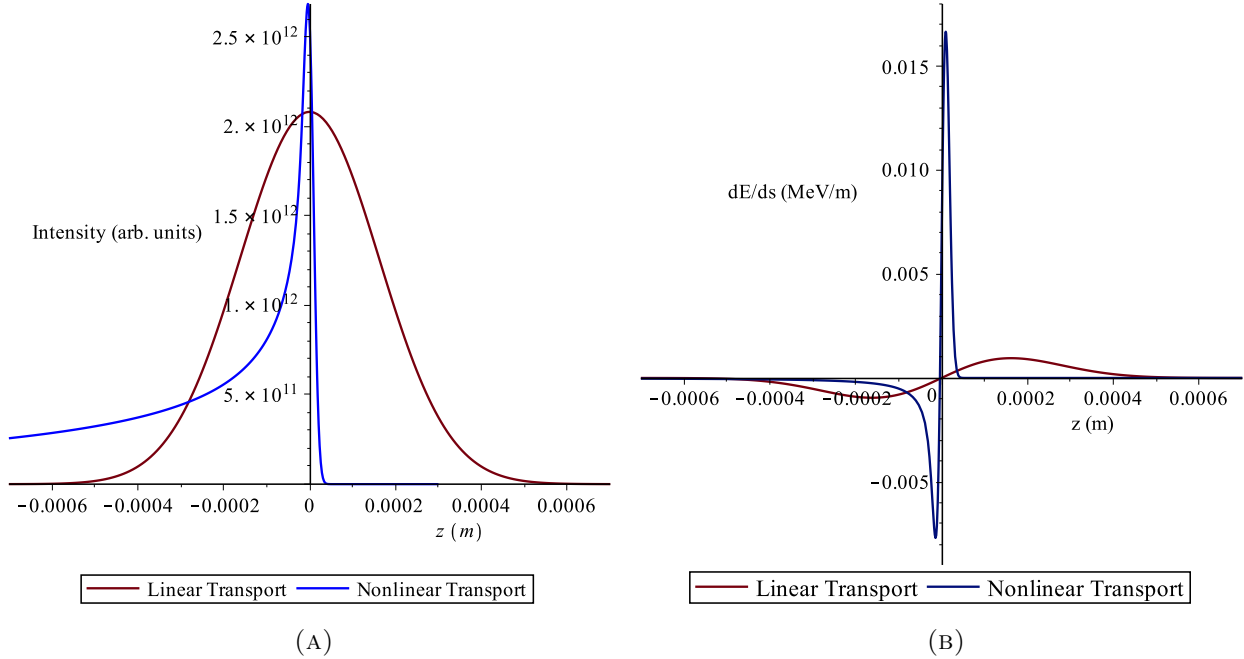


FIGURE 4.28. (A) Longitudinal density for linear transport (red) and nonlinear transport (blue) and (B) the corresponding LSC fields calculated from Eqs. 55 and 59.

The greatly increased LSC field is due to a very sharp gradient for the nonlinear bunch. To correct for this we may, as before, apply sextupoles to counter the induced curvature. By running the bunch slightly before full compression and setting  $T_{566}$  accordingly, we can create a much more gently sloped bunch after compression with comparable peak current, Fig. 4.29. Comparing the magnitude of the LSC field in Fig. 4.29 against that in Fig. 4.28 it can be seen that even though the peak current is comparable, the field has been reduced by a factor of 5. In this way, similar to that for CSR, we may reduce the impact of LSC on the longitudinal phase space, even for very high compression ratios.

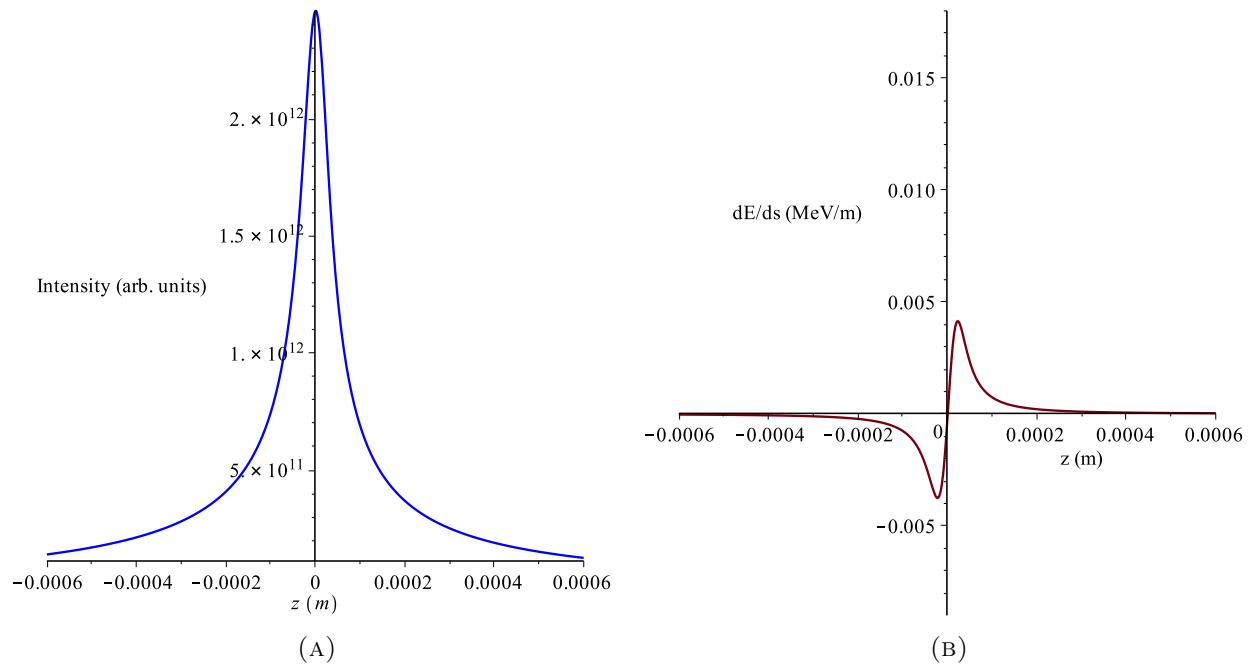


FIGURE 4.29. (A) Longitudinal density for adjusted setting of  $T_{566}$  to linearize transport (B) the corresponding LSC fields calculated from Eqs. 55 and 59.

## CHAPTER 5

### 2D CSR SIMULATIONS

While the CSR 1D-model representation provides a computationally efficient means to include CSR into beam dynamics simulations, the conditions under which this model is valid must be understood. Several studies [51–53] using a variety of codes to model CSR in 2D (bending-plane and longitudinal motion) and 3D have shown, generally, that there are small discrepancies between the 1D projected model and more accurate treatments. Unfortunately, few experiments exist demonstrating good comparison between experimental data and the 1D and 2D models. One example performed on the LCLS [28], does compare the projected model in IMPACT-Z [54], `elegant` and CSRtrack’s [55] 2D ‘g\_to\_m’ method to experimental results. However, the properties of the electron beam; namely, that it is long compared to the transverse dimension and so effectively 1D in nature, suggest that good agreement is expected, as was observed.

Though the discrepancy between 1D and 2D CSR models has not been seen to be especially large, it would still be expected to present on some level. It is thus important to examine the lattice and beam conditions of the JLab FEL to determine whether the projected model should be expected to hold. This validity is normally gaged using the Derbenev criterion [21], a comparison of the beam transverse and longitudinal dimensions while in a dipole magnet. This criterion is violated through large portions of the JLab FEL BC1 chicane. It is therefore necessary and also interesting to compare the 1D results to a more comprehensive CSR model. Here we will show results using CSRtrack’s 2D ‘g\_to\_p’ model that uses a pseudo-Green’s function approach with Gaussian sub-bunches [56]. As will be shown the differences observed in the average properties of the bunch between the 1D model and 2D

model are not significant. Our previous observations, both experimental and in simulation, namely, the average energy loss and bunch fragmentation agree very well between the 1D and 2D models. However, there are novel effects that can be observed in the 2D simulation of the beam passing through the chicane region that seem to be related to transverse particle motion. It is possible that such effects might be exploited to provide a direct observation of 2D CSR effects in an experiment.

### 5.1. THE DERBENEV CRITERION

As previously discussed in Chapter 2 the projected 1D CSR model commonly used to perform beam simulations including CSR effects should in theory suffer in accuracy the further the beam shape diverges from a line in the  $x$ - $t$  plane. The geometric criterion employed in determining whether the 1D projected model is valid is

$$(60) \quad \sigma_x \left( \frac{1}{R\sigma_z^2} \right)^{\frac{1}{3}} \ll 1,$$

where  $\sigma_x$  is the beam size in the bending plane of the dipoles of the chicane,  $R$  is the bending radius of the dipoles, and  $\sigma_z$  is the bunch length. For a bunch of length  $\sigma_z$  traveling through some angle  $\phi$  on an arc of radius  $R$  (shown in Fig. 5.1) the overtaking length is the distance the bunch will travel along the arc before the radiation from the tail of the bunch reaches the head.

For  $\phi \ll 1$  this overtaking length will be approximately the line  $AB$  in Fig. 5.1 and will be given in terms of  $R$  and  $\sigma_z$  as

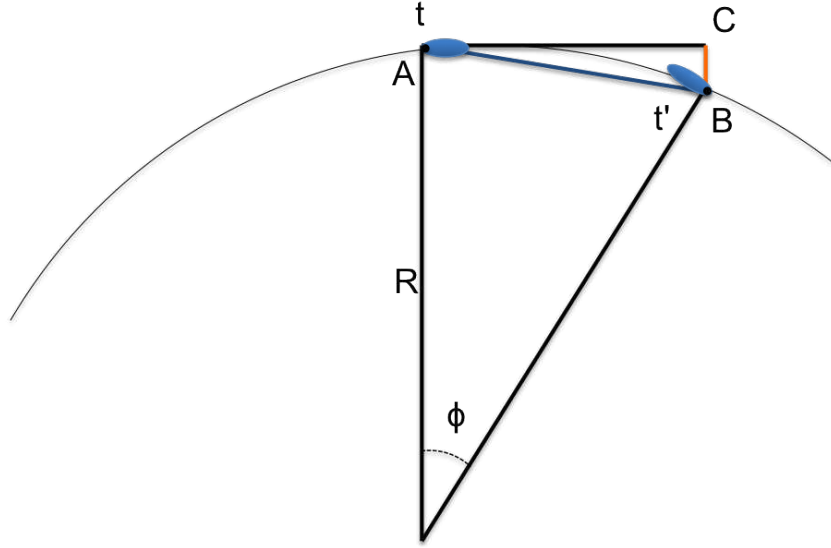


FIGURE 5.1. For radiation emitted from the tail of a bunch at some time  $t$

$$(61) \quad AB \approx (24R^2\sigma_z)^{\frac{1}{3}}.$$

From this it is then easy to find  $BC$  in terms of the same parameters

$$(62) \quad BC \approx 2(24R\sigma_z^2)^{\frac{1}{3}}.$$

The expectation in the 1D CSR model that all particles should follow the central trajectory then requires that

$$(63) \quad \frac{\sigma_x}{BC} \ll 1.$$

This requirement is sometimes referred to as the Derbenev criterion [21]; we will define

$$(64) \quad \kappa \equiv \sigma_x \left( \frac{1}{R\sigma_z^2} \right)^{\frac{1}{3}},$$

as the Derbenev parameter. In theory  $\kappa$  should provide a measure of the divergence between the 1D projection and a more complete 2D model, such as used in CSRtrack. In regions such as the final dipoles of the chicane the beam will be dispersed in the bending plane creating a larger apparent size  $\sigma_x$ , while the bunch length will have become quite short, leading possibly to large values for  $\kappa$ . With the short bunch length, CSR production will be maximized, creating a potentially troublesome situation where the 1D model could fail at a position where the CSR effect is the most potent.

For the JLab BC1 chicane the parameter  $\kappa$  is plotted in Fig. 5.2 along the length of the beamline using beam parameters from the `elegant` model. Three cases are shown based on the bunch compression state at the end of chicane. The under-compressed bunch, that is a bunch exiting the chicane with a positive chirp, and an  $R_{56}$  setting in the first arc of  $R_{56}^{A1} = 0.695$  m. The critically-compressed bunch, which is fully upright and has no chirp, which will be for  $R_{56}^{A1} = 0.655$  m. Finally the over-compressed bunch, which will exit the chicane with a negative chirp, at  $R_{56}^{A1} = 0.614$  m. The maximum value of  $\kappa$  occurs, as expected, in the third dipole where dispersion is high and the bunch length is short. While the bunch length can be even shorter in the fourth dipole the dispersion is trending to zero at the end of the chicane due to its achromatic design, greatly reducing  $\kappa$ . The rollover that is observed in the third dipole is due to the longitudinal dynamics of the bunch as it undergoes compression. Here the over-compressed bunch will over-rotate in the third dipole, passing through maximum compression and flipping the sign of its chirp before increasing in length again. However, the critically compressed case also begins roll-over within the third

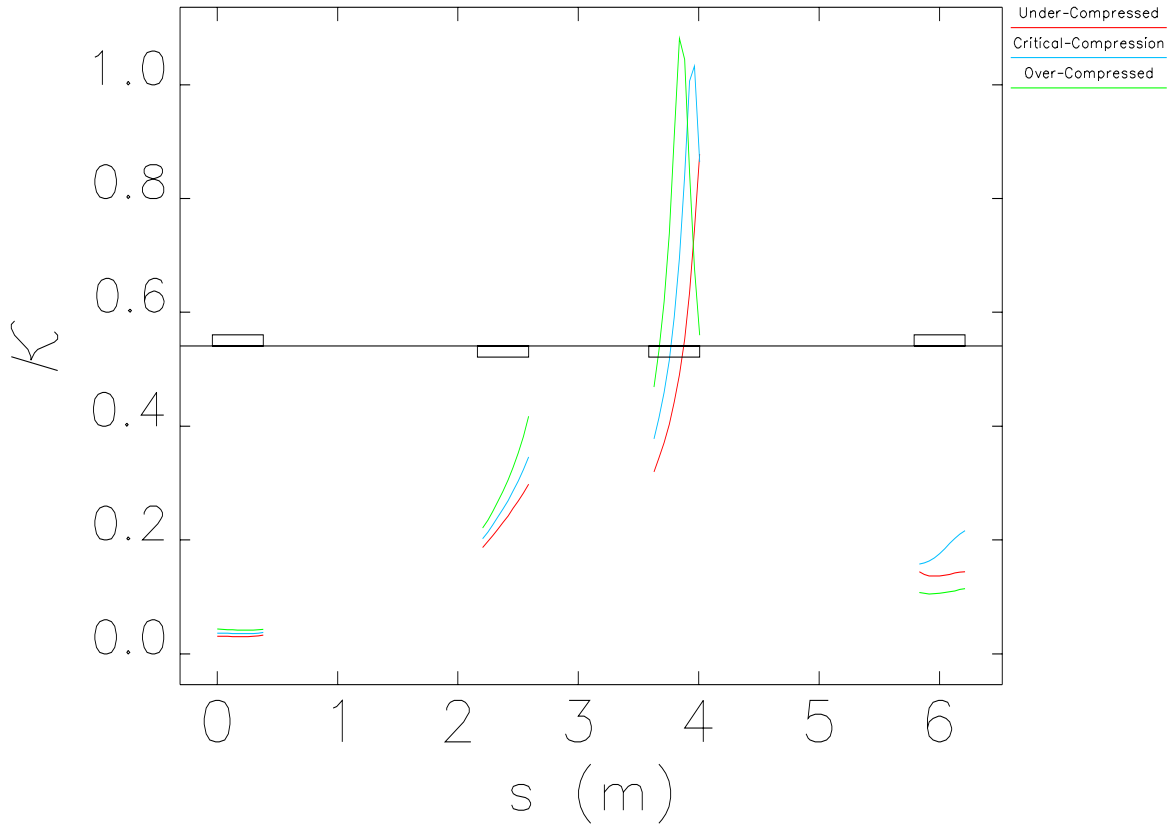


FIGURE 5.2. The Derbenev parameter, defined in Eq. 64, is plotted as a function of position within the BC1 chicane. Three cases are shown, under-compressed in red, critically-compressed in blue, and over-compressed in green.

dipole. This is because the fourth dipole provides a small positive momentum compaction term. Thus, for full compression the bunch will slightly over-compress in dipole three before rolling back upright in the final dipole. We would expect, then, that if there is significant deviation between the 1D and 2D simulations it would occur in and immediately after the third dipole as this is both where  $\kappa$  reaches its maximum and where the integrated value of the CSR effect will be at its highest local level.

## 5.2. BC1 CHICANE MODEL IN CSRTRACK

Because of the greatly increased computational effort for calculating the CSR field in 2D we model in CSRtrack only the BC1 chicane. To be able to study the CSR in the drift a 4 m drift space included beyond the end of the final dipole of the chicane to allow for continued interaction between the co-propagating CSR and electron bunch. This drift is included in both CSRtrack and `elegant`. After 4 m, the energy loss rate has fallen by a factor of 100 and should no longer be relevant.

Fig. 5.3 shows a comparison of the particle phase space at the end of the chicane, for an over-compressed bunch, as computed by `elegant` and CSRtrack. Both simulations were performed with CSR off. The match between the two models is excellent in the longitudinal plane; however, as shown in 5.3 (a) and (b) the horizontal and vertical planes do not match as well. This is due to the impact on particles by the fringe field of the dipole in CSRtrack. The fringe fields are included in CSRtrack, but field parameters are not controllable.

Since only the chicane is modeled in CSRtrack the initial beam distribution at the BC1 entrance is taken from the full lattice simulation in `elegant`. The distribution at the chicane entrance is then down-sampled to 25k macroparticles. The down-sampling is performed randomly using the `sddsprocess` program. This distribution is then converted to the ASTRA input format [57] which is accepted by CSRtrack. While the lower macroparticle count is necessary to prevent prohibitively long run-times this random sampling does induce a level of jitter into the bunch statistics. This jitter, while small, is particularly appreciable for the energy loss measurement where the fractional energy difference between the `elegant` distribution and the sample distribution used in CSRtrack can be almost 15% of the total fractional energy loss from CSR along the chicane. Fortunately, in the ultra-relativistic regime the CSR force is energy-independent as long as  $\sigma_z > R/c\gamma^3$  [19]. For the BC1

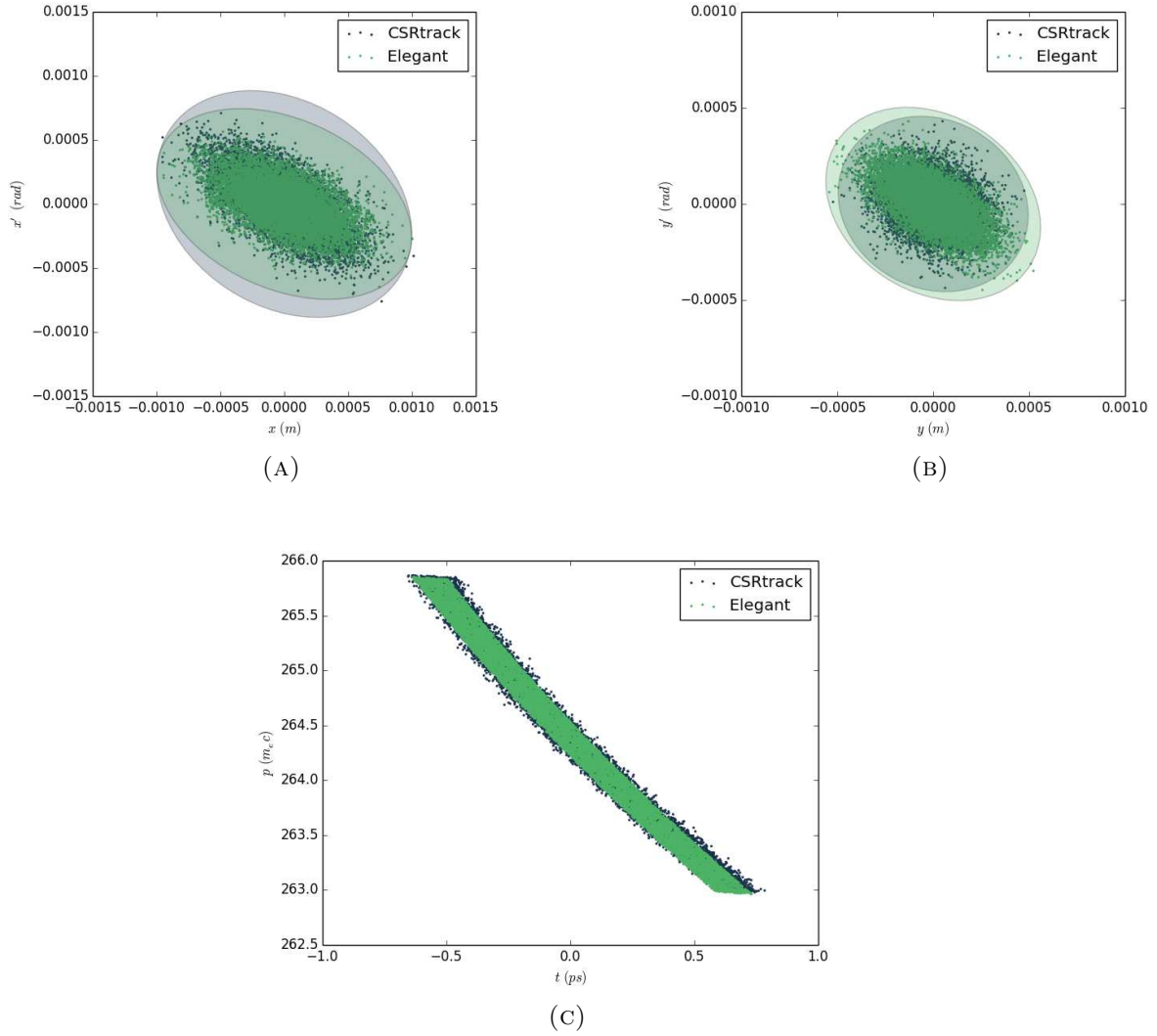


FIGURE 5.3. Comparison between CSRtrack and Elegant in blue and green respectively with CSR calculations turned off in both simulations. Shown from the top left going clockwise are the horizontal phase space (in the bending plane), the vertical phase space, and the longitudinal phase space. For the horizontal and vertical planes the ellipse calculated from the Twiss parameters of each bunch is shown.

chicane  $\sigma_z$  is at a minimum 150 fs while  $R/c\gamma^3$  is 0.2 fs, so this method should not perturb the results. To remove this jitter from the data all energy loss values must be normalized by the initial average energy of the bunch for that simulation step.

### 5.3. SIMULATION RESULTS AND ANALYSIS

Due to only including the BC1 chicane we are restricted to only making comparisons between the simulated results and cannot make any direct comparison to measurement data. For the comparisons shown here the `elegant` model, used previously, is compared against CSRtrack. CSRtrack can be run in both 1D and 2D CSR modes with the 1D mode using an equivalent model to that employed by `elegant`. In the `elegant` simulations the quadrupole strength of the A1 quadrupoles is scanned with shifts of 3.4 mm in  $R_{56}^{A1}$ . To limit the computation time we choose to simulate intervals of 13.6 mm of momentum compaction in CSRtrack. Since only the BC1 chicane is modeled, we constrain the scan to the region around full compression at the end of BC1, from  $R_{56}^{A1} = 0.55$  to 0.75 m. Fig. 5.4 shows the comparison of energy loss versus momentum compaction in A1 for the 1D model in both CSRtrack and `elegant` and the 2D model in CSRtrack. All three cases show good agreement. The 2D CSR model does have slightly higher energy loss on average, though the level of discrepancy would be too small to be resolved experimentally. Notionally, it might be expected that the total energy loss would be reduced in the 2D model as compared to the 1D model due to the fact that in the 1D projection the electron separation distances will tend to be underestimated. However, this is not seen in the result here, nor is it clearly shown to be the case in other studies that show a mix of results [28, 58–61]. It is clear, then, that the situation is somewhat more nuanced than this simple approach would suggest.

To gain a better understanding of where one sees a divergence between the 1D and 2D models we first look at the level of compression at the end of the chicane. In Fig. 5.5 the bunch length at the end of the chicane is plotted for the three models, again as a function of the A1 arc momentum compaction. The result shows that there is no difference

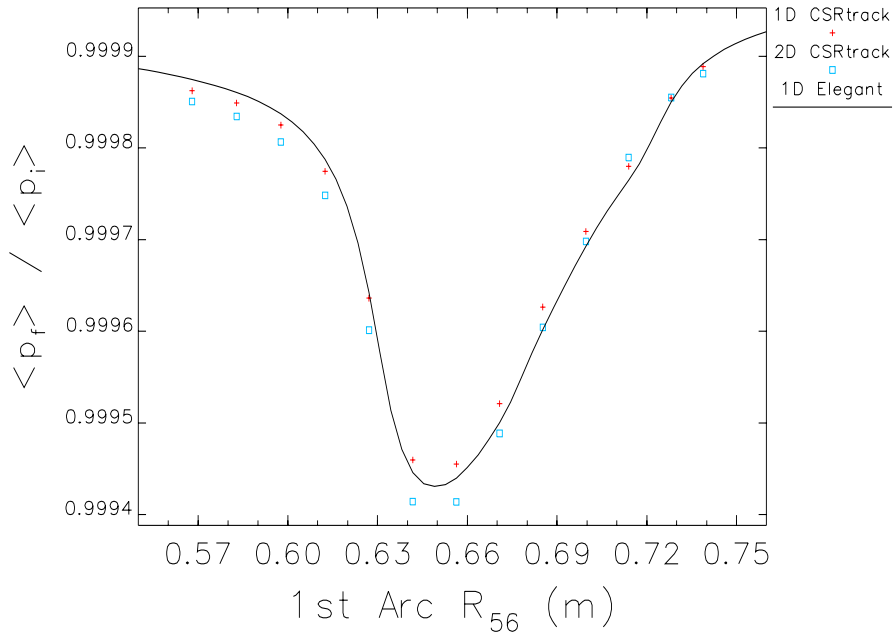


FIGURE 5.4. The energy loss due to CSR in the BC1 chicane is plotted as a function of  $R_{56}^{A1}$ , the momentum compaction, in the first arc. The black line shows the result for Elegant, the red and blue symbols show the 1D and 2D results from CSRtrack.

in compression between any of the models. This is reassuring and quickly removes from consideration one of the more obvious sources of possible discrepancy between the models.

We next turn to looking at the average energy loss as a function of position in the chicane. In the case of an under-compressed bunch, corresponding to  $R_{56}^{A1} = 0.695$  m and shown in Fig. 5.6, it is seen that the most significant deviation occurs in the drift space between the third and fourth dipoles. Almost all bunch compression has completed by the end of the third dipole so the bunch is very close to its minimum length, under these conditions, at this point. The peculiarity shown in the 2D model in this drift region is that rather than the rate of energy loss tapering off there is actually a clear increase in the rate of energy loss, as the bunch approaches the entrance to the fourth dipole.

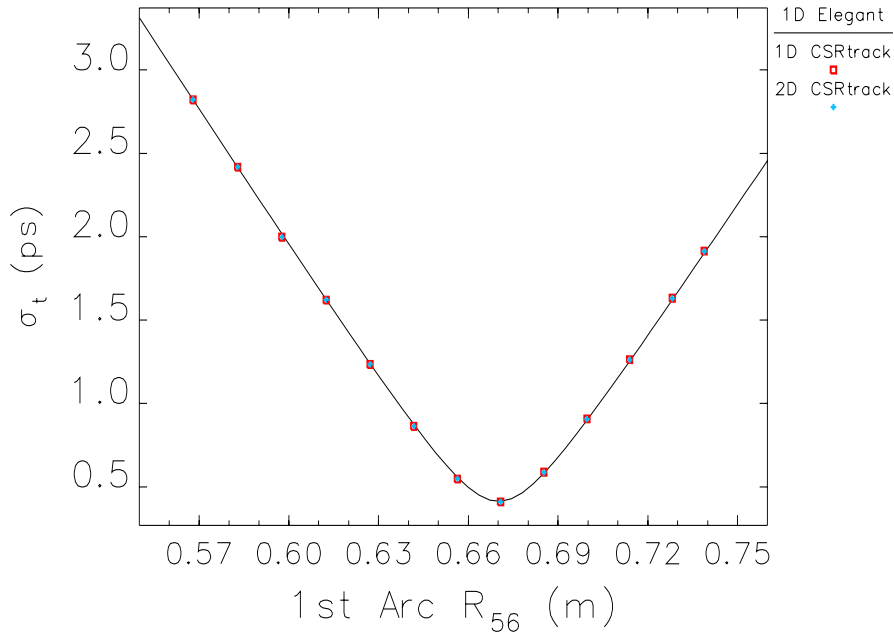
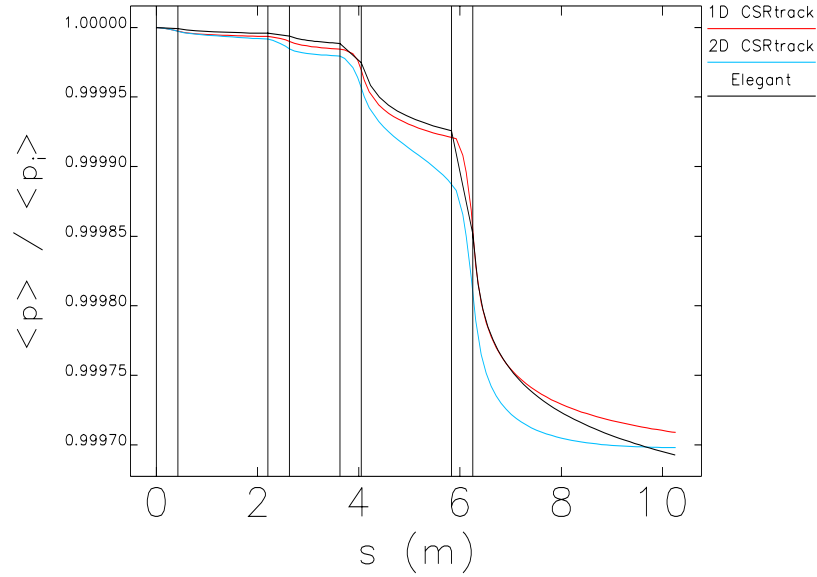
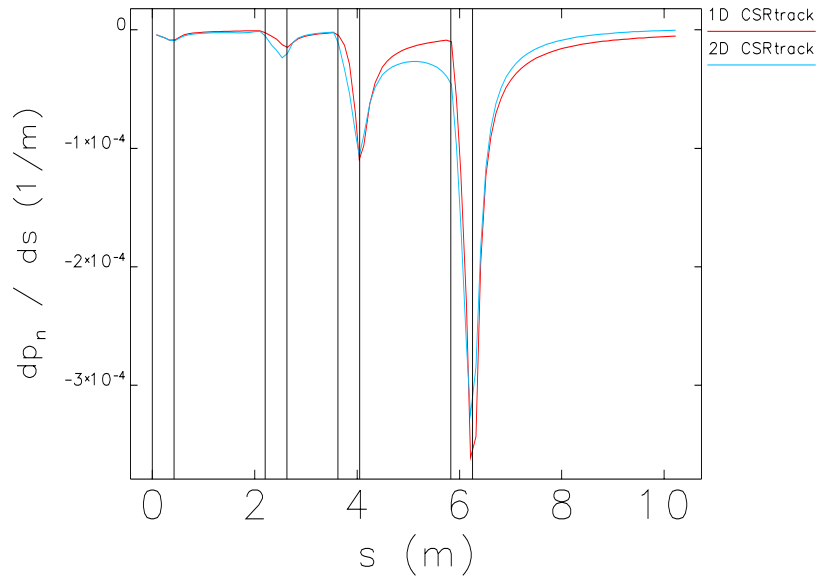


FIGURE 5.5. The bunch length at the end of the BC1 chicane is plotted as a function of  $R_{56}^{A1}$ , the momentum compaction, in the first arc. The black line shows the result for Elegant, the red and blue symbols show the 1D and 2D results from CSRtrack. Note that red and blue symbols are directly over top of each other.

Much the same behavior is observed in the critically-compressed case ( $R_{56}^{A1} = 0.655$  m, shown in Fig. 5.7). Again, the only significant deviation occurs in the drift between the final two dipoles, and again the rate of energy loss is observed to increase in the latter half of the drift. This change in energy loss rate corresponds to a rotation of the bunch in the horizontal phase space. The  $\beta_x$  function is steadily decreasing in this drift and reaches a minimum immediately before the entrance to the fourth dipole. In contrast, within the drift downstream of the chicane  $\beta_x$  is rapidly increasing corresponding to the more rapid dying-off of energy loss in the 2D CSR simulation when compared to the 1D result. The effect of this rotation is examined in more detail later.

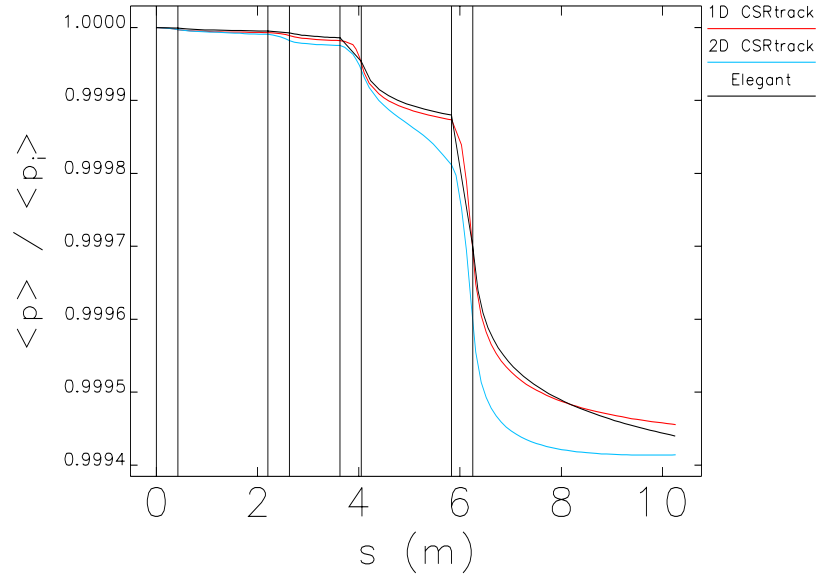


(A)

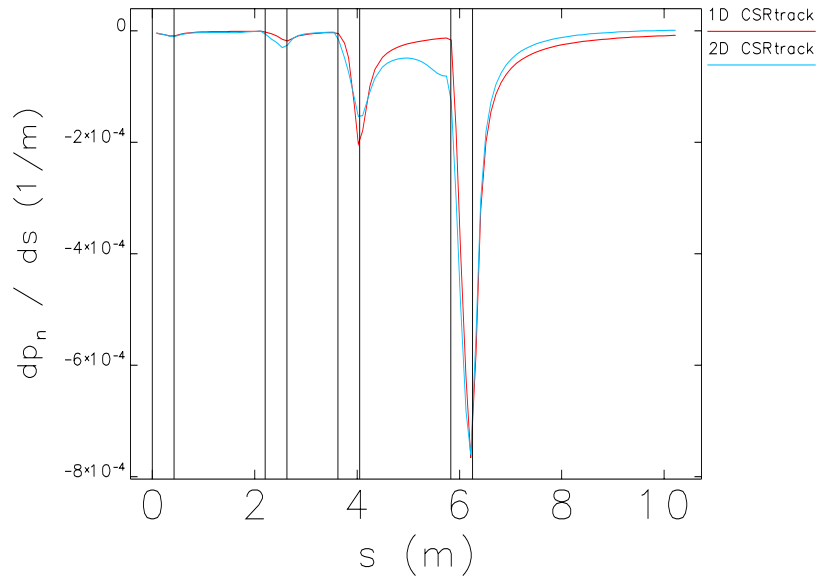


(B)

FIGURE 5.6. Shown in (a) is the energy loss as a function of position in the BC1 chicane for  $R_{56}^{A1} = 0.695$  m with the 1D and 2D CSRtrack results shown in red and blue respectively and the 1D result from Elegant in black. The rate of energy loss  $\frac{d\langle p \rangle}{\langle p_i \rangle ds}$  is shown in (b). The vertical black lines represent the boundaries of the four dipoles.



(A)

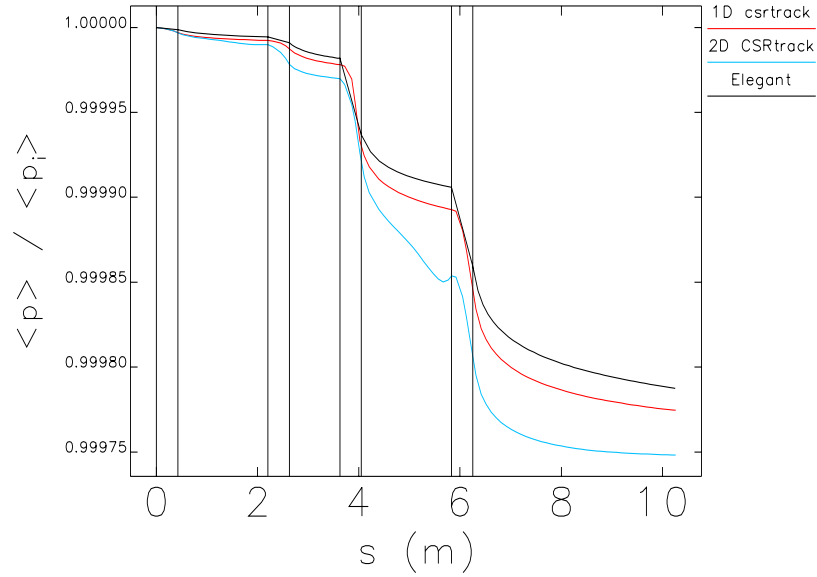


(B)

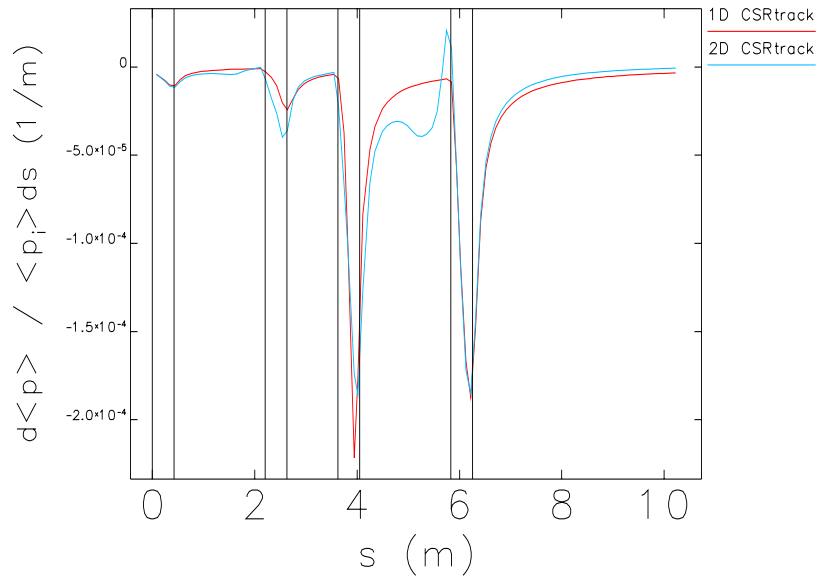
FIGURE 5.7. Shown in (a) is the energy loss as a function of position in the BC1 chicane for  $R_{56}^{A1} = 0.655$  m with the 1D and 2D CSRtrack results shown in red and blue respectively and the 1D result from Elegant in black. The rate of energy loss  $\frac{d\langle p \rangle}{\langle p_i \rangle ds}$  is shown in (b). The vertical black lines represent the boundaries of the four dipoles.

While the region of interest remains the same in the over-compressed case, with  $R_{56}^{A1} = 0.614$  m, in Fig. 5.8, the effect that is observed is quite different. Here there is actually a small, but significant, energy gain region starting out 0.15 m from the entrance to the final dipole. This energy gain appears to be related to particle motion in the  $x$ -axis. Shown in Fig. 5.9 is the bunch distribution in the  $x'$ - $t$  plane. The particle coloring is based on particle energy change between two successive simulation steps 0.1 m apart with the initial position located 0.25 m from the edge of the fourth dipole. Regions of energy loss or gain are highly clustered in  $x'$ - $t$ . In general the region of maximum energy change occurs at the position of peak current in  $t$ . For the critically compressed case (Fig. 5.9(a)) the bunch assumes a sharply-peaked, Gaussian distribution with minimal tails. However, for the over-compressed case (Fig. 5.9(b)) the current distribution is very asymmetric and peaks around 2 ps with a long tail trailing behind. Whether particles in the band around the peak current gain or lose energy seems to be determined by their movement in  $x$ . For critical-compression the majority of the bunch is losing energy with only one small region showing significant energy gain with those particles moving sharply towards the inside of the chicane. In the case of the over-compressed bunch most of the tail is experiencing no change in energy. Particles gaining energy are located at the head of the bunch and are all at positions  $x' < 0$ . This correlation between energy change and  $x'$  might suggest that there could be a significant contribution from horizontal CSR fields contributing a strong  $v_x E_x$  term to the energy change.

Ultimately, while significant differences appear when the electron beam evolution is examined along the chicane, the integrated result at the end of the chicane does not seem to deviate substantially between the 1D and 2D models. On one hand, it is reassuring that the computationally non-intensive 1D model seems to provide reliable results even when a key assumption upon which it is built would seem to be violated for this experiment (see Fig.



(A)



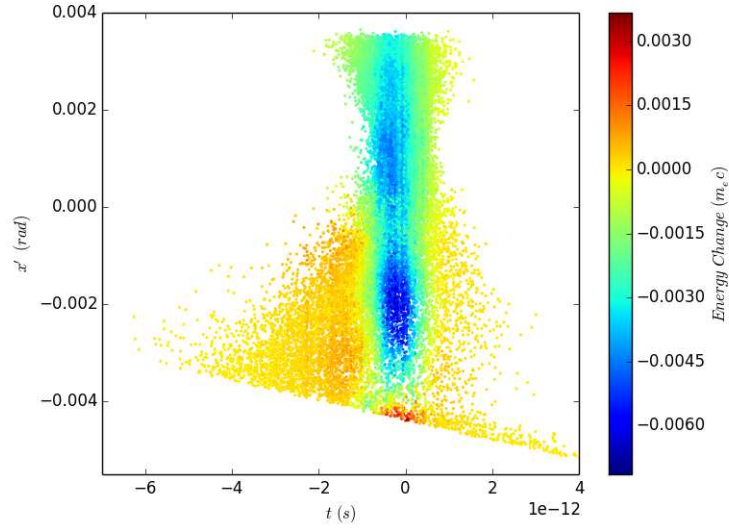
(B)

FIGURE 5.8. Shown in (a) is the energy loss as a function of position in the BC1 chicane for  $R_{56}^{A1} = 0.612$  m with the 1D and 2D CSRtrack results shown in red and blue respectively and the 1D result from Elegant in black. The rate of energy loss  $\frac{d\langle p \rangle}{\langle p_i \rangle ds}$  is shown in (b). The vertical black lines represent the boundaries of the four dipoles.

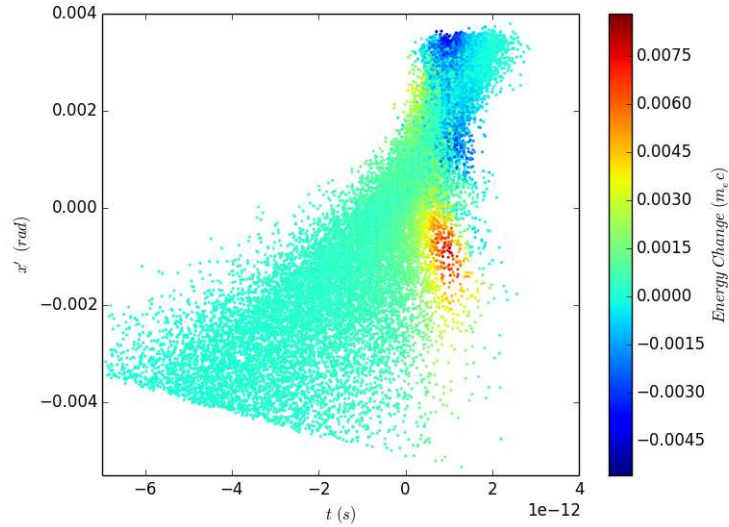
5.2). At the same time, it is unfortunate that we would seem to be denied an opportunity to better validate the relatively unvetted 2D CSR models since we only have the data set here. However, this study does suggest some hope in this regard. If the local properties of the CSR energy loss within the bunch can be strongly influenced through manipulation of the x-plane distribution of the bunch it may be possible to perform an experiment that would expect to produce a measurable deviation between observed result and the expected outcome within a 1D simulation. If such an experiment could be performed in this manner it would certainly be quite novel, both for direct testing for a 2D CSR effect and for reliance on manipulation of the transverse phase space to impact CSR interaction, rather than varying bunch compression.

5.3.1. ENERGY SPECTRUM FRAGMENTATION. One advantage to CSRtrack is that space charge forces are automatically included when tracking with the 2D CSR model. This allows for easy comparison to `elegant` and its 1D LSC model. The downside is that internally, within CSRtrack, no distinction is made between forces from CSR and those from space charge. Thus a direct comparison of the LSC field between the two simulations is not possible at arbitrary points along the beamline. We can, however, compare the energy spectrum at the end of each simulation to see how the combined CSR/LSC forces have impacted it. Given that `elegant`'s 1D LSC model includes a number of assumptions about beam properties and was originally implemented to study microbunching [46], and not as a general space charge model, there exists some question about whether it is valid to use in modeling our experiment.

The energy spectrum of the bunch at the end of the 4 m downstream drift is shown in Fig. 5.10. The 1D CSR model in CSRtrack does not include any space charge forces and shows only very small levels of fragmentation. However, we see that the 2D CSRtrack results



(A)



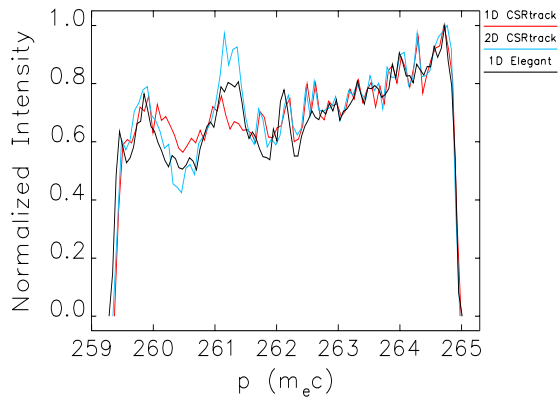
(B)

FIGURE 5.9. Plots  $x'-t$  for (a) the critically-compressed bunch and (b) the over-compressed bunch. The heat map is based upon energy change between two successive steps in the simulation starting 0.25 m from the entrance to the fourth dipole. (Note that in this plot  $t > 0$  is the head of the bunch.)

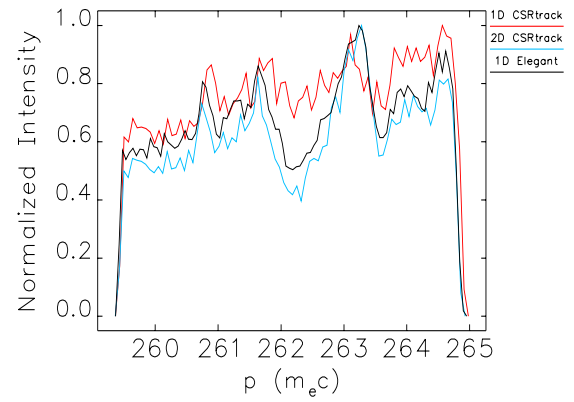
match very well with result from `elegant`, which uses 1D models for both CSR and LSC.

This agreement suggests that the use of `elegant` is appropriate in this regime and validates

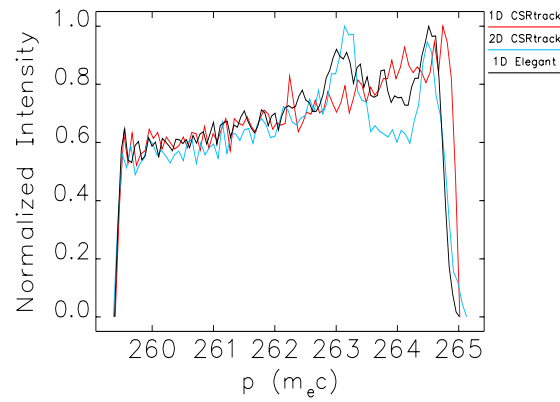
our previous work shown on the study of the energy spectrum fragmentation



(A)



(B)



(C)

FIGURE 5.10. The energy spectrum is plotted for the under-compressed, critically-compressed, and over-compressed cases in (a), (b), and (c). The 1D CSRtrack result is shown in red, the 2D CSRtrack in blue, and 1D Elegant in black.

## CHAPTER 6

# CONCLUSION

In this work, we outlined the utility of electron-beam-based light sources and describe in detail several important collective effects that can lead to a decrease in performance of these systems, namely coherent synchrotron radiation (CSR) and longitudinal space charge (LSC). As a push continues to higher average power the energy recovery linac (ERL) is becoming a very attractive option for a number of proposed facilities, both for light sources and particle accelerators for nuclear physics. The impact of CSR and LSC on the electron beam has the potential to damage the electron beam and may be particularly severe in ERLs due to the large number of dipoles required as compared to a standard, single-pass linac. This makes the study of CSR and other collective beam effects critical to the successful construction of the next generation of light sources and other accelerators, such as the MEIC ERL cooling ring.

We have shown the results from an experiment performed on the Jefferson Laboratory (JLab) ERL driven FEL. The JLab FEL is capable of providing kilowatts of average power in the IR spectrum. The capabilities of this FEL make it a world-class test-bed for studying collective effects in an ERL. In our experiment we studied how CSR emission varies as a function of compression point within the machine. The unique structure of the JLab FEL with its control of momentum compaction using the recirculation arcs and multiple chicane makes this experiment particularly unique. With this structure we were able to study multiple compression points on both sides of the acceleration rf wave. A comparison of the data collected to simulations using `elegant` and the 1D CSR model of Saldin et al. showed good agreement between experiment and simulation. This is the first time that such

experimental validation of the use of `elegant` to model CSR over such a broad range of longitudinal dynamics has been shown. This work provides reassurance that the 1D CSR model remains a useful tool for studying the design of recirculation arcs in future ERLs.

In addition, data was also collected of the energy spectrum of the beam as a function of compression. From this data a 'fragmentation' of the energy spectrum was observed. The energy around which fragmentation is centered varies in a regular fashion based upon compression point. Simulation in `elegant` showed that this fragmentation is, in part, the result of CSR propagating into the drift space beyond the chicanes and arcs where it will continue to interact with the beam. This result highlights the need to include accurate modeling of CSR-beam interaction outside of dipoles, as there are still critical interactions outside of the dispersive dipole regions. Also of importance, it was shown that the sextupoles, employed to remove longitudinal curvature and improve compression also will compensate for this fragmentation effect, creating a more uniform energy spectrum. The energy fragmentation effect has been observed at a number of accelerators previously but a complete explanation of how to remove the effect has never been shown prior to this. While CSR in the drift space plays into this fragmentation, simulation also showed that longitudinal space charge (LSC) can be an even more dominant contributor to the fragmentation effect. Fortunately, removing the sharp current spike that arises from non-linear compression can help to significantly alleviate the contribution of LSC to fragmentation.

Finally, the results of 2D CSR simulations in `CSRtrack` were shown. These simulations show, in general, good agreement between the 2D CSR model and the 1D model in both `CSRtrack` and `elegant`. However, there were observed peculiarities in the rate of energy change in the drift spaces following dipoles where the beam was strongly compressed. While this effect does not seem to significantly alter the average properties of the beam, it may

provide a mechanism by which to directly observe discrepancies between the 1D and 2D CSR models using a carefully designed experiment. This would be significant in allowing a path forward to directly test more complete 2D and 3D CSR models.

The work shown here demonstrates the importance of having a full understanding of CSR, if future ERL-based accelerators are to be successful. A method of reducing the impact of CSR on the electron bunch energy spectrum was demonstrated theoretically and in simulation. However, ultimately this work should be tested directly in an actual ERL. An experimental study on the impact to CSR of longitudinal phase space curvature manipulations via sextupoles would provide a much greater understanding of the effects shown in this work. In addition, while the 1D CSR model has proven a very effective tool the parameter space within which it is applicable is still not understood. In order to have confidence in future ERL designs it is necessary to more fully test for 2D and 3D CSR effects. Simulations we have shown, with CSRtrack, suggest that an experiment focusing on imaging bunch structure might be able to resolve discrepancies between the 1D and 2D CSR models. This would provide more information about the bounds of the 1D CSR model. As we continue to push the boundaries of technical progress in particle accelerators we must make sure that we have an increasingly more precise understanding of all relevant effects on the beam. This will only be achieved, ultimately, through continued experimental study to validate and refine our theories and simulation.

## REFERENCES

- [1] W. Henning, *Accelerators for America's Future*. Sandbox Studio, 2010.
- [2] H. Winick and S. Doniach, *Synchrotron Radiation Research*. Plenum Press, 1980.
- [3] J. Hemminger, “Future light sources report,” Tech. Rep. BESAC-DOE, BESAC, 2013.
- [4] M. Tigner, “A possible apparatus for electron clashing-beam experiments,” *Il Nuovo Cimento (1955-1965)*, vol. 37, no. 3, pp. 1228–1231, 1965.
- [5] G. Hoffstaetter, “Cornell energy recovery linac,” Tech. Rep. Cornell University Project Definition Design Report, Cornell, 2013.
- [6] A. Accardi *et al.*, “Electron ion collider: the next QCD frontier - understanding the glue that binds us all,” 2012.
- [7] R. Ryne *et al.*, “Using a lienard-wiechert solver to study coherent synchrotron radiation effects,” in *Proceedings of the 2013 FEL Conference*, (New York, NY, USA), pp. 17–23, 2013.
- [8] Y. Derbenev and Y. Zhang, “Electron cooling for electron-ion collider at jlab,” in *Proceedings of COOL09*, (Lanzhou, China.), pp. 181–184, 2009.
- [9] C. Tennant and D. Douglas Tech. Rep. JLAB-TN-12-027, JLAB, 2012.
- [10] D. Douglas *et al.*, “Control of synchrotron radiation effects during recirculation,” in *Proceedings of the 2015 International Particle Accelerator Conference*, (Richmond, VA, USA.), pp. 1913–1915, 2015.
- [11] C.-Y. Tsai, D. Douglas, R. Li, and C. Tennant, “Theoretical investigation of coherent synchrotron radiation induced microbunching instability in transport and recirculation arcs,” *ArXiv e-prints*, Aug. 2014.

- [12] D. Douglas, S. V. Benson, G. A. Krafft, R. Li, L. Merminga, and B. C. Yunn, “Driver Accelerator Design for the 10 kW Upgrade of the Jefferson Lab IR FEL,” in *Proceedings of LINAC01*, no. physics/0008032, 2000.
- [13] D. Douglas, “A thz suppression chicane for the fel upgrade energy recovery transport (ir upgrade design revision 113b),” Tech. Rep. JLAB-TN-04-028, JLAB, September 2004.
- [14] A. A. Lienard *L’Eclairage Electr.*, vol. 16, no. 5, 1898.
- [15] J. E. Wiechert *Archives Neerlandaises*, no. 549, 1900.
- [16] J. Blewett *Phys. Rev.*, vol. 69, no. 87, 1946.
- [17] J. Schwinger *Phys. Rev.*, vol. 75, no. 1912, 1949.
- [18] H. Wiedemann, *Particle Accelerator Physics*. SpringerLink: Springer e-Books, Springer Berlin Heidelberg, 2007.
- [19] E. Saldin, E. Schneidmiller, and M. Yurkov, “On the coherent radiation of an electron bunch moving in an arc of a circle,” *Nuclear Instruments and Methods in Physics Research Section A: Accelerators, Spectrometers, Detectors and Associated Equipment*, vol. 398, no. 23, pp. 373 – 394, 1997.
- [20] R. Hajima, “A first-order matrix approach to the analysis of electron beam emittance growth caused by coherent synchrotron radiation,” *Japanese Journal of Applied Physics*, vol. 42, no. 8A, p. L974, 2003.
- [21] Y. S. Derbenev, J. Rossbach, E. L. Saldin, and V. D. Shiltsev, “Microbunch radiative tail-head interaction,” Tech. Rep. TESLA-FEL 95-05, TESLA, 1995.
- [22] M. Borland, Y. C. Chae, S. Milton, R. Soliday, V. Bharadwaj, P. Emma, P. Krejcik, C. Limborg, H. Nuhn, and M. Woodley, “Start-to-end jitter simulations of the linac coherent light source,” in *Proceedings of the PAC01*, (Chicago, IL, USA.), p. 2707, 2001.

- [23] S. Benson, K. Beard, G. Biallas, J. Boyce, D. Bullard, J. Coleman, D. Douglas, F. Dylla, R. Evans, P. Evtushenko, *et al.*, “High power operation of the jlab ir fel driver accelerator,” in *Particle Accelerator Conference, 2007. PAC. IEEE*, pp. 79–81, IEEE, 2007.
- [24] S. V. Benson, G. H. Biallas, J. L. Coleman, C. Dickover, D. Douglas, P. Evtushenko, M. Marchlik, D. W. Sexton, and C. Tennant, “Electron Beam Diagnostics of the JLab UV FEL,” *Conf. Proc.*, vol. C110328, pp. 1446–1448, 2011.
- [25] P. Piot, D. R. Douglas, and G. A. Krafft, “Longitudinal phase space manipulation in energy recovering linac-driven free-electron lasers,” *Phys. Rev. ST Accel. Beams*, vol. 6, no. 030702, 2003.
- [26] H. Braun *et al.*, “Emittance growth and energy loss due to coherent synchrotron radiation in the bunch compressor of the clic test facility (ctf ii),” in *Proceedings of the European Particle Accelerator Conference*, (Vienna, Austria.), pp. 471–473, 2000.
- [27] M. Borland and J. Lewellen in *Proceedings of the 2001 Particle Accelerator Conference*, (Piscataway, NJ, USA.), p. 2823, 2001.
- [28] K. L. F. Bane *et al.*, “Measurements and modeling of coherent synchrotron radiation and its impact on the linac coherent light source electron beam,” *Phys. Rev. ST Accel. Beams*, vol. 12, p. 030704, Mar 2009.
- [29] E. Saldin, E. Schneidmiller, and M. Yurkov, *The Physics of Free Electron Lasers*. Advanced Texts in Physics, Springer, 2000.
- [30] C. Hernandez-Garcia, T. Siggins, S. Benson, D. Bullard, H. F. Dylla, K. Jordan, C. Murray, G. R. Neil, M. Shinn, and R. Walker, “A high average current DC GaAs photocathode gun for ERLs and FELs,” *Conf. Proc.*, vol. C0505161, p. 3117, 2005. [3117(2005)].
- [31] B. C. Yunn, “Physics of JLAB FEL Injector,” *Conf. Proc.*, 1999.

- [32] J. R. Delayen *et al.* in *Proceeding of the 199 Particle Accelerator Conference*, (New York, NY), pp. 934–936, 1999.
- [33] J. B. Flanz and C. P. Sargent, “Operation of an isochronous beam recirculation system,” *Nucl. Inst. Meth.*, vol. A241, pp. 325–333, 1985.
- [34] J. B. Flanz, S. Kowalski, and C. P. Sargent, “An isochronous beam recirculation magnet system,” in *Proceedings of the Particle Accelerator Conference*, (Washington D.C.), pp. 2847–2849, 1981.
- [35] A. Smirnov *et al.* in *Proceedings of the 2003 Particle Accelerator Conference*, (Portland, OR), pp. 2135–2137, 2003.
- [36] D. Douglas, “Ir upgrade octupole trim requirements,” Tech. Rep. JLAB-TN-01-036, JLAB, August 2001.
- [37] D. Douglas, “Longitudinal phase space management in the ir upgrade fel driver,” Tech. Rep. JLAB-TN-00-020, JLAB, 2000.
- [38] M. Borland *Phys. Rev ST Accel. Beams*, vol. 4, p. 070701, 2001.
- [39] C. Tennant, D. Douglas, R. Li, and C.-Y. Tsai, “Studies of coherent synchrotron radiation in the Jefferson Lab FEL driver with implications for bunch Compression,” in *Proceedings, 27th Linear Accelerator Conference, LINAC2014*, p. MOPP139, 2014.
- [40] M. Borland, “elegant: A flexible sdds-compliant code for accelerator simulation,” *Advanced Photon Source*, vol. LS-287, September 2000.
- [41] J. Rosenzweig *et al.*, “Space-charge oscillations in a self-modulated electron beam in multi-undulator free-electron lasers,” Tech. Rep. TESLA-FEL-96-15, DESY, 1996.
- [42] A. Savitzky and M. J. Golay, “Smoothing and differentiation of data by simplified least squares procedures.,” *Analytical chemistry*, vol. 36, no. 8, pp. 1627–1639, 1964.
- [43] D. Douglas. private communication.

- [44] R. Li, “Sensitivity of the csr self-interaction to the local longitudinal charge concentration of an electron bunch,” *Nucl. Instr. and Meth. A.*, vol. 475, no. 13, pp. 498 – 503, 2001.
- [45] P. Piot *et al.*, “Emittance and energy spread studies in the jefferson lab free-electron laser,” in *Proceedings of the European Particle Accelerator Conference*, (Vienna, Austria.), pp. 1546–1548, 2000.
- [46] Z. Huang *et al.*, “Suppression of microbunching instability in the linac coherent light source,” *Phys. Rev. ST Accel. Beams*, vol. 7, p. 074401, Jul 2004.
- [47] M. Borland, “Modeling of the microbunching instability,” *Phys. Rev. ST Accel. Beams*, vol. 11, p. 030701, Mar 2008.
- [48] E. Saldin, E. Schneidmiller, and M. Yurkov, “Klystron instability of a relativistic electron beam in a bunch compressor,” *Nuclear Instruments and Methods in Physics Research Section A: Accelerators, Spectrometers, Detectors and Associated Equipment*, vol. 490, pp. 1 – 8, 2002.
- [49] A. W. Chao, *Physics of Collective Beam Instabilities in High Energy Accelerators*. Wiley.
- [50] S. Di Mitri, M. Cornacchia, S. Spampinati, and S. Milton, “Suppression of microbunching instability with magnetic bunch length compression in a linac-based free electron laser,” *Phys. Rev. ST Accel. Beams*, vol. 13, Jan 2010.
- [51] G. Bassi *et al.*, “Comparison of 1d and 2d csr models with application to the fermi@elettra bunch compressors,” in *Proceedings of 2011 Particle Accelerator Conference*, (New York, NY, USA.), pp. 1734–1745, 2011.
- [52] R. Li, “Curvature-induced bunch self-interaction for an energy-chirped bunch in magnetic bends,” *Phys. Rev. ST Accel. Beams*, vol. 11, p. 024401, Feb 2008.

- [53] L. Giannessi and M. Quattromini, “Tredi simulations for high-brilliance photoinjectors and magnetic chicanes,” *Phys. Rev. ST Accel. Beams*, vol. 6, p. 120101, Dec 2003.
- [54] C. E. Mitchell, J. Qiang, and R. D. Ryne, “A fast method for computing 1-d wakefields due to coherent synchrotron radiation,” *Nuclear Instruments and Methods in Physics Research Section A: Accelerators, Spectrometers, Detectors and Associated Equipment*, vol. 715, pp. 119 – 125, 2013.
- [55] M. Dohlus and T. Limberg, “Csrtrack: Faster calculation of 3-d csr effects,” in *Proceedings of the 2004 FEL Conference*, (Trieste, Italy), pp. 18–21, 2004.
- [56] M. Dohlus, “Two methods for the calculation of csr field,” Tech. Rep. TESLA-FEL 2003-05, DESY, 2003.
- [57] K. Floettmann, “Astra: A space charge tracking algorithm,” 2011.
- [58] L. Giannessi and M. Quattromini, “TREDI simulations for high brilliance photoinjectors and magnetic chicanes,” *Phys. Rev. ST Accel. Beams*, vol. 6, p. 120101, 2003.
- [59] M. Dohlus in *Proceeding of the European Particle Accelerator Conference*, (Edinburgh, Scotland), pp. 26–30, 2006.
- [60] G. Bassi, J. A. Ellison, and K. A. Heinemann, “Comparison of 1D and 2D CSR Models with Application to the Fermi@Elettra Bunch Compressors,” *Conf. Proc.*, vol. C110328, pp. 1743–1745, 2011.
- [61] G. Bassi, J. A. Ellison, and K. Heinemann, “CSR effects in a bunch compressor: Influence of the transverse force and shielding,” *Conf. Proc.*, vol. C060626, pp. 2260–2262, 2006. [2260(2006)].
- [62] K. Brown *et al.*, “Transport a computer program for designing charged particle beam transport systems,” Tech. Rep. CERN 80-04, CERN, 1980.

## APPENDIX A

### TRANSPORT NOTATION

Transport notation, originally developed by K.L. Brown [62], provides a formalism for describing the motion of a particle beam as traverses a particle accelerator. The state of each particle in the bunch may be described in terms of the vector

$$(65) \quad \vec{W} = \begin{pmatrix} x \\ x' \\ y \\ y' \\ \beta ct \\ \delta \end{pmatrix}$$

The transverse coordinates are  $x$  and  $y$  and the canonical transverse momentum is measured in terms of the particle's divergence from the central path  $x' = dx/ds$ . The longitudinal coordinate along the central path is  $\beta ct$ , and  $\delta$  is the fractional momentum deviation  $p - p_0/p_0$  where  $p_0$  is the reference momentum.

For linear transport through some arbitrary element of the accelerator the final coordinate vector of a particle  $\vec{W}(1)$  can be found through the transformation of the initial state  $\vec{W}(0)$  by

$$(66) \quad \vec{W}(1) = A\vec{W}(0) = \begin{pmatrix} R_{11} & R_{12} & R_{13} & R_{14} & R_{15} & R_{16} \\ R_{21} & R_{22} & R_{23} & R_{24} & R_{25} & R_{26} \\ R_{31} & R_{32} & R_{33} & R_{34} & R_{35} & R_{36} \\ R_{41} & R_{42} & R_{43} & R_{44} & R_{45} & R_{46} \\ R_{51} & R_{52} & R_{53} & R_{54} & R_{55} & R_{56} \\ R_{61} & R_{62} & R_{63} & R_{64} & R_{65} & R_{66} \end{pmatrix} \begin{pmatrix} x \\ x' \\ y \\ y' \\ \beta ct \\ \delta \end{pmatrix}_0.$$

Where the matrix  $A$  is determined by the fields of the element. For a series of multiple elements in sequence from  $A_0$  to  $A_i$  the final coordinates the exit of the  $i$ th element may be found from

$$(67) \quad \vec{W}(1) = A_i \dots A_2 A_1 \vec{W}(0)$$

This system may be extended to arbitrary order with the  $i$ th coordinate  $W_i(1)$  being given by

$$(68) \quad W_i(1) = \sum_{j=1}^6 R_{ij} W_j(0) + \sum_{j=1}^6 \sum_{k=1}^6 T_{ijk} W_j(0) W_k(0) + \sum_{j=1}^6 \sum_{k=1}^6 \sum_{l=1}^6 U_{ijkl} W_j(0) W_k(0) W_l(0) + \dots$$

## APPENDIX B

### ACCELERATOR COORDINATE CONVENTIONS

In accelerator design it is typical to have some 'ideal' path through the accelerator, such a particle will, in general, be possessed of an energy we designate as the design energy of the accelerator and follow a perfect path through the center of the beamline and all elements comprising the accelerator. Because of this we are most concerned then with how the real particles of the beam will behave as they deviate from this design path.

This leads to a system, as in Fig. B.1, where the particle moves on the curved, reference trajectory with radius of curvature  $\rho_0(s)$ . The transverse axes are then always perpendicular to this reference trajectory.

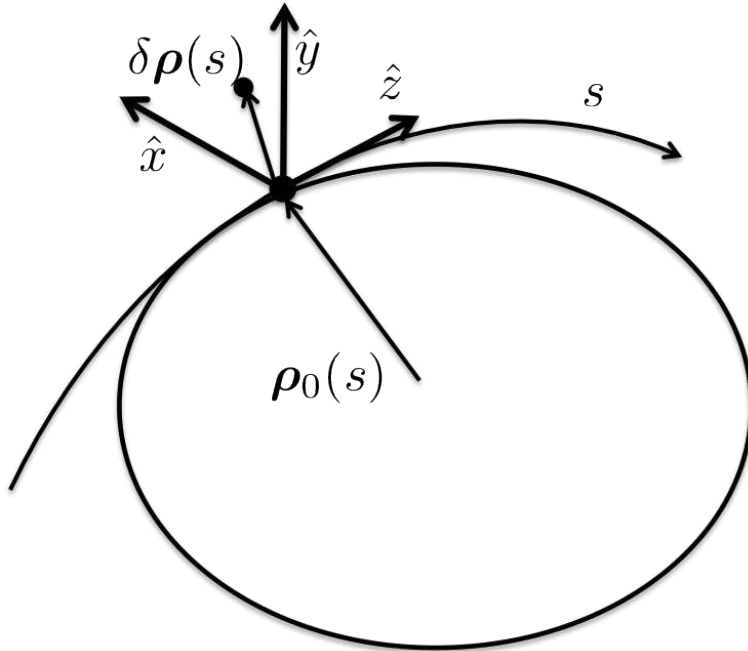


FIGURE B.1. The ideal reference trajectory through the accelerator along a path  $s$  with radius of curvature  $\rho_0(s)$  is shown. Particles in the bunch can then be defined in terms of their deviation from the reference particle, given as the vector  $\delta\rho(s)$

While there are no strict constraints placed on the form of this reference trajectory, because we are dealing with a physical system that has numerous design constraints it is usual to think of the reference trajectory as being closed and lying in a the x-z plane. This is important for our consideration in discussing CSR as the beam will be bent only in this single plane, leading to significant dispersive effects only in x, and allowing us to neglect the vertical particle motion (along the y-axis).

More formally this constitutes a Frenet-Serret coordinate system [18]. Where we define the trajectory of a particle relative to the reference trajectory as

$$(69) \quad \boldsymbol{\rho}(\mathbf{s}) = \boldsymbol{\rho}_0(s) + \delta\boldsymbol{\rho}(s).$$

The three unit vectors of this coordinate system are then

$$(70) \quad \hat{z} \equiv \frac{d\rho_0/ds}{|d\rho_0/ds|}$$

$$(71) \quad \hat{x} \equiv -\rho_0(s) \frac{d\hat{z}}{ds}$$

$$(72) \quad \hat{y} \equiv \hat{z} \times \hat{x}.$$

Based on this the particle's deviation from the ideal particle on the reference trajectory in Eq. 69 is then

$$(73) \quad \delta\boldsymbol{\rho}(s) = x\hat{x} + y\hat{y} + z\hat{z}.$$